Fermilab FERMILAB-THESIS-2002-36

Search for the Stau slepton at DELPHI

&

Muon identification and Z^0 production at CDF

Thesis submitted in accordance with the requirements
of the University of Liverpool
for the degree of Doctor in Philosophy
by

Agnes C. Taffard

March 2002

Abstract

The data taken in 1998 and 1999 by the DELPHI experiment at centre of mass energies between 189 GeV and 202 GeV, corresponding to an integrated luminosity of 378.2 pb^{-1}, were used to search for the supersymmetric partner of the tau lepton (stau, $\widetilde{\tau}$) in the context of the Minimal Supersymmetric Standard Model (MSSM) with R-parity conservation. In this scenario, staus could be pair produced at LEP2 and decay dominantly to the lightest neutralino ($\tilde{\chi}_1^0$) and a tau lepton ($\widetilde{\tau} \rightarrow \tau\tilde{\chi}_1^0$). In this context, the lightest neutralino is an ideal candidate for the lightest supersymmetric particle (LSP). Since R-parity conservation implies that the LSP is stable and neutral, the $\tilde{\chi}_1^0$ interacts weakly thus escaping detection. Therefore, the stau events are characterised by an acoplanar tau pair with missing energy.

The number of observed event candidates shows no significant deviation from the Standard Model prediction. The results were interpreted as a 95% confidence level (C.L.) exclusion region in the neutralino-stau mass plane. Assuming the MSSM input parameters for the Higgs mixing parameter, $\mu = -200$ GeV/c^2 and the ratio of the vacuum expectation values of the two Higgs doublets, $\tan\beta = 1.5$, the right-handed stau mass limit was found to be $m_{\widetilde{\tau}_R} \geq 63$ GeV/c^2 at 95%CL if the difference in mass between the neutralino and the stau is greater than 15 GeV/c^2.

The prospects of detecting trilepton events from the associated production of the lightest chargino ($\tilde{\chi}_1^{\pm}$) and the second lightest neutralino ($\tilde{\chi}_2^0$) in the context of the Minimal Supergravity model (MSUGRA) with the CDF experiment at the TEVATRON are overviewed. The $\tilde{\chi}_1^{\pm}$ and $\tilde{\chi}_2^0$ cascade decay to final states with a lepton and the lightest neutralino ($\tilde{\chi}_1^0$). In the case where the τ lepton decays leptonically, this channel can offer a *clean* trilepton signal with very little Standard Model background. Preliminary Monte Carlo studies have shown that for certain regions of MSUGRA parameter space, the *clean* trilepton signal could be observable in Run IIa with 2 fb^{-1} of data. The observation of a signal coming from the $\tilde{\chi}_1^{\pm}\tilde{\chi}_2^0$ associated production can be enhanced if the hadronic tau decay could be efficiently tagged while keeping the Standard Model backgrounds under control. In the eventuality that no signal is observed, a substantial region of the parameter space that was

not accessible at LEP2 can still be probed and the lightest chargino could be excluded up to a mass of ~ 200 GeV/c^2.

In preparation for the search for a supersymmetric trilepton signal, a cosmic ray muon tagger has been implemented, since cosmic ray muons are a natural source of background. The cosmic ray tagger was used to obtain the first Run IIa $Z^0/\gamma^* \to \mu^+\mu^-$ signal using the 3.1 pb^{-1} of data collected. The data candidates obtained in the mass window of $66 < M_{\mu^+\mu^-} < 116$ GeV/c^2 and with $|\eta_\mu| < 0.6$ have been used to measure the Z^0 production cross section. The Z^0 cross section was measured to be $4.84 \pm 1.08(stat.) \pm 0.77(syst.)$ nb which is in agreement with the RunI measurement of 6.94 ± 0.53 nb and with the QCD theoretical prediction of 6.05 ± 0.3 nb.

Author's Contribution

I started my Ph.D. at the University of Liverpool in October 1998. During my first year, I was involved in the construction of the silicon microstrip detector, Layer00, for the CDF experiment at FermiLab. The Layer00 detector was proposed as an additional single sided microstrip detector to be placed directly on the beam pipe, to improve vertex reconstruction. In order to optimise the intrinsic resolution of the Layer00 detector, I wrote a realistic Monte Carlo (MC) simulation for a microstrip silicon detector. The results of my work contributed to the major change from the original 8-fold design of Layer00 to a 12-fold design. Later on, I was also involved in the design and thermal testing of the mechanical support structure of Layer00. The Layer00 detector was installed as part of the silicon tracking in October 2000. This work is not presented in this thesis.

During the second year of my Ph.D., I undertook a search for the supersymmetric partner of the tau lepton (stau), with the Delphi experiment at Lep, whilst working at FermiLab on the commissioning of the CDF detector and on the offline code development. In this analysis, the Minimal Supersymmetric standard Model (Mssm) is assumed, as well as conservation of R-Parity. In this scenario, staus ($\widetilde{\tau}$) could be pair produced via e^+e^- annihilation into Z^0/γ. For a large fraction of parameter space, the dominant decay of the $\widetilde{\tau}$ is to the τ plus the lightest neutralino. Since the neutralino escapes undetected, the topology searched for is acoplanar τ pairs with missing energy. For this analysis, I used the data collected in 1998 and 1999, to develop and optimise a series of sequential cuts that reduce the Standard Model backgrounds while keeping a reasonable efficiency for the signal over a wide range of mass combinations. The number of observed events was found to be in agreement with the Standard Model prediction and the results were interpreted as a 95% CL confidence level exclusion region in the neutralino-stau mass plane. The results of my analysis were presented at the ICHEP 2000 conference in Osaka [1].

During the final year, I have focused on the investigation of the potential of Susy discovery at CDF via the associated production of the Chargino-Neutralino which cascade decay to 3 leptons and missing transverse energy. I have also been working on lepton identification, more particularly muons, using MC and the commissioning data collected in Summer 2001. I have also spent three months involved in the operation of the CDF detector where I was responsible for the data taking. I have developed the CDF cosmic ray muon tagger and identified the first $Z^0/\gamma^* \to \mu^+\mu^-$ events. I have used those data candidates to measure the Z^0 production cross section at $\sqrt{s} = 2$ TeV. The result obtained agrees with the RunI measurement and the QCD theoretical prediction at $\sqrt{s} = 1.8$ TeV.

Contents

1 Theory and Motivation **3**

1.1 Introduction 3

1.2 The Standard Model 3

1.2.1 Model description 5

1.2.2 Success and limitations 9

1.3 Supersymmetric Models 11

1.3.1 Motivation for Supersymmetry 12

1.3.2 Minimal Supersymmetric Standard Model (MSSM) 14

1.3.3 Minimal Supergravity (MSUGRA) 15

1.3.4 R-parity conservation 16

1.3.5 Particle spectrum 17

1.4 Supersymmetric Channels 21

1.4.1 Supersymmetric Scalar Tau at LEP 21

1.4.2 Trilepton signal from $\tilde{\chi}_1^{\pm}\tilde{\chi}_2^0$ associated production at CDF . . 24

2 The DELPHI detector and the LEP accelerator **28**

2.1 Introduction 28

2.2 The LEP Accelerator 28

2.2.1 The LEP ring 29

2.3 The DELPHI Detector 31

2.3.1 Tracking detectors 32

2.3.2 Calorimeters 37

2.3.3 Muon Chambers 40

2.4 The DELPHI Online System 41

2.4.1 Trigger 42

2.5 The DELPHI Offline Analysis Chain 42

3 Search for the supersymmetric scalar tau, stau ($\tilde{\tau}$) with DELPHI at $\sqrt{s} = 189$ to 202 GeV 44

3.1 Introduction 44

3.2 Data samples 45

3.3 Monte Carlo samples 45

3.3.1 SM backgrounds 45

3.3.2 Stau signal simulation 48

3.4 Search for Staus 49

3.4.1 Preselection 49

3.4.2 Main Selection 58

3.4.3 Results summary for 189 GeV analysis 73

3.5 Extension to 1999 data sets 80

3.6 Evaluation of systematic errors 85

3.7 Results 91

3.7.1 Exclusion limits 91

3.7.2 Stau mass limits calculation 93

3.8 Model dependence on the stau limit 95

3.9 Conclusion 96

4 The CDF detector at FERMILAB 97

4.1 Introduction 97

4.2 The TEVATRON Accelerator 98

4.3 The CDF Detector 99

4.3.1 Tracking detectors 102

4.3.2 Calorimeters 105

4.3.3 Muon Chambers 106

4.3.4 Luminosity counters (CLC) 109

4.3.5 Triggers 110

5 Muon reconstruction, cosmic tagger and $Z^0/\gamma^* \rightarrow \mu^+\mu^-$ using RunIIa data at CDF 112

5.1 Introduction 112

5.2 Muon identification 113

5.2.1 Muon reconstruction 113

5.2.2 Calorimeter Energy 113

5.2.3 Track Matching 114

5.3 Cosmic ray muon tagger 115

5.3.1 Data samples and detector status 115

5.3.2 Cosmic ray muon selection criteria 115

5.3.3 Performance of the cosmic ray muon tagger 119

5.3.4 Future plans 120

5.4 First $Z^0/\gamma^* \rightarrow \mu^+\mu^-$ events 121

5.4.1 Data samples and detector operation 121

5.4.2 Selection criteria 122

5.4.3 Z^0 production cross section measurement 126

5.5 Conclusion 129

6 Conclusions 132

List of Figures

1.1 SM loop corrections to the Higgs mass. 8

1.2 Electroweak measurements and comparison from Standard Model from Moriond 2001. 9

1.3 $\Delta\chi^2$ of the fit as a function of m_H. 10

1.4 Evolution of the inverse of the three coupling constants in the SM. . . 11

1.5 SUSY loop corrections to the Higgs mass. 12

1.6 Evolution of the inverse of the three coupling constants in the MSSM. 14

1.7 Running of the sparticle masses from the GUT scale to EW scale . . 16

1.8 Production and decay diagram for the stau 22

1.9 Stau production cross section and $BR(\tilde{\tau}_R^{\pm} \to \tau + \tilde{\chi}_1^0)$ 23

1.10 Event display of MC stau event. 23

1.11 Feynman diagrams for $q\bar{q}' \to \tilde{\chi}_1^{\pm}\tilde{\chi}_2^0$ 24

1.12 Feynman diagrams for $\tilde{\chi}_1^{\pm} \to l\nu\tilde{\chi}_1^0$ and $\tilde{\chi}_2^0 \to \tilde{\chi}_1^0 l^+ l^-$ 25

1.13 Cross section $p\bar{p} \to \tilde{\chi}_1^{\pm}\tilde{\chi}_2^0 \to 3l + X$ without cuts. 26

1.14 Contours for the 99% C.L. for Run IIa (2 fb^{-1}) in the $(m_{1/2}, m_0)$ plane for the SUSY trilepton channel. 27

2.1 The CERN accelerators. 29

2.2 A perspective view of the DELPHI detector. 33

2.3 The Silicon trackers. 35

2.4 The Time Projection Chamber. 36

2.5 Internal structure of the HPC module. 38

2.6 The STIC detector. 39

2.7 A typical sector of the DELPHI barrel muon chambers. 41

2.8 DELPHI offline analysis chain. 43

3.1 Cross sections of some typical SM processes. 46

3.2 Track length for data superimposed on the expected backgrounds. . . 50

3.3 Theta distribution, z and Rϕ impact parameter before cosmic rejection. 51

3.4 Theta distribution and z and $R\phi$ impact parameters after cosmic rejection. 52

3.5 Total visible charge energy in the event. 53

3.6 Energy in the FEMC detector. 54

3.7 Sum of the jets transverse momenta. 54

3.8 Energy of the largest isolated neutral. 55

3.9 Charged tracks topology in the event for forward and barrel. 56

3.10 Number of charged tracks outside the cones in the event for forward and barrel. 57

3.11 Theta distribution of the leading tracks before and after tracking efficiency correction in the forward region. 58

3.12 Acolinearity distribution. 60

3.13 Total visible energy. 61

3.14 p_T^{jets} of the two leading tracks. 62

3.15 Distributions of $cos^2(\theta_{J1}) + cos^2(\theta_{J2})$ and acoplanarity. 63

3.16 2-dimensional plot of $cos^2(\theta_{J1}) + cos^2(\theta_{J2})$ -vs- jets acoplanarity. . . . 64

3.17 $F_1 = (cos^2(\theta_{J1}) + cos^2(\theta_{J2})) - 0.075 \times$ jets acoplanarity $+ 0.15$. . . . 65

3.18 Distribution of $\sqrt{(p_{J1}^2 + p_{J2}^2)}/E_b$. 65

3.19 2-dimensional plot of $Jp_{rad} = \sqrt{p_{J1}^2 + p_{J2}^2}/E_b$ -vs- F_1. 66

3.20 Distribution of $F_2 = Jp_{rad} - 0.075 \times F_1 - 0.2$. 67

3.21 Distribution of $|90^o - \theta_{miss}|$. 68

3.22 Distribution of the energy in the STIC detector. 68

3.23 Distribution of the isolated neutral energy. 69

3.24 p_T^{jets} for two track events with identified leptons in the final state. . . 69

3.25 Number of electrons and muons for 3 track events. 70

3.26 Fully leptonic decay modes of the W and Stau for two track events. . 71

3.27 Distribution of the secondary leading track momentum for two track events. 72

3.28 Distribution of total momentum and $q_J \times cos(\theta_J)$ for the 2 leading jets for W^+W^- and Stau Monte Carlo. 74

3.29 Distribution of log(likelihood ratio). 75

3.30 $\frac{Signal}{\sqrt{background}}$ of the log(likelihood ratio). 75

3.31 Invariant mass of each of the cones. 76

3.32 Event display of a $\widetilde{\tau}^+\widetilde{\tau}^-$ candidate. 79

3.33 Acolinearity distribution for samples at 192 GeV, 196 GeV, 200 GeV and 202 GeV 81

3.34 $F_1 = (cos^2(\theta_{J1}) + cos^2(\theta_{J2})) - 0.075 \times$ jets acoplanarity $+ 0.15$ for samples at 192 GeV, 196 GeV, 200 GeV and 202 GeV 82

3.35 Distribution of likelihood ratio for samples at 192 GeV, 196 GeV, 200 GeV and 202 GeV 83

3.36 Distributions of the jets acolinearity, E_{vis} and p_T^{jets} for barrel and forward regions. 86

3.37 Mass limits for the scalar Stau 95% CL exclusion region from data and MC simulation. 94

3.38 Mass limit fluctuation for the scalar Stau when errors are taken into account. 95

4.1 The FermiLab accelerators 98

4.2 The CDF detector 100

4.3 Quadrant of the CDF tracking system. 102

4.4 End view of the CDF silicon system and end view of the innermost three layers of silicon system. 103

4.5 $1/6^{th}$ of a COT end plate and cell layout of SL-2. 104

4.6 A wedge of the central electromagnetic calorimeter (CEM). 106

4.7 Coverage of the muon chambers in the $\eta - \phi$ plane. 107

4.8 Schematic view of a CMP-CMX tube. 108

4.9 Drift tube layout in a 15° CMX module. 109

4.10 Schematic view of the luminosity monitor inside a quadrant of CDF. . 110

4.11 The Run II readout block diagram. 111

5.1 Electromagnetic calorimeter (a) and hadronic calorimeter (b) energy deposit from a single muon with $4 < p_T < 40$ GeV/c. 114

5.2 Distance, δX between the CMU stub and the extrapolated track in the $R\phi$ plane versus the muon momentum. 114

5.3 Two dimensional plot of $z0$ and $d0$ for the selected muon pair. 116

5.4 Distribution of $\rho = \sqrt{d0_1^2 + d0_2^2}$ (a) and $\alpha = \tan^{-1}(d0_2/d0_1)$. 117

5.5 Distribution of the acolinearity for the data and MC Drell-Yan $Z^0/\gamma^* \to \mu^+\mu^-$. 118

5.6 Distribution of the forward energy, E_{plug}, when the acolinearity between the selected muon pair is greater that 2.9 rad for the data and MC Drell-Yan $Z^0/\gamma^* \to \mu^+\mu^-$ 119

5.7 Distribution of δt_0 between the selected muon pair for events tagged as cosmic and the other events and distribution of δt_0 between the selected muon pair for all events. 120

5.8 Distribution of δt_0 between the selected muon pair for the events remaining after cosmic ray rejection. 121

5.9 Distribution of the total transverse energy in a cone of $\Delta R = 0.4$ around the muon direction. 123

5.10 (a) Number of hits per stub for CMX muons. (b) Track matching variable, δX, for CMU muon. (c) Total electromagnetic energy deposited by the muons. (d) Total hadronic deposited by the muons. . . 124

5.11 (a) $d0$ distribution of the muons. (b) $z0$ distribution of the muons. . . 125

5.12 Distribution of the invariant mass of the two muons after selection without applying the cosmic ray filter and with applying the cosmic ray filter. 126

5.13 Distribution of the invariant mass of the two muons after selection, for MC Drell-Yan and data. 130

5.14 CDF event display of a $Z^0/\gamma^* \to \mu^+\mu^-$ candidate. 130

List of Tables

1.1 The elementary fermions 4

1.2 Properties of the gauge bosons. 4

1.3 Particles of the MSSM. 18

2.1 Specifications and performance of the DELPHI tracking detectors. . . 34

2.2 Specifications and performance of the DELPHI calorimeters. 37

2.3 Specifications and performance of the DELPHI muon chambers. 40

3.1 Integrated luminosities for each data sample after run quality checks. 45

3.2 Simulation Data sets 47

3.3 Number of events in data and expected background after each of the preselection cuts. 59

3.4 Effect of the sequential cuts on the data and simulated backgrounds using the refitted weights. 77

3.5 Effect of the sequential cuts on the stau signal ($\widetilde{\tau}_R$,$\tilde{\chi}_1^0$) of (50,40) GeV/c^2 and (80,20) GeV/c^2. 77

3.6 Sample composition of the backgrounds generated at 189 GeV at the end of the analysis. 78

3.7 Stau signal efficiency with error at the end of the analysis for each $\widetilde{\tau}_R - \tilde{\chi}_1^0$ mass combination. 78

3.8 Sample composition of the backgrounds generated at 196 GeV at the end of the analysis. 84

3.9 Sample composition of the backgrounds generated at 200 GeV at the end of the analysis. 84

3.10 Number of data events, expected background events and standard deviations observed for the barrel and forward regions during the sequential cuts, using original MC weights for the 189 GeV analysis. . 85

3.11 Composition of the selected samples with lepton identification for forward and barrel for the 189 GeV analysis. 87

3.12 Mean fitted weights in the barrel, for the 189 GeV analysis. 88

3.13 Mean fitted weights in the forward region, for each of the backgrounds for the 189 GeV analysis. 88

3.14 Standard deviations observed for the barrel and forward regions for the first five cuts of the analysis at 189 GeV, 196 GeV and 200 GeV. 89

3.15 Standard deviations observed for the barrel and forward regions using refitted MC weights for the first five cuts of the analysis at 189 GeV, 196 GeV and 200 GeV. 90

3.16 Number of data candidates with expected background from 189 GeV to 202 GeV. 91

4.1 Run 1b and Run IIa foreseen parameter list 101

4.2 Specifications of the CDF silicon tracking detectors. 103

5.1 Criteria used to select cosmic ray events. 118

5.2 Number of data events and percentage of Drell-Yan MC after each cut for $|\eta|$ <0.6 and $|\eta|$ <2.0. 125

5.3 Reconstruction efficiencies of CMU and CMP for single muon in the MC and data. 128

Preface

The Standard Model has been very successful in predicting the properties of new particles and the structure of the interactions between them. However, despite its excellent agreement with experimental measurements, the Standard Model contains several theoretical problems that cannot be solved without the introduction of new physics beyond the Standard Model. At present, the preferred theories are based on Supersymmetry (SUSY) which introduces a new symmetry between the fermions and the bosons. Supersymmetry predicts the existence of supersymmetric partners (sparticles) to all Standard Model particles.

This thesis presents a search for the supersymmetric partner of the Standard Model tau lepton, known as scalar tau (stau), with the DELPHI detector at LEP2 and discusses the prospects for observing a supersymmetric signal in the trilepton channel with the CDF detector at the TEVATRON in Run IIa. Additionally, the implementation of a cosmic ray muon tagger and the measurement of the Z^0 production cross section at $\sqrt{s} = 2$ TeV with the CDF detector are described.

In the Minimal Supersymmetric Standard Model with R-parity conservation (MSSM), staus ($\widetilde{\tau}$) could be pair produced at LEP2. The dominant decay of the stau is to the lightest neutralino ($\tilde{\chi}_1^0$), assumed to be the lightest supersymmetric particle (LSP), and to the tau lepton ($\widetilde{\tau} \to \tau\tilde{\chi}_1^0$). Since R-parity conservation implies that the LSP is stable and neutral, the $\tilde{\chi}_1^0$ interacts weakly thus escaping detection. Therefore, the stau events are characterised by an acoplanar tau pair with missing energy.

In the Minimal Supergravity model (MSUGRA) with R-parity conservation, the source of the supersymmetric trilepton signal, that could be produced at the TEVATRON, is the associated production of the lightest chargino ($\tilde{\chi}_1^\pm$) and the second lightest neutralino ($\tilde{\chi}_2^0$) which cascade decay to leptons and $\tilde{\chi}_1^0$ for some regions of the parameter space. At the TEVATRON, the pair production of $\tilde{\chi}_1^\pm\tilde{\chi}_2^0$ is expected to dominate over other strongly produced supersymmetric processes. Therefore, this

channel could produce a *clean* trilepton signal ($l = e$ or μ) plus missing transverse energy ($\not{E}_T$) almost free of Standard Model backgrounds.

In preparation for the search for a supersymmetric trilepton signal, a cosmic ray muon tagger is implemented and is used to obtain the first Run IIa $Z^0/\gamma^* \rightarrow \mu^+\mu^-$ signal. The number of data candidates with a reconstructed invariant mass in the mass window of $66 < M_{\mu^+\mu^-} < 116$ GeV/c^2 and with $|\eta_\mu| < 0.6$ are used to measure the Z^0 production cross section at $\sqrt{s} = 2$ TeV.

Chapter 1 presents the Standard Model and describes its theoretical shortcomings. The motivations for supersymmetry are outlined and the MSSM and MSUGRA models are described. The production and decay of scalar tau at LEP2 and the prospects for the discovery with the CDF detector of the supersymmetric trilepton signal from the associated production of the $\tilde{\chi}_1^\pm\tilde{\chi}_2^0$ are discussed. Chapter 2 introduces the LEP accelerator and the DELPHI detector. The search for staus with the DELPHI detector is presented in Chapter 3. The data and the Monte Carlo simulated samples are outlined followed by the description of the selection of the stau candidates based on a sequential cut analysis. Since the result is in agreement with the Standard Model prediction, it is interpreted as an excluded region in the $\tilde{\tau}\tilde{\chi}_1^0$ mass plane. Chapter 4 presents the TEVATRON and the CDF detector. Chapter 5 describes the implementation of the CDF cosmic ray tagger, the selection criteria used to isolate the $Z^0/\gamma^* \rightarrow \mu^+\mu^-$ signal using the 3.1 pb^{-1} of data collected, and the measurement of Z^0 production cross section at $\sqrt{s} = 2$ TeV. Chapter 6 concludes and discusses the future prospects of the search for supersymmetry using the trilepton signal.

Chapter 1

Theory and Motivation

1.1 Introduction

The Standard Model (SM) of particle physics is one of the most successful theories ever constructed and is in excellent agreement with experimental measurements. In spite of this, the Standard Model contains several theoretical problems which cannot be solved without the introduction of new physics.

This chapter discusses briefly the Standard Model (SM) of particle physics and some of its successes and limitations. It is shown how the introduction of a new kind of symmetry, Supersymmetry (SUSY), solves two of the main problems of the SM, namely the hierarchy problem and the unification of the couplings at a higher scale and by doing so reduces the number of free parameters. The basic ideas of the Minimal Supersymmetric Standard Model (MSSM), the minimal Supergravity model (MSUGRA) and R-Parity conservation are introduced as well as the predicted particle spectrum. Finally, the two supersymmetric channels relevant to this thesis, involving the production of supersymmetric particles at DELPHI and CDF, are described.

1.2 The Standard Model

The Standard Model [2] describes the interactions of the fundamental particles, called fermions, via the exchange of bosons. The constituents of matter, fermions, are organised in three families (see Table 1.1).

Fermions	Generation			Quantum Numbers		
	1	2	3	Q	I_3^W	Y
Leptons	$\begin{pmatrix} \nu_e \\ \mathrm{e} \end{pmatrix}_L$	$\begin{pmatrix} \nu_\mu \\ \mu \end{pmatrix}_L$	$\begin{pmatrix} \nu_\tau \\ \tau \end{pmatrix}_L$	0	$+\frac{1}{2}$	-1
				-1	$-\frac{1}{2}$	-1
	e_R	μ_R	τ_R	-1	0	-2
Quarks	$\begin{pmatrix} \mathrm{u} \\ \mathrm{d}' \end{pmatrix}_L$	$\begin{pmatrix} \mathrm{c} \\ \mathrm{s}' \end{pmatrix}_L$	$\begin{pmatrix} \mathrm{t} \\ \mathrm{b}' \end{pmatrix}_L$	$+\frac{2}{3}$	$+\frac{1}{2}$	$+\frac{1}{3}$
				$-\frac{1}{3}$	$-\frac{1}{2}$	$+\frac{1}{3}$
	u_R	c_R	t_R	$+\frac{2}{3}$	0	$+\frac{4}{3}$
	d'_R	s'_R	b'_R	$-\frac{1}{3}$	0	$-\frac{2}{3}$

Table 1.1: The elementary fermions and their electroweak quantum numbers, where Q is the charge, I_3^W is the third component of weak isospin and Y is the weak hyper-charge. The subscripts L and R refer respectively to left and right-handed helicity states.

The fundamental forces, electroweak, strong and gravitational are mediated by the exchange of bosons. (see Table 1.2).

Boson	Q	I_3^W	Mass [GeV/c^2]	Interaction
Vector Boson				
$\begin{pmatrix} W^+ \\ W^- \end{pmatrix}$	$+1$	$+1$	80.45	(charged) Electroweak
	-1	-1		
Z^0	0	0	91.19	(neutral) Electroweak
γ	0	0	0	(neutral) Electroweak
g	0	0	0	QCD
Scalar Boson				
H	0	0	> 113.5 [3]	Yukawa

Table 1.2: Properties of the gauge bosons, where Q is the charge, I_3^W is the third component of weak isospin.

The electromagnetic force is mediated by photons, the weak force by the heavy bosons, Z^0 and $\mathrm{W}^\pm$ and the strong force by gluons. The Standard Model envisages that gravity is mediated by the exchange of the graviton, but a satisfactory quantum description of gravity has not yet been described. The masses of the fermions and

heavy bosons are generated by the Higgs mechanism involving a heavy scalar Higgs boson which has not yet been observed. LEP experiments have excluded a Standard Model Higgs with mass below 113.5 GeV/c^2 [3].

Presently, the Higgs boson is the one remaining particle of the Standard Model that has so far not been discovered. All other Standard Model particles have been observed and many of their properties have been measured.

1.2.1 Model description

The Standard Model combines the idea of quantum mechanics and special relativity into a quantum field theory description where the particles emerge as quanta of the field variables. Its two major components are Quantum Chromodynamics (QCD) and the Unified Electroweak Theory (QED). The model is based on the symmetry groups $SU(3)_C \otimes SU(2)_L \otimes U(1)_Y$. The $SU(3)_C$ symmetry group, where C denotes the colour, describes the strong interactions mediated by eight gluons. The $SU(2)_L \otimes U(1)_Y$ symmetry group, where L denotes left-handed helicity and Y the weak hyper-charge, describes the weak and electromagnetic interactions and is known as electroweak symmetry.

Electroweak theory

The central postulate of the SM is invariance under local gauge transformations. The invariance requirement leads to the introduction of four massless fields. The first three constitute a triplet $W_\mu^{a=1,2,3}$ associated to weak isospin of the $SU(2)_L$ group and the fourth is a single B_μ field associated to hyper-charge Y of the $U(1)_Y$ group where:

$$Y = 2(Q - I_3^W) \tag{1.1}$$

The B_μ field couples to the fermions with a strength g' while the W_μ fields couple with strength g to the left handed chirality states. The observed gauge bosons are linear combination of the four gauge fields.

The two charged boson fields $W_\mu^\pm$ are given by:

$$W_\mu^\pm = \frac{1}{\sqrt{2}}(W_\mu^1 \mp iW_\mu^2) \tag{1.2}$$

Since the Z boson couples to both right and left handed fermions, the field, A_μ, corresponding to the physical γ, and the field, Z_μ, corresponding to Z^0, are orthogonal

combinations of the W_μ and B_μ fields and are given by:

$$A_\mu = \sin\theta_W \; W^3_\mu + \cos\theta_W \; B_\mu \tag{1.3}$$

$$Z_\mu = \cos\theta_W \; W^3_\mu - \sin\theta_W \; B_\mu \tag{1.4}$$

The weak mixing angle, θ_W can be expressed as a function of the weak and electromagnetic coupling constants, g and g' :

$$g \sin\theta_W = g' \cos\theta_W = e \tag{1.5}$$

where e is the electron charge.

The coupling strengths[1], $\alpha_{i=1,2,3}$ are defined as:

$$\alpha_i(Q^2 = 0) = \frac{g_i^2}{4\pi} \tag{1.6}$$

The electromagnetic fine structure constant, α_{em}, has the value 1/137 at energies which are small compared with the electron mass. At higher energies it becomes larger, for example, at LEP energies it takes a value closer to 1/128.

Quantum Chromodynamics

The gauge theory of the strong interaction is called Quantum Chromodynamics (QCD) [4]. In this theory the quarks possess an internal property called *colour* and the gauge transformations are transformations between quarks of different colours.

The eight gauge bosons of QCD are called gluons and these are the ones that mediate the strong interaction. Due to colour exchange, multiple gluon couplings are allowed in QCD which is what underlies the decreasing strength of the strong coupling, α_3 with increasing energy scale. At the Z^0 mass energy scale, the strong coupling is measured to be:

$$\alpha_3(M_Z^2) = 0.118 \pm 0.004 \tag{1.7}$$

Higgs Mechanism

The principle of local invariance leads to the introduction of the massless W and B fields. However, since the weak interactions are very short range, it implies that the gauge bosons must be massive. In order to give mass to the gauge bosons without

[1] For matter of simplicity, the natural units $\hbar = c = 1$ have been used.

loosing local gauge invariance, a procedure exploiting the spontaneous symmetry breaking mechanism and the Higgs mechanism [5] is introduced. The Higgs mechanism introduces a weak isospin doublet of a complex scalar field with hyper-charge Y=1:

$$\Phi(x) = \begin{pmatrix} \Phi^+ \\ \Phi^0 \end{pmatrix} = \begin{pmatrix} (\Phi_1 + i\Phi_2)/\sqrt{2} \\ (\Phi_3 + i\Phi_4)/\sqrt{2} \end{pmatrix} \tag{1.8}$$

where Φ_i are real fields. The most general form of the potential which stays invariant under gauge transformation can be written as:

$$V(\Phi) = \mu^2|\Phi|^2 + \lambda|\Phi|^4 \tag{1.9}$$

By choosing the parameters $\mu^2 < 0$ and $\lambda > 0$, the potential has an infinite number of states each with the same lowest energy:

$$< \Phi >= \sqrt{\frac{-\mu^2}{2\lambda}} \equiv \ v \neq \ 0 \tag{1.10}$$

The fundamental state is degenerate and does not respect the gauge symmetry of $SU(2)_L \otimes U(1)_Y$. This phenomenon is called spontaneous symmetry breaking, where the vacuum expectation value, v, represents the energy scale where the electroweak symmetry is broken. By expressing the Lagrangian in terms of these fields, one obtains a massive scalar particle called the Higgs boson (H), and three massless particles known as Goldstone bosons.

P.W. Higgs was one of the first to realise that the choice in which the vacuum is the true vacuum is equivalent to choosing a gauge, which is necessary in order to quantise the theory. G. Hooft and M. Veltman [6] applied that idea to the Standard Model. In the Higgs mechanism, perturbative expansion is computed around:

$$\Phi_0 = \frac{1}{\sqrt{2}} \begin{pmatrix} 0 \\ v \end{pmatrix} \tag{1.11}$$

The three degrees of freedom of the scalar doublet are used to give the longitudinal polarisation of the $W^\pm$ and Z^0 bosons. The mass terms appear only for the W_μ, Z_μ and H fields. The A_μ field, corresponding to the photon, stays massless since the choice of the hyper-charge $Y = 1$ for the scalar doublet leaves it invariant under $U(1)_Y$ local gauge transformation. The mass of the gauge bosons are given by:

$$M_W = \frac{1}{2}gv \tag{1.12}$$

$$M_Z = \frac{1}{2}gv/\cos\theta_W \tag{1.13}$$

$$M_H = v\sqrt{2\lambda} \tag{1.14}$$

The parameter v is related to the Fermi coupling constant, G_F by:

$$v = (G_F\sqrt{2})^{-\frac{1}{2}} = 246 \text{ GeV} \tag{1.15}$$

which has been measured to high precision [7].

From equation 1.12 and 1.13 one can see that the theory predicts the ratio of the W-mass to the Z-mass, but since λ is a free parameter of the theory, the mass of the Higgs boson is not predicted.

Hierarchy problem

This section describes the problem of quadratic divergence of the Higgs Boson mass when radiative corrections are taken in account.

Let's consider the first order perturbative correction to the Higgs boson mass.

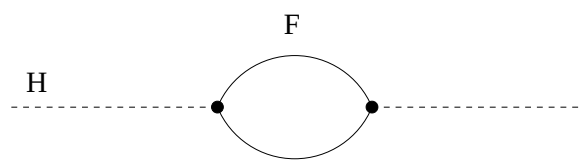

Figure 1.1: SM quantum correction for the Higgs mass: loop containing a Dirac fermion F with mass m_F.

Figure 1.1 shows the one loop correction to m_H^2 from a Dirac fermion F of mass m_F and with coupling strength, λ_F, of the Higgs to the fermions. The correction is then given by:

$$\Delta m_H^2 = \frac{|\lambda_F|^2}{16\pi^2}\left[-2\Lambda_{UV}^2 + 6m_F^2 ln\left(\frac{\Lambda_{UV}}{m_F}\right) + \ldots\right] \tag{1.16}$$

where Λ_{UV} is the momentum cutoff parameter used to regulate the loop integral. It can be interpreted as the energy scale at which new physics enters to alter the high-energy behaviour of the theory. The first term of equation 1.16 diverges quadratically with the momentum cutoff Λ_{UV}. Since the Higgs-fermion coupling is proportional to the fermion mass, the most important contribution occurs in the case of the top quark ($\lambda_F \approx 1$). If we insert $\Lambda_{UV} \sim M_{Planck}$, then the radiative correction to the scalar field is of the order of the Planck scale:

$$\Delta m_H^2 \approx (10^{19} \text{ GeV}/c^2)^2 \tag{1.17}$$

Those corrections need to be compared with the order of magnitude of the Higgs mass which is required to be less than 1 TeV in order for the SM to stay a perturbative theory [14]. Thus those large quadratic corrections must be cancelled by a fine-tuning of the parameters to the order of one part in 10^{16} and such a tuning is extremely unnatural. Additionally, this cancellation must occur at every order in perturbation theory and therefore the parameters need to be retuned each time. This problem is known as the hierarchy problem.

1.2.2 Success and limitations

Over the past 11 years, experiments carried at CERN, SLAC and FNAL have checked many of the Standard Model predictions to high accuracies (see Fig 1.2) [8] .

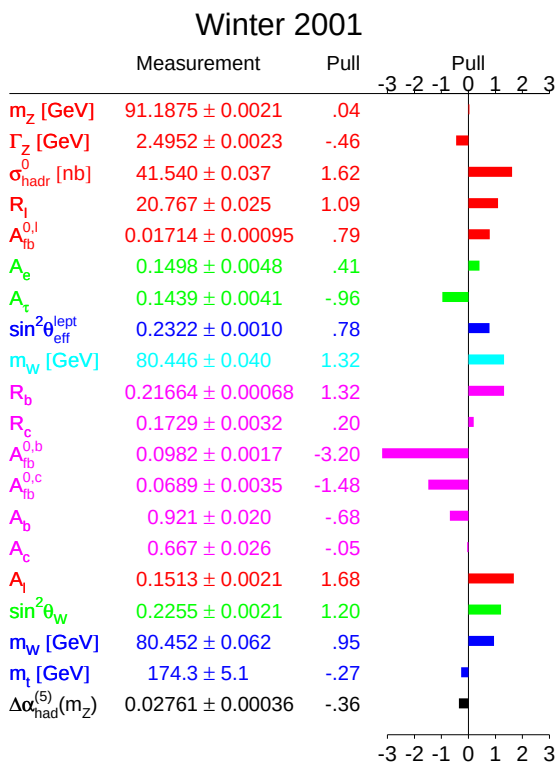

Figure 1.2: Electroweak measurements and comparison from Standard Model from Moriond 2001.

Some of those high precision measurements have been the determination of the $W^{\pm}$ ($M_W = 80.452 \pm 0.062$ GeV/c^2) and Z^0($M_Z = 90.1871 \pm 0.0021$ GeV/c^2) masses, the weak mixing angle ($\sin^2\theta_W = 0.2255 \pm 0.0021$) [9] as well as determining the num-

ber of neutrino families to $N_f = 2.994 \pm 0.012$ [11]. However, the most impressive result is the tight constraint on the top quark mass by experiments at LEP without this particle being kinematically accessible [9]. Higher-order processes involving virtual top quarks are an important element in quantum corrections to the predictions that the electroweak theory makes for many observables. The comparison of experimental measurements at LEP and theoretical predictions favours a top mass in the neighbourhood of 180 GeV/c^2, which is compatible with the TEVATRON top quark mass measurement $175.9 \pm 4.8(\text{stat.}) \pm 4.9(\text{syst.})$ [12].

As shown in Figure 1.3, direct searches and precision measurements constrain the Higgs mass to be between about 113.5 GeV/c^2 and 200 GeV/c^2. The value of χ^2, associated to the adjustment of the different independent SM parameters, seems to favour a Higgs mass below 150 GeV/c^2 (see Section 1.3.5).

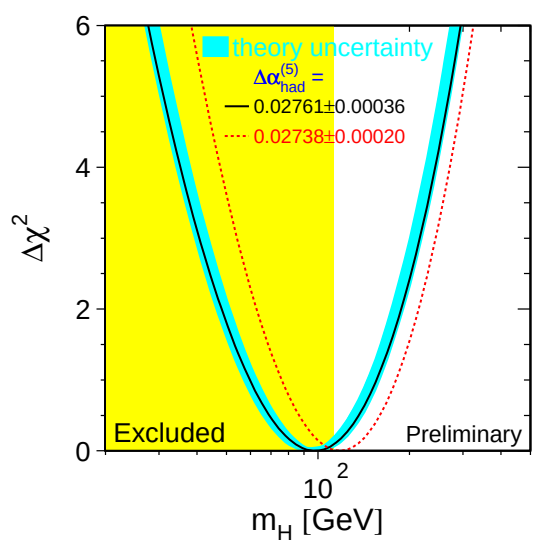

Figure 1.3: $\Delta\chi^2$ of for a global fit of the precision electroweak data as a function of m_H. The main result is shown by the solid curve. The associated band represents the estimate of the theoretical uncertainty. The dashed curve is the result using a theory driven determination of $\Delta\alpha_h(m_Z)$ [13].

Although the Standard Model seems to be a very effective theory at the electroweak scale *i.e.*,at $\sqrt{s} \approx M_W \approx M_Z$, many problems remain. Some of them are:

- Although the Higgs mechanism provides a framework to predict the bosons masses, it appears somehow *ad hoc* and does not explain the origin of spontaneous symmetry electroweak breaking.

- The Standard Model has three independent gauge groups, each with its own gauge coupling α_1, α_2, α_3. An idea which theorists find very appealing is that the three forces described by these three gauge groups are parts of a single unifying force. It is assumed that there exists some large scale, M_{GUT}, at which these three gauge couplings converge and above which there is only one Grand Unified Force. The three gauge couplings accurately measured at the Z mass scale can be extrapolated to the GUT scale ($M_{GUT} \sim 10^{16}$ GeV/c^2) using the Renormalisation Group Equations (REG). As shown in Figure 1.4, the coupling constants do not unify at a large energy scale. This contradicts the unification of the forces.

- When radiative corrections to the Higgs mass are taken in account, scalar corrections to the Higgs mass become quadratically divergent (see Section 1.2.1). One solution to cancel those divergences is to *fine-tune* the parameters, which is regarded by most theorists as unacceptable.

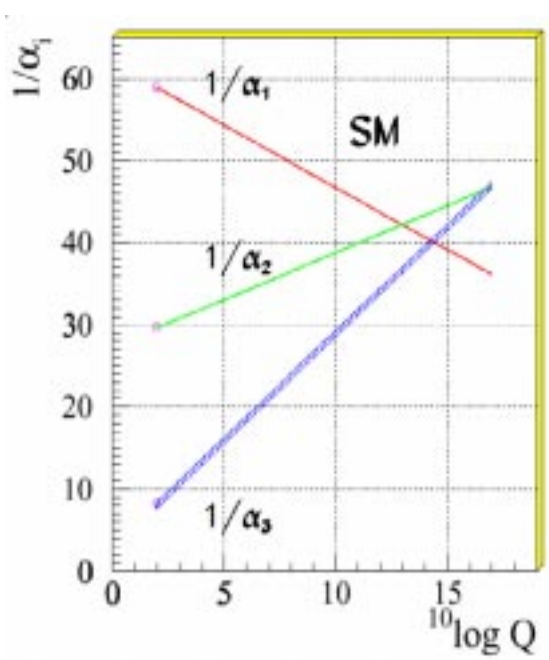

Figure 1.4: Evolution of the inverse of the three coupling constants in the SM, where α_1 (e.m), α_2 (weak) and α_3 (strong).

1.3 Supersymmetric Models

In recent years, supersymmetry (SUSY) has been extensively studied to give a picture of possible physics beyond the SM. Supersymmetry is an elegant theory which relates fermions to bosons. This theory predicts the existence of additional particles which differ from their SM partner by half unit of spin. In this section, the motivation to supersymmetry will be introduced. The Minimal Supersymmetric Standard Model (MSSM) will be briefly described as well as one of the supersymmetric breaking mechanisms (SUGRA) which predicts the entire SUSY mass spectrum from a few parameters. The concept of R-Parity conservation will be introduced and finally the particle spectrum will be described.

1.3.1 Motivation for Supersymmetry

This section describes how the introduction of supersymmetry solves both the hierarchy problem and the unification of couplings at a high energy scale.

Solving the hierarchy problem

Supersymmetry (SUSY) offers a very attractive solution for the hierarchy problem by generating another loop contribution so that both contributions cancel the divergence.

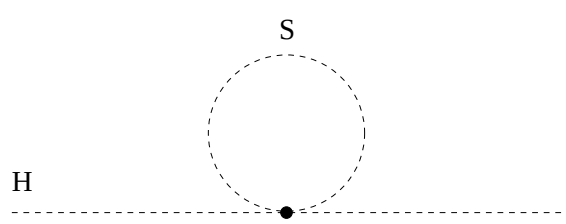

Figure 1.5: SUSY quantum correction for the Higgs mass: loop containing scalar particle S with mass m_S.

If an additional scalar particle S with mass m_S and with a coupling λ_S exists, an additional correction shown in figure 1.5 arises and can be written as:

$$\Delta m_H^2 = \frac{\lambda_S}{16\pi^2}\left[\Lambda_{UV}^2 - 2m_S^2 ln\left(\frac{\Lambda_{UV}}{m_S}\right) + \ldots\right] \tag{1.18}$$

By comparing equations 1.16 and 1.18, one can see that by choosing $\lambda_S = |2\lambda_F|^2$, the quadratic divergence cancels out. Furthermore a complete cancellation of the fermionic and bosonic contribution, even at higher orders, can be achieved by also requiring $m_F = m_S$. Hence, a mechanism that transforms fermions into bosons and vice-versa gives a possible solution to the hierarchy problem.

Supersymmetry solves the gauge hierarchy problem by predicting that all bosons have a fermionic partner and all fermions have a bosonic partner. The supersymmetric partners differ from their ordinary partner by half unit of spin, all other quantum numbers remain unchanged. The operator which transforms fermions into bosons and vice versa, is an anti-commutating spinor, Q with:

$$Q|boson >= |fermion > \qquad Q|fermion >= |boson > \tag{1.19}$$

Each SM particle is paired with its superpartner to form a supermultiplet with the same coupling strength. There are two types of supermultiplets:

- *Chiral supermultiplet* contains a chiral spin-$\frac{1}{2}$ fermion and a spin-0 scalar;
- *Massless Vector supermultiplet* contains a spin-1 vector boson and a Majorana[2] spin-$\frac{1}{2}$ fermion.

Unification of gauge couplings

As mentioned in Section 1.2.2, in the SM the gauge coupling constants do not unify at any energy scale. However, in a supersymmetric theory, the new particles introduced into the spectrum change the evolution of the couplings. Figure 1.6 shows this evolution in the SUSY model. The forces unify around 10^{16} GeV.

If supersymmetry was an exact symmetry, the particles and their superpartners would be degenerate in mass. Since no scalar particles with the same mass as the SM fermions have been observed, SUSY must be broken at some higher energy scale. Two supersymmetric breaking mechanisms have been studied in the literature: gravity mediated supersymmetry breaking (SUGRA) [16] and gauge mediated supersymmetry breaking (GMSB) [17]. In this thesis, the SUGRA breaking mechanism is considered.

[2] A Majorana fermion, ψ is one which is its own charge conjugate, $\psi^c = \psi$, e.g.:Majorana neutrino.

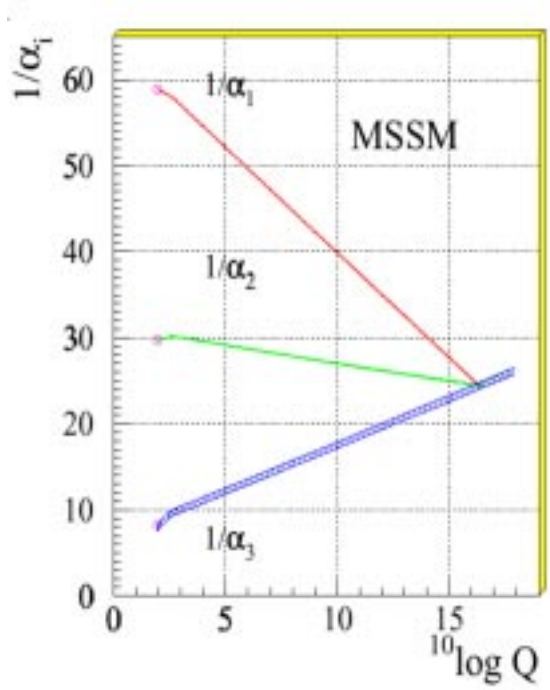

Figure 1.6: Evolution of the inverse of the three coupling constants in the MSSM, where α_1 (e.m), α_2 (weak) and α_3 (strong).

1.3.2 Minimal Supersymmetric Standard Model (MSSM)

The Minimal Supersymmetric Standard Model (MSSM) is the simplest supersymmetric extension of the Standard Model since it requires a minimal number of new particles and interactions that are consistent with the SM gauge group. It respects the same $SU(3)_C \otimes SU(2)_L \otimes U(1)_Y$ gauge symmetry as the SM.

The fermions (quarks and leptons) belong to chiral supermultiplets[3] together with spin-0 sfermions (squarks and sleptons). The gauge bosons (photon, gluon, $W^{\pm}$, Z^0) belong to the vector supermultiplets together with the Majorana spin-$\frac{1}{2}$ gauginos (photino, gluino, wino, zino).

The MSSM requires two Higgs doublets for two reasons. The first reason is that since the SM fermions have exactly the right quantum numbers to cancel the triangle $SU(2)_L$ and $U(1)_Y$ gauge anomalies, the contribution from the fermionic partner of the Higgs doublet remains uncancelled. The second reason is that two Higgs doublets are required in order to give both the up and down quarks masses. Therefore, the Higgs boson is paired with a spin-$\frac{1}{2}$ Higgsino in a chiral multiplet.

[3]SM fermions are chiral since their left and right handed components transform differently under $SU(2)_L \otimes U(1)_Y$

The exact nature of the Supersymmetry breaking mechanism is unknown, but it can be incorporated by adding explicitly soft SUSY breaking terms consistent with the symmetries of the SM. For the MSSM [15] they consist of:

- gaugino masses (M_1, M_2, M_3 for each $U(1)$, $SU(2)$ and $SU(3)$ gauge groups);
- mass terms for various left and right spin 0 (squarks, sleptons, Higgs) fields;
- trilinear (A-term) interactions amongst the scalars and
- analogous bilinear (B-term) interactions.

In addition to those soft-breaking terms, the ratio, $\tan\beta$, of the two Higgs vacuum expectation value, Vevs, and a supersymmetric Higgsino mixing parameter μ must be specified. In the unconstrained MSSM, the above terms are considered to be free parameters of the theory. The large number of unknowns can be reduced if a particular SUSY breaking mechanism is employed.

1.3.3 Minimal Supergravity (MSUGRA)

The minimal Supergravity model (MSUGRA) is based on a local version of supersymmetry. Since invariance under local SUSY transformations implies invariance under local coordinate change (which is the underlying principle of the theory of General Relativity), gravity is naturally included. In this model, supersymmetry is broken in the *hidden sector* [18] and transmitted to the *visible sector* via gravitational interactions [19].

In this model it is assumed that the gauge couplings unify at the scale $M_x \sim 10^{16}$ GeV as motivated by Figure 1.6 which shows that the three gauge couplings do meet at this scale. It is further assumed that at this energy scale, the masses of all scalar partners ($\tilde{q}$ and $\tilde{l}$) take a common value of m_0, the gauginos masses unify at $M_i(M_x) = m_{\frac{1}{2}}$, the trilinear parameters have the same value A_0 and the neutral Higgs boson masses are equal to $M_{h,H} = \sqrt{m_0^2 + \mu^2}$, where μ is the Higgs mass parameter (see section 1.3.5). Figure 1.7 shows the masses from the M_x down to the electroweak scale predicted through the supersymmetric renormalisation group equations (RGEs).

One can notice that m_h^2 goes negative toward the electroweak scale. This introduces the breaking of electroweak symmetry. This mechanism only works in the case of $M_{top} \sim 175$ GeV/c^2 [20].

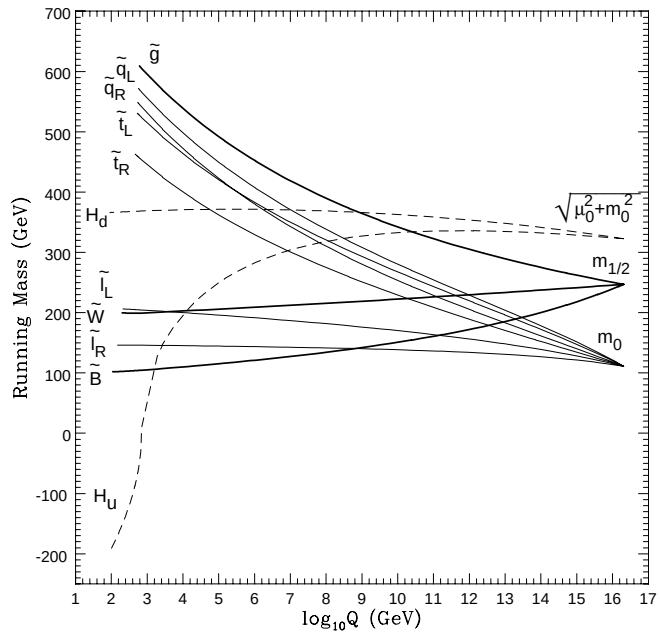

Figure 1.7: Running of the sparticle masses from the GUT scale to the electroweak scale for a particular choice of model parameters [23]. The bold lines are the three soft gaugino masses, $m_{\tilde{g}}$, M_2 (labeled $\tilde{W}$) and M_1 (labelled $\tilde{B}$). The light solid lines are the squarks ($\tilde{q}_L$, $\tilde{q}_R$, $\tilde{t}_L$, $\tilde{t}_R$) and slepton soft masses ($\tilde{l}_L$, $\tilde{l}_R$). Finally the dashed lines represent the soft Higgs masses, M_h and M_H, labelled by H_d and H_u.

At the electroweak scale, the gaugino mass terms are related by:

$$M_1 = \frac{5}{3}\tan^2\theta_W M_2 \tag{1.20}$$

$$M_3 = \frac{\alpha_3}{\alpha_{em}}\sin^2\theta_W M_2 \tag{1.21}$$

With this set of assumptions and the further requirement that the Z^0 boson mass acquires its measured value when the parameters are evaluated at a lower scale, the SUSY sector requires 5 free parameters:

$$m_0,\ m_{\frac{1}{2}},\ A_0,\ \tan\beta,\ \mathrm{sign}(\mu) \tag{1.22}$$

In addition, as in the SM, the top mass, m_t, must be specified.

Furthermore, within the MSUGRA framework, R-Parity (see Section 1.3.4) is assumed to be conserved.

1.3.4 R-parity conservation

In constructing MSSM, there are terms that allow for violation of Baryon number (B) or Lepton number (L). A solution to the problem is to introduce a new symmetry

called R-Parity which forbids the undesirable lepton and baryon number violating terms. R-Parity is defined as a multiplicative quantum number such that all SM particles have R-Parity +1, while all superpartners have R-Parity -1. R-Parity can be written as:

$$\mathrm{R} = (-1)^{3\mathrm{B}+\mathrm{L}+2\mathrm{s}} \tag{1.23}$$

where s is the particle spin.

The assumption of R-Parity conservation has profound phenomenological consequences. Firstly, it implies that SUSY particles must be pair produced from SM particles. Secondly, the lightest supersymmetric partner (LSP) must be stable. Cosmological constraints favour an LSP which is neutral in electric and colour charge [24]. Hence the LSP is stable and neutral and thus escapes experimental detection. Therefore the LSP is an excellent candidate for dark matter and is generally assumed to be the lightest neutralino χ_1^0. Furthermore, SUSY particles will decay into a state which contains an odd number of LSP, typically one. Experimentally this means that the search for supersymmetric particles is characterised by the missing energy from the non-observed LSP.

1.3.5 Particle spectrum

In this section the particle spectrum in the context of MSSM is described (see Table 1.3).

Higgs

The Higgs scalar fields of the MSSM consist of two complex $SU(2)_L$ doublets each of which have four degrees of freedom. When electroweak symmetry is broken, three of them become the longitudinal modes of the Z^0 and $W^{\pm}$ massive vector bosons. The remaining five Higgs scalar mass eigenstates consist of one CP-odd neutral scalar A, a charge +1 scalar H^+ and its conjugate charge -1 scalar H^- and two CP-even neutral scalars h and H. After fixing $v_1^2 + v_2^2$ so that the W boson get its mass according to the equation:

$$\mathrm{M}_W^2 = \frac{g^2}{2}(v_1^2 + v_2^2) \tag{1.24}$$

the Higgs sector can be described with two additional parameters:

$$\tan\beta = \frac{v_2}{v_1} \tag{1.25}$$

Quarks				Squarks				
(spin$\frac{1}{2}$)	$\begin{pmatrix} \mathrm{u} \\ \mathrm{d} \end{pmatrix}_L$	$\mathrm{u_R}$	$\mathrm{d_R}$	(spin0)	$\begin{pmatrix} \tilde{\mathrm{u}} \\ \tilde{\mathrm{d}} \end{pmatrix}_L$	$\tilde{\mathrm{u}}_R$	$\tilde{\mathrm{d}}_R$	
	$\begin{pmatrix} \mathrm{c} \\ \mathrm{s} \end{pmatrix}_L$	$\mathrm{c_R}$	$\mathrm{s_R}$		$\begin{pmatrix} \tilde{\mathrm{c}} \\ \tilde{\mathrm{s}} \end{pmatrix}_L$	$\tilde{\mathrm{c}}_R$	$\tilde{\mathrm{s}}_R$	
	$\begin{pmatrix} \mathrm{t} \\ \mathrm{b} \end{pmatrix}_L$	$\mathrm{t_R}$	$\mathrm{b_R}$		$\begin{pmatrix} \tilde{\mathrm{t}} \\ \tilde{\mathrm{b}} \end{pmatrix}_L$	$\tilde{\mathrm{t}}_R$	$\tilde{\mathrm{b}}_R$	$\rightarrow \tilde{\mathrm{t}}_{1,2}, \tilde{\mathrm{b}}_{1,2}$
Leptons				Sleptons				
(spin$\frac{1}{2}$)	$\begin{pmatrix} \mathrm{e} \\ \nu_e \end{pmatrix}_L$	$\mathrm{e_R}$		(spin0)	$\begin{pmatrix} \tilde{\mathrm{e}} \\ \tilde{\nu_e} \end{pmatrix}_L$	$\tilde{\mathrm{e}}_R$		
	$\begin{pmatrix} \mu \\ \nu_\mu \end{pmatrix}_L$	μ_R			$\begin{pmatrix} \tilde{\mu} \\ \tilde{\nu_\mu} \end{pmatrix}_L$	$\tilde{\mu}_R$		
	$\begin{pmatrix} \tau \\ \nu_\tau \end{pmatrix}_L$	τ_R			$\begin{pmatrix} \tilde{\tau} \\ \tilde{\nu_\tau} \end{pmatrix}_L$	$\tilde{\tau}_R$		$\rightarrow \tilde{\tau}_{1,2}$
Gauge bosons				Gauginos				
(spin1)	g			(spin$\frac{1}{2}$)	$\tilde{\mathrm{g}}$			
	γ				$\tilde{\gamma}$			Neutralinos
	Z				$\tilde{\mathrm{Z}}$			$\rightarrow \tilde{\chi}^0_{1,2,3,4}$
	$\mathrm{W}^\pm$				$\tilde{\mathrm{W}}^\pm$			$\{\tilde{\gamma}, \tilde{\mathrm{Z}}, \tilde{\mathrm{H}}^0_{1,2}\}$
Higgs bosons				Higgsinos				Charginos
(spin0)	h, H, A			(spin$\frac{1}{2}$)	$\tilde{\mathrm{H}}^0_{1,2}$			$\rightarrow \tilde{\chi}^\pm_{1,2}$
	$\mathrm{H}^\pm$				$\tilde{\mathrm{H}}^\pm$			$\{\tilde{\mathrm{W}}^\pm, \tilde{\mathrm{H}}^\pm\}$

Table 1.3: Particles of the MSSM. Arrows indicate fields that mix due to the Yukawa interactions and the corresponding physical fields that result.

and M_A, the mass of the pseudo-scalar Higgs boson. The masses of the different Higgs can then be expressed in terms of M_A and $tan\beta$:

$$M_A^2 = m_1^2 + m_2^2 + 2\mu^2 \tag{1.26}$$

$$M_{H^\pm}^2 = M_A^2 + M_W^2 \tag{1.27}$$

$$M_{h,H}^2 = \frac{1}{2}\left(M_A^2 + M_Z^2 \mp \sqrt{(M_A^2 + M_Z^2)^2 - 4M_A^2 M_Z^2 \cos^2 2\beta}\right) \tag{1.28}$$

The MSSM seems to predict that one of the neutral Higgs scalar must be lighter than the Z boson: $m_{h^0} < M_Z|\cos\ 2\beta|$. However, after taking into account the radiative corrections, one obtains the upper bound:

$$\mathrm{m}_{h^0} \leq 130\ \mathrm{GeV}/c^2\ [21] \tag{1.29}$$

which is in agreement with the EW precision measurements[4].

Sleptons

Below the electroweak breaking scale, fields with different $SU(2)_L \otimes U(1)_Y$ quantum numbers can mix if they have the same $SU(3)_C \otimes\ U(1)_{Em}$ quantum numbers. Thus, for example, the superpartner of the τ^-, the $SU(2)_L$ doublet and singlet fields, $\tilde{\tau}_L^-$ and $\tilde{\tau}_R^-$, respectively, have identical quantum numbers and thus can mix. Furthermore, since the gauge interactions of the sfermions are the same as for the SM fermions, a left-handed slepton will couple to the W boson, while the right-handed will not.

In the context of MSUGRA, the following equations describe the slepton masses at the electroweak scale [22]:

$$M_{\tilde{\nu}_l}^2 = m_0^2 + \frac{1}{4}C_1 + C_2 + \frac{1}{2}M_Z^2 \cos\ 2\beta \tag{1.30}$$

$$M_{\tilde{l}_L}^2 = m_0^2 + \frac{1}{4}C_1 + C_2 - (\frac{1}{2} + \sin^2\theta_W)M_Z^2 \cos\ 2\beta \tag{1.31}$$

$$M_{\tilde{l}_R}^2 = m_0^2 + C_1 - \sin^2\theta_W M_Z^2 \cos\ 2\beta \tag{1.32}$$

with $C_1 = -\frac{2}{11}M_1^2(1 - \frac{\alpha^2(M_x)}{\alpha_1^2}))$ and $C_2 = -\frac{3}{2}M_2^2(1 - \frac{\alpha^2(M_x)}{\alpha_2^2}))$

The slepton's masses are obtained by the diagonalisation of the following mass matrix:

$$\begin{pmatrix} M_{\tilde{l}_L}^2 + m_l^2 & m_l(A_l + \mu\tan\beta) \\ m_l(A_l + \mu\tan\beta) & M_{\tilde{l}_R}^2 + m_l^2 \end{pmatrix} \tag{1.33}$$

[4]This assumes that all the sparticles that can contribute to $\Delta(m_{h^0}^2)$ in loops have masses that do not exceed 1 TeV.

For the first two lepton generations, one can approximate $m_l = 0$ and therefore the mass eigenstate are $\tilde{l}_R$ and $\tilde{l}_L$. However for the third generation, $m_\tau = 1.777$ GeV/c^2, thus one obtains two mass eigenstates $(\tilde{\tau}_1, \tilde{\tau}_2)$ which are a mixture of $\tilde{\tau}_R$ and $\tilde{\tau}_L$:

$$\begin{pmatrix} \tilde{\tau}_1 \\ \tilde{\tau}_2 \end{pmatrix} = \begin{pmatrix} \cos\theta_{\tilde{\tau}} & \sin\theta_{\tilde{\tau}} \\ -\sin\theta_{\tilde{\tau}} & \cos\theta_{\tilde{\tau}} \end{pmatrix} \begin{pmatrix} \tilde{\tau}_L \\ \tilde{\tau}_R \end{pmatrix} \tag{1.34}$$

where the mixing angle $\theta_{\tilde{\tau}}$ is defined by:

$$\theta_{\tilde{\tau}} = \frac{1}{2}\arctan\left(2m_\tau \frac{(A_\tau + \mu\ \tan\beta)}{M^2_{\tilde{\tau}_L} - M^2_{\tilde{\tau}_R}}\right) \tag{1.35}$$

At the electroweak scale, the stau will be the lightest slepton due to the presence of the diagonal terms in equation 1.33 and their larger evolution due to Yukawa couplings.

Charginos

The charged Higgsinos $(\tilde{H}^+, \tilde{H}^-)$ and winos $(\tilde{W}^+, \tilde{W}^-)$ mix to form the two mass eigenstates called charginos $(\tilde{\chi}^\pm_1, \tilde{\chi}^\pm_2)$ obtained by the diagonalisation of the mass matrix:

$$\begin{pmatrix} M_2 & \sqrt{2}M_W\ \sin\beta \\ \sqrt{2}M_W\ \cos\beta & \mu \end{pmatrix} \tag{1.36}$$

The nature of the chargino is important. Depending if the chargino is Higgsino like or wino like, the interactions with other particles will be different and therefore the cross sections and branching ratios will change.

Furthermore, in the limit of $|\mu + M_2| >> M_Z$, mass eigenstates of the charginos consist of a wino like, $\tilde{\chi}^\pm_1$ and a higgsino like $\tilde{\chi}^\pm_2$, and their masses can be approximated to:

$$M_{\tilde{\chi}^\pm_{1,2}} = M_2 \mp \frac{M^2_W(M_2 + \mu\ \sin 2\beta)}{\mu^2 - M^2_2} \tag{1.37}$$

In this case, the lighter chargino, $\tilde{\chi}^\pm_1$, is wino $(\sim \tilde{W}^\pm)$ while $\tilde{\chi}^\pm_2$, is Higgsino $(\sim \tilde{H}^\pm)$.

Neutralinos

Neutralinos are a mixture of the photino $(\tilde{\gamma})$, the zino $(\tilde{Z})$ and the two neutral higgsinos $(\tilde{H}^0_{1,2})$. The four mass eigenstates $(\tilde{\chi}^0_{1,2,3,4})$ can be obtained by the diago-

nalisation of the following matrix:

$$\begin{pmatrix} M_1 & 0 & -M_Z\cos\beta\sin\theta_W & M_Z\sin\beta\sin\theta_W \\ 0 & M_2 & M_Z\cos\beta\cos\theta_W & -M_Z\sin\beta\cos\theta_W \\ -M_Z\cos\beta\sin\theta_W & M_Z\cos\beta\cos\theta_W & 0 & -\mu \\ M_Z\sin\beta\sin\theta_W & -M_Z\sin\beta\cos\theta_W & -\mu & 0 \end{pmatrix} \tag{1.38}$$

In the limit of $|\mu + M_2| >> M_Z$, the mass eigenstates of the the lightest neutralino, $(\tilde{\chi}_1^0)$ and the second lightest,$(\tilde{\chi}_2^0)$, can be approximated to:

$$M_{\tilde{\chi}_1^0} = M_1 - \frac{M_z^2 \ \sin^2\theta_W(M_1 + \mu \ \sin \ 2\beta)}{\mu^2 - M_1^2} \tag{1.39}$$

$$M_{\tilde{\chi}_2^0} = M_2 - \frac{M_W^2(M_2 + \mu \ \sin \ 2\beta)}{\mu^2 - M_2^2} \tag{1.40}$$

1.4 Supersymmetric Channels

This section describes the production and decay of the supersymmetric partner of the tau lepton at LEP2. The prospects of observing a supersymmetric signal in the trilepton channel from the associated production of the $\tilde{\chi}_1^{\pm}\tilde{\chi}_2^0$, with the CDF experiment at the TEVATRON in Run IIa, are discussed.

1.4.1 Supersymmetric Scalar Tau at LEP

As mentioned in Section 1.3.5, the stau is predicted to be the lightest slepton and hence has the highest discovery potential since it is more accessible kinematically.

The staus can be pair produced with an e^+e^- collider by the s-channel diagram shown in Figure 1.8. For a large part of the MSSM, the right-handed stau is predicted to have a lower mass than the left handed stau. A conservative approach is adopted by assuming that $m_{\tilde{\tau}_L} > E_{beam}$ which is indeed conservative since the cross section for left-handed stau is typically larger than that of the right-handed one. Hence in this study, the mixing angle, $\theta_{\tilde{\tau}}$, is set to $\frac{\pi}{2}$ which corresponds to the case where the lightest stau is a right-handed stau ($\tilde{\tau}_1 \equiv \tilde{\tau}_R$).

Typically, the predicted cross section of the right-handed staus varies from 0.2 to 1 pb for $m_{\tilde{\tau}_R}$ between 30 to 70 GeV/c^2, at a centre of mass energy of 189 GeV (see Figure 1.9a). Assuming R-parity conservation, the stau decays predominantly to a

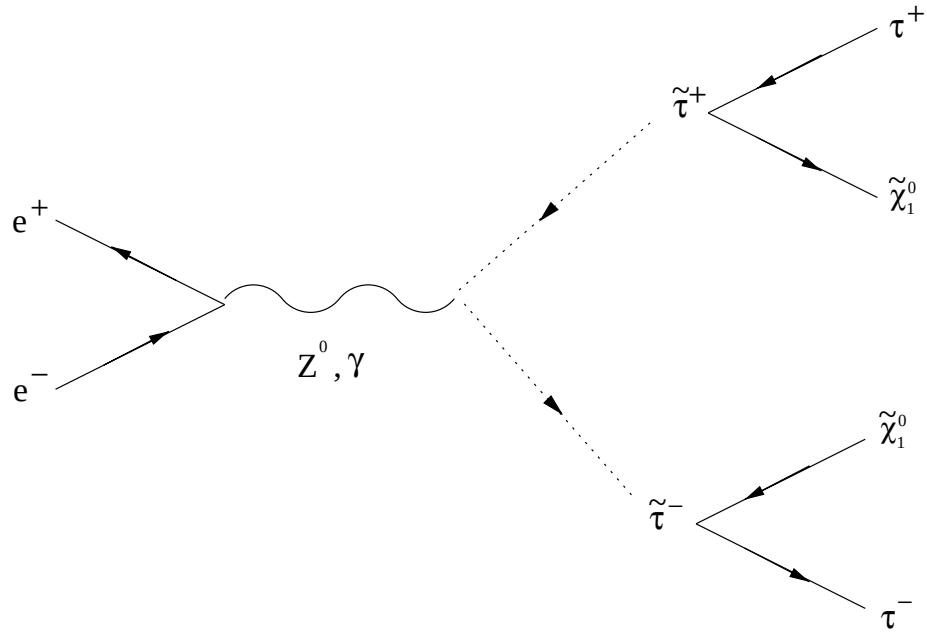

Figure 1.8: Production and decay diagram for the stau

tau and the lightest neutralino:

$$\tilde{\tau}_R^{\pm} \rightarrow \tau + \tilde{\chi}_1^0 \tag{1.41}$$

Figure 1.9b shows the branching ratio for this decay channel for the parameters ($\mu = -200$ GeV/c^2 and $\tan\beta = 1.5$) recommended by the LEP SUSY Working Group [10]. In this case the branching ratio is almost always at 100%. However when the neutralino $\tilde{\chi}_1^0$ has a small mass, two other decay channels, $\tilde{\tau}_R^{\pm} \rightarrow \tau^{\pm} + \tilde{\chi}_2^0$ and $\tilde{\tau}_R^{\pm} \rightarrow \nu_\tau + \tilde{\chi}_1^{\pm}$ open. The subsequent decay of the second lightest neutralino $\tilde{\chi}_2^0$ and the chargino $\tilde{\chi}_1^{\pm}$ introduce new topologies which are not considered in the stau search presented in this thesis.

Since the neutralino escapes undetected, the signal topology consists of an acoplanar tau pair with missing energy. Figure 1.10 shows an event display of a MC stau event generated for $\mu = -200$ GeV/c^2, $\tan\beta = 1.5$ and ($\tilde{\tau}_R$,$\tilde{\chi}_1^0$) signal of (80,20) GeV/c^2. The event shows four acoplanar tracks, where three of them deposits energy in the electromagnetic and hadron calorimeters ($\tau \rightarrow 3\pi\nu_\tau$) and where the other track showers in the electromagnetic calorimeter ($\tau \rightarrow e\nu_e\nu_\tau$). The arrow indicates the direction of the missing energy.

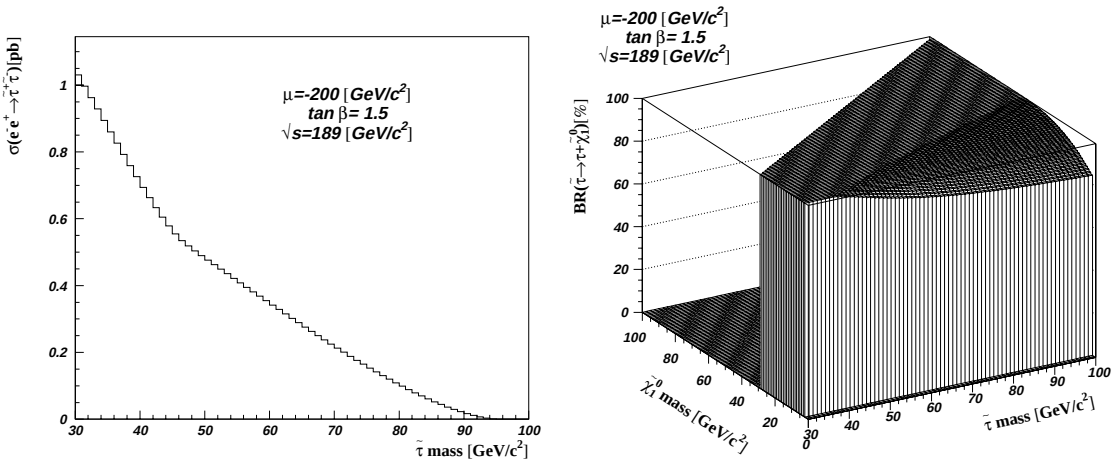

(a) (b)

Figure 1.9: Stau production cross section and branching ratio $BR(\tilde{\tau}_R^{\pm} \rightarrow \tau + \tilde{\chi}_1^0)$. Both plots were generated using SUSYGEN 3.00 [25] assuming MSSM parameters $\mu = -200$ GeV/c^2, $\tan\beta = 1.5$ at a centre of mass energy of 189 GeV.

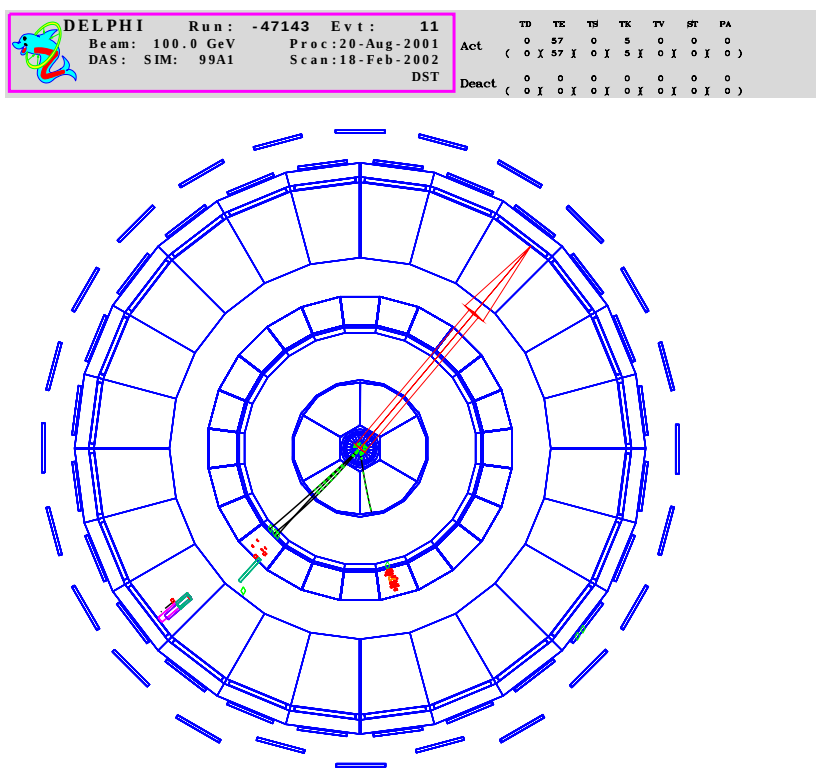

Figure 1.10: Event display of a MC stau event generated at 200 GeV with $\mu = -200$ GeV/c^2, $\tan\beta = 1.5$ and $(\tilde{\tau}_R, \tilde{\chi}_1^0)$ signal of (80,20) GeV/c^2. One of the τ decays hadronically ($\tau \rightarrow 3\pi\nu_\tau$), while the other one decays to an electron and a neutrino ($\tau \rightarrow e\nu_e\nu_\tau$). The arrow indicates the direction of the missing energy.

1.4.2 Trilepton signal from $\tilde{\chi}_1^{\pm}\tilde{\chi}_2^0$ associated production at CDF

The trilepton signal plus missing transverse energy ($3l+\not{E}_T$) is one of the most promising channels for SUSY discovery at the TEVATRON. In the MSUGRA, the associated production of lightest chargino, $\tilde{\chi}_1^{\pm}$, and the second lightest neutralino, $\tilde{\chi}_2^0$, that could be produced, cascade decay to a final state with three leptons and missing transverse energy ($3l+\not{E}_T$) for some regions of the parameter space. The $\tilde{\chi}_1^{\pm}$ $\tilde{\chi}_2^0$ production occurs via quarks-antiquarks annihilation in the s-channel through the W boson exchange and in the t and u-channel through squark ($\tilde{q}$) exchange (see Figure 1.11).

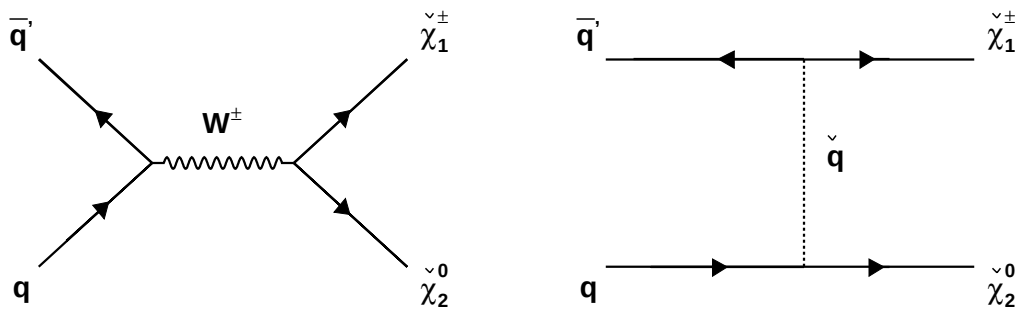

Figure 1.11: Feynman diagrams for $q\bar{q}' \to \tilde{\chi}_1^{\pm}\tilde{\chi}_2^0$

The production cross section depends on the masses of chargino ($m_{\tilde{\chi}_1^{\pm}}$) and neutralino ($m_{\tilde{\chi}_2^0}$). If the squarks are much heavier that the gauginos, the s-channel dominates, if however the squarks are light, a destructive interference between the W-boson and the squarks exchange amplitudes can suppress the cross section by as much as 40% compared to the s-channel contribution alone. At the TEVATRON, the pair production $\tilde{\chi}_1^{\pm}$ $\tilde{\chi}_2^0$ dominates over the strongly produced $\tilde{g}\tilde{g}$, $\tilde{g}\tilde{q}$, $\tilde{q}\tilde{q}$ over essentially all of the parameter space for which $|\mu| >> M_1 + M_2$.

Once the $\tilde{\chi}_1^{\pm}$ and $\tilde{\chi}_2^0$ are produced, they decay through a cascade of decays with lighter sparticles until the decay terminates with the production of the LSP ($\tilde{\chi}^0$). Sparticle branching fractions are a complicated function of the SUSY model parameter space.

Figure 1.12 shows the Feynman diagrams of the $\tilde{\chi}_1^{\pm}$ (a) and $\tilde{\chi}_2^0$ (b) decays into final states of leptons and neutralino. The chargino decays to a lepton, neutrino and neutralino ($\tilde{\chi}_1^{\pm} \to l\nu\tilde{\chi}_1^0$) via a slepton ($\tilde{e}$, $\tilde{\mu}$ or $\tilde{\tau}$), a sneutrino ($\tilde{\nu}$) or a W boson.

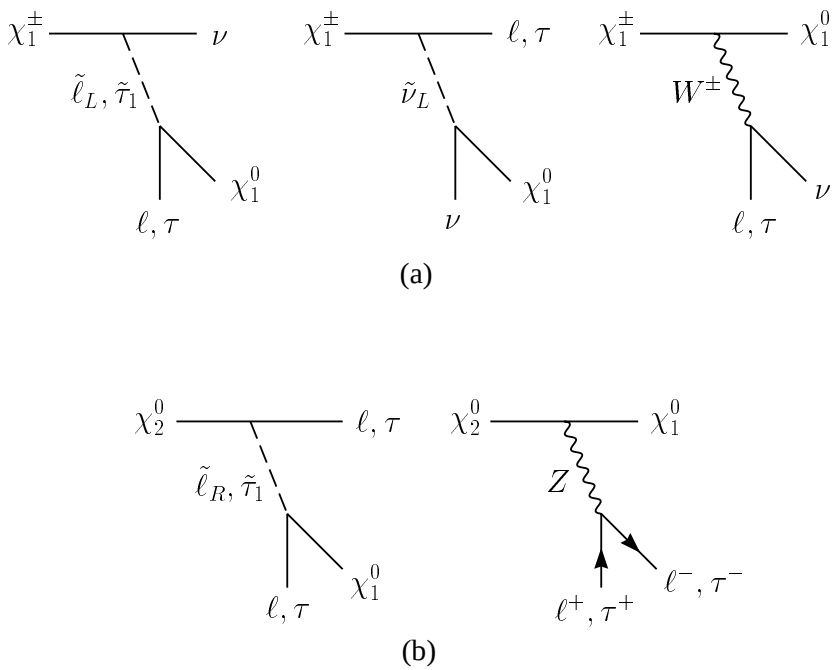

Figure 1.12: Feynman diagrams for (a) $\tilde{\chi}_1^\pm \to l\nu\tilde{\chi}_1^0$ and (b) $\tilde{\chi}_2^0 \to \tilde{\chi}_1^0 l^+ l^-$, where $l = e, \mu$.

The second lightest neutralino ($\tilde{\chi}_2^0$) decays to two leptons and a neutralino ($\tilde{\chi}^0$) via a slepton or a Z boson.

Regardless of the intermediate stages, the final state always involves a lepton-antilepton pair, an additional lepton, a neutrino and two $\tilde{\chi}_1^0$. Since $\tilde{\chi}_1^0$ escapes undetected, the signal topology to search for is 3 leptons and missing transverse energy, $\not{E}_T$. The direction of the escaping neutrino and two $\tilde{\chi}_1^0$ are uncorrelated and therefore the amount of $\not{E}_T$ can vary from a small to a substantial amount. In the case where the τ lepton decays leptonically, this channel can offer a very distinctive trilepton signature with very little Standard Model background.

The mass distribution of the same flavor, opposite sign dileptons, $m_{l\bar{l}}$, can provide important information about the neutralino, and possibly also slepton, masses [59]. It is expected that with a sufficiently large trilepton signal, a mass end point should be visible. In the case where $\tilde{\chi}_2^0 \to l\tilde{l}\tilde{\chi}_1^0$ via a real slepton, $\tilde{l_R}$, an edge is expected at:

$$m_{l\bar{l}}^{max} = m_{\tilde{\chi}_2^0}\sqrt{1 - \frac{m_{\tilde{l}_R}^2}{m_{\tilde{\chi}_2^0}^2}}\sqrt{1 - \frac{m_{\tilde{\chi}_1^0}^2}{m_{\tilde{l}_R}^2}} \tag{1.42}$$

In the cases where the leptons arise as secondaries from the τ decay that is produced from the $\tilde{\chi}_2^0$, the dilepton mass distribution will rise at lower mass values, and the sharp edge will disappear.

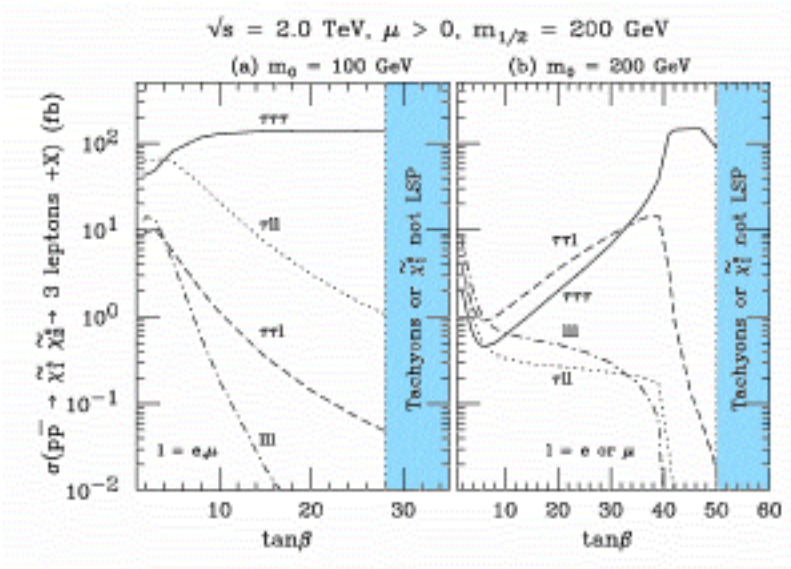

Figure 1.13: Cross section $p\bar{p} \to \tilde{\chi}_1^{\pm}\tilde{\chi}_2^0 \to 3l + X$ without cuts versus $\tan\beta$, with $\mu > 0$, and with $m_{1/2} = 200$ GeV/c^2, for $m_0 = 100$ GeV/c^2 for 4 final states: $\tau\tau\tau$ (solid), $\tau\tau l$ (dot-dash), τll (dash) lll (dot) where $l = \mu$ or e.

Figure 1.13 shows the predicted cross sections of $p\bar{p} \to \tilde{\chi}_1^{\pm}\ \tilde{\chi}_2^0 \to 3l + X$ for $m_0 =$ 100 GeV/c^2 and 200 GeV/c^2, $\mu > 0$ and $m_{1/2} = 200$ GeV/c^2. For $m_0 = 100$ GeV/c^2, the dominating final state involves three τ's over the whole $\tan\beta$ range, followed by τll, $\tau\tau l$ and lll (where $l = e, \mu$) which decrease as a function of $\tan\beta$. For $m_0 = 200$ GeV/c^2, the cross sections are lower and the dominating final states are $\tau\tau l$ and three τ's which increase as a function of $\tan\beta$ and lll which decreases as a function of $\tan\beta$. Therefore, the detection of tau leptonic decays would increase the reach in the discovery of a trilepton signal over a larger range of the parameter space.

Monte Carlo studies [63] have investigated the prospects of detecting the SUSY trilepton signal at the TEVATRON. The results show that with soft but realistic lepton p_T cuts, the leptonic decay of the τ can substantially enhance the statistical significance of the trilepton signal. Figure 1.14 shows the 99% C.L. for Run IIa (2 fb^{-1}) observation contour in the $(m_{1/2}, m_0)$ plane for the SUSY trilepton channel for the MSUGRA parameters $\tan\beta = 2$, $\mu > 0$ and $A_0 = 0$.

It is worth noticing, that by tagging the hadronic decay of one of the tau, one could increase the number of trilepton events by as much as a factor of 6. This would increase the potential of observing a trilepton signal as well as increasing the region

of the SUSY parameter space that can be probed.

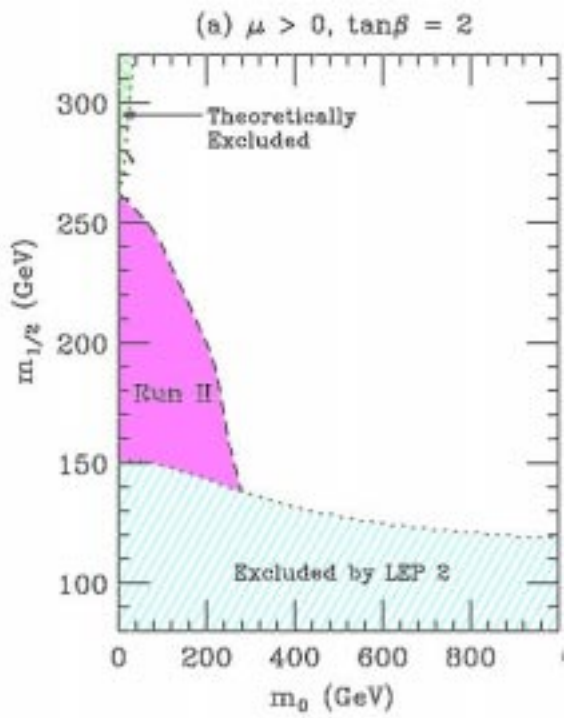

Figure 1.14: Contours for the 99% C.L. for Run IIa (2 fb^{-1}) in the $(m_{1/2}, m_0)$ plane for the SUSY trilepton channel for the MSUGRA parameters $\tan\beta = 2$, $\mu > 0$ and $A_0 = 0$.

In conclusion, for $m_0 = 100$ GeV/c^2 and $\tan\beta = 2$, the trilepton signal could be seen at Run IIa if $m_{1/2} \leq 240$ GeV/c^2 ($m_{\tilde{\chi}_1^\pm} \leq 177$ GeV/c^2). The observation of the SUSY trilepton signal could possibly be enhanced if the hadronic tau decay could be efficiently tagged while keeping the Standard Model backgrounds under control [64]. In the eventuality that a signal is not observed, a substantial region of the parameters space not accessible at LEP2 can be probed and the lightest chargino mass could be excluded up to ~ 200 GeV/c^2.

Chapter 2

The DELPHI detector and the LEP accelerator

2.1 Introduction

This chapter introduces the LEP e^+e^- accelerator at CERN and the DELPHI experiment which is one of the four general purpose experiments. The DELPHI detector consists of a series of sub-detectors which provide tracking information for charged particles, calorimetry energy deposit, muon identification and luminosity measurement. After a brief description of the LEP machine, the DELPHI detector is presented in more detail, with special attention paid to the features important to this analysis.

2.2 The LEP Accelerator

The Large Electron-Positron (LEP) collider is located on the French-Swiss border at the European Laboratory for Particle Physics (CERN). Its main goal is the detailed study of electroweak interactions, both by performing precise measurements of the relevant physical quantities and by searching for new physics. In its first phase (LEP1: 1989 to 1995) LEP was operating at a centre of mass energy ($\sqrt{s}$) very close to the Z^0 mass (91.188 GeV). The large statistical sample of events accumulated allowed very precise measurements to be performed. The increase of the centre of mass energy was started in November 1995 entering the second phase (LEP2). W^+W^- pairs were produced for the first time at LEP in summer 1996 at $\sqrt{s} \simeq 161$ GeV. This second phase took LEP to an energy of 209 GeV in summer

2000. The data studied in this thesis were those taken during the 1998 and 1999 period at $\sqrt{s} = 189$ to 202 GeV.

2.2.1 The LEP ring

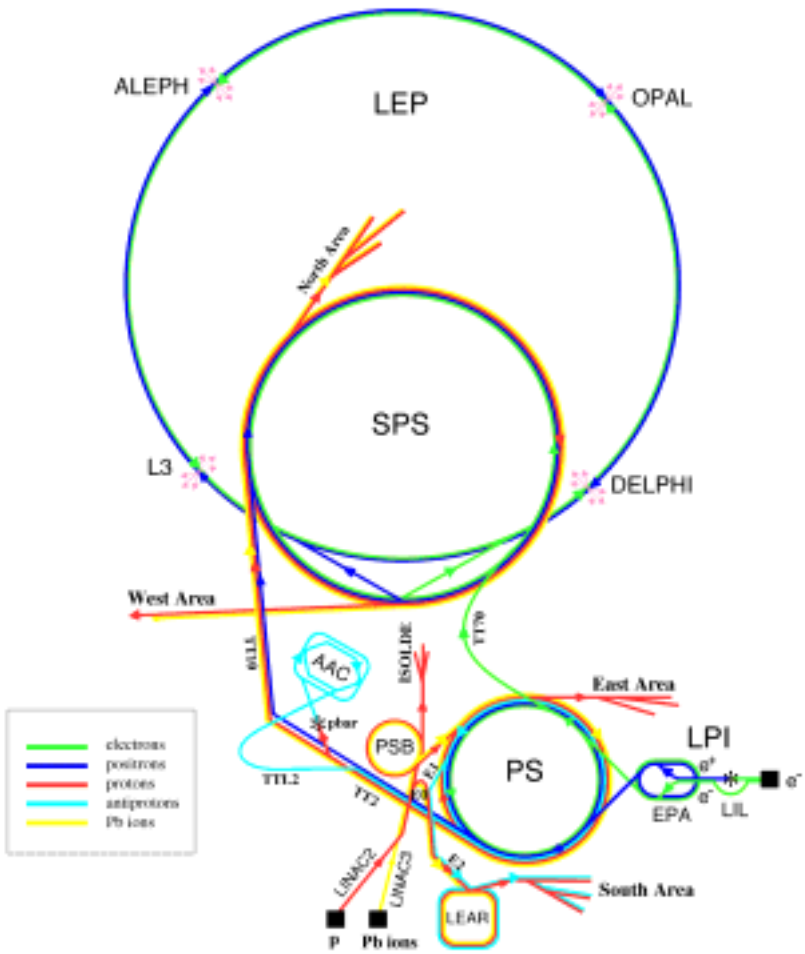

Figure 2.1: The CERN accelerators. The following description includes only components used by LEP. LEP: Large Electron Positron collider, SPS: Super Proton Synchrotron, PS: Proton Synchrotron, LPI: LEP Pre-Injector, EPA: Electron Positron Accumulator, LIL: LEP Injector Linac.

The LEP ring is 26.7 km in circumference and lies within a stable layer of rock at an average depth of about 100 m below the surface. The tunnel was excavated as a sequence of straight sections and arcs; the ring consists of eight lengths of each type. The four experiments, ALEPH, DELPHI, L3 and OPAL are situated in the middle of the alternate straight sections. Positioning the detectors in the straight sections protects the experiments from synchrotron radiation from the beams. Mid-

way along each section, where the beams are brought into collision at the centre of each experiment, is the interaction point.

The acceleration of electrons and positrons to such high energies requires a complex chain that uses the other accelerators available at CERN (see Figure 2.1). The positrons are produced by the collision of 200 MeV electrons with a tungsten target. Electrons and positrons are then accelerated to 600 MeV at the LIL (Linear Injector-LEP) and accumulated in the storage ring EPA (Electron-Positron Accumulator). When the currents reach a certain value the beams are injected in the PS (Proton Synchrotron) where they are accelerated to a maximum energy of 3.5 GeV and then in the SPS (Super Proton Synchrotron) where they reach an energy of about 20 GeV prior to injection into LEP.

The e^+e^- beams are then accelerated to the desired energy for collision using radio frequency (RF) cavities located in the straight sections, while dipole magnets guide the beams through the curved sections. Once the required acceleration has been achieved, LEP is operated as a storage ring, and the cavities are used to replace the energy lost by the particles in synchrotron radiation. The copper cavities used during the first phase of LEP were replaced by superconducting cavities to allow for the acceleration of the e^+e^- pairs to higher energies required for the LEP2 running. In order to achieve a long beam lifetime, the rate of particle loss due to collisions with residual gas molecules in the beam pipe, is minimised by keeping the LEP beam pipe at low pressure.

The bunches of each beam must be tightly focused ("squeezed") at the interaction point in order to maximise the luminosity $\mathcal{L}$. This is accomplished by a set of superconducting quadrupole and sextupole magnets situated a few meters away the interaction points. The very strong field gradients allow to focus the beams to typical dimensions of ~ 10 μm in the vertical plane, ~ 150 μm in the horizontal plane and ~ 2 cm along the beam direction.

The number of particle per bunch is of the order of $2 \cdot 10^{11}$. The number of bunches per beam is 4. Additionally at LEP2, the bunches can be divided into bunchlets of particles. The interval between collisions is ~ 22 μs.

Luminosity

For a storage ring such as LEP, if the electron and positron beams overlap completely, the luminosity is given approximately by:

$$\mathcal{L} = \frac{n_b N_e N_p f}{4\pi\sigma_x\sigma_y} \; [cm^{-2}s^{-1}] \tag{2.1}$$

where n_b is the number of bunches per beam, f is the frequency of revolution, N_e and N_p are the number of electrons and positrons per bunch respectively and σ_x and σ_y are the *rms* spread of each bunch in the horizontal and vertical planes respectively.

Thus, the total number of events observed by each detector is related to the total cross section, σ_T, by the time integral:

$$N = \int \mathcal{L}_t \epsilon_t \sigma_T dt \tag{2.2}$$

where ϵ_t is the efficiency of the detector.

Since the luminosity relates the event rate of a given process to its cross-section, an accurate measurement of the luminosity is important in the determination of cross sections and other quantities derived from them. At LEP, the luminosity is measured using equation 2.2 by obtaining the event rate for a high statistics process whose cross section is theoretically known with great precision. This process is Bhabha scattering $e^+e^- \rightarrow e^+e^-$. The luminosity integrated over a certain period will be given by:

$$L = \int_{\Delta\ t} \mathcal{L} dt \; = \; \frac{N}{\sigma_{eff}} \; [pb^{-1}] \tag{2.3}$$

where $N = N^{meas} - N^{back}$ is the number of events after background subtraction and the effective cross section $\sigma_{eff} = \sigma\varepsilon_a\varepsilon$ is obtained from the theoretical cross section (σ) by correcting for the effects of geometrical acceptance (ε_a) and Bhabha identification efficiency (ε).

2.3 The DELPHI Detector

The DELPHI Detector (Detector with Lepton, Photon and Hadron Identification) is the most elaborate of the four general purpose LEP experiments. The design aims for high tracking efficiency and good calorimetry performance over nearly the full solid angle. The detector includes both powerful particle identification capabilities and precise vertex determination.

The standard DELPHI coordinate system is defined as follows: the z axis is along the electron LEP beam direction, the x axis points towards the centre of LEP and the y axis points upwards. The polar angle with respect to the z axis is θ and the azimuthal angle around the z axis ϕ is defined with respect to the x axis. The radius in the transverse plane is $R = \sqrt{x^2 + y^2}$.

DELPHI is formed by a cylinder (barrel region) closed by two end-caps that constitute the forward regions of the detector. Figure 2.2 shows the layout of the barrel and one end-cap. The barrel covers the θ region from 40° to 140°, while the two end-caps, also referred to as the forward regions, cover $1.7^o < \theta < 40^o$; $140^o < \theta < 178.3^o$.

The measurement of the properties of the final state particles and the identification of leptons, photons and hadrons require a number of sub-detectors, with very different characteristics and goals. The DELPHI detector consists of 19 sub-detectors and a superconducting solenoid, surrounding the electromagnetic calorimeter, which gives a uniform axial magnetic field of 1.2 T . The magnetic field, B, makes the trajectories of charged particles follow a helical path with axis parallel to the beam pipe. The measurement of the radius of curvature, $\mathcal{R}$, determines the transverse momentum p_T of particles, defined as:

$$p_T = B\mathcal{R}q \tag{2.4}$$

where q is the particle charge. The electromagnetic and hadronic calorimeters measure the energy deposit of both charged and neutral particles and track the direction of showers as they develop. Finally, muon chambers identify muons which traverse the calorimeters leaving only a small energy deposit.

Since its first operation in 1989, the DELPHI detector has been upgraded several times. The original detector is described in [29] and references therein. The three major upgrades are described in [30]. A summary of its performance is reviewed in [31].

The following section will review the components of the DELPHI detector relevant to this analysis.

2.3.1 Tracking detectors

The trajectories of charged particles from collisions are determined from their ionising properties in the tracking detector active volumes through which they pass. The curvature of a particle in the magnetic field is used to determine the sign of charge and momentum.

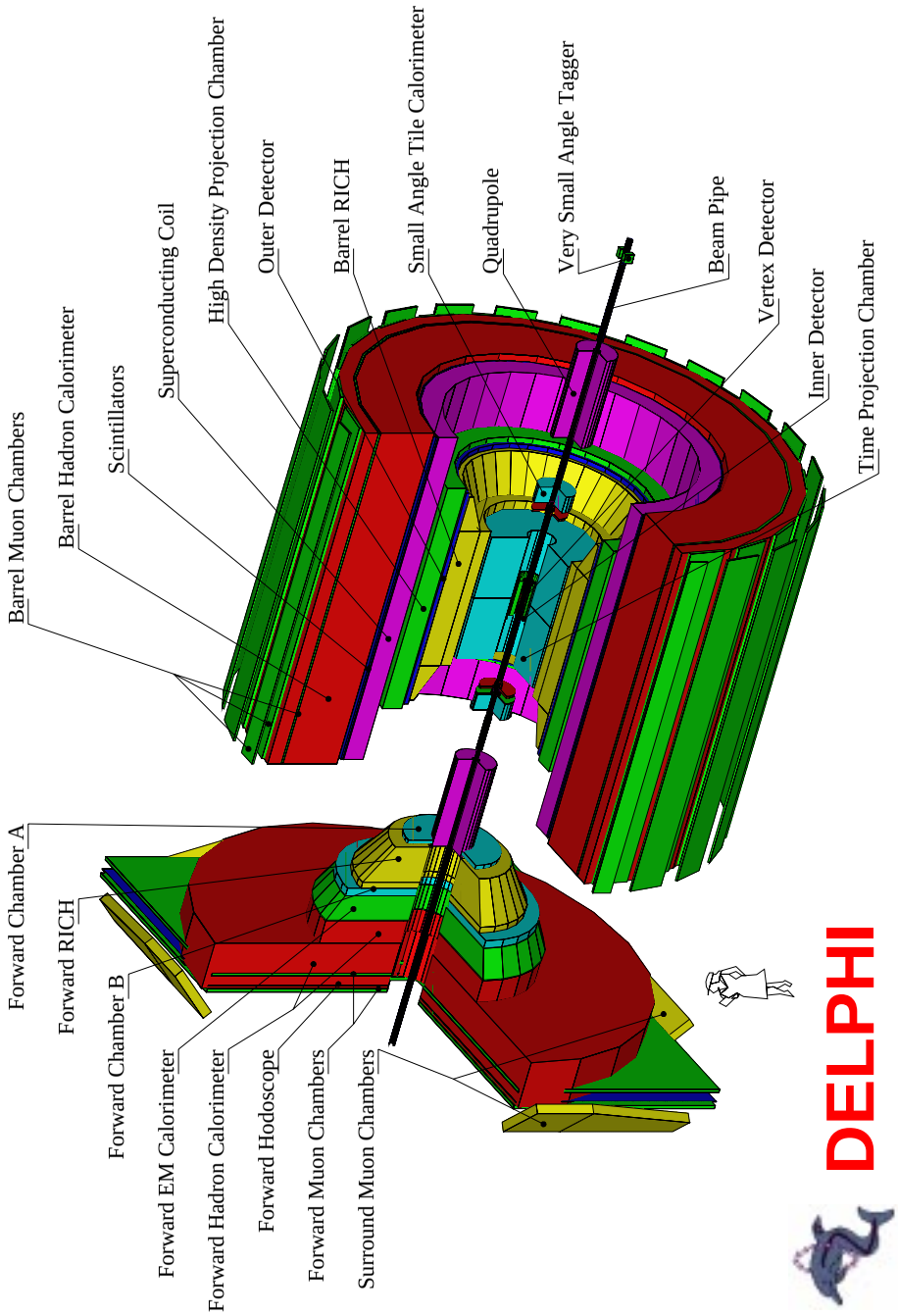

Figure 2.2: A perspective view of the DELPHI detector, showing the layout of the barrel region and of one end-cap.

The geometrical acceptance and spatial resolutions of the DELPHI tracking detectors described below are given in Table 2.1. Most charged particles have space points measured by more than one of the tracking detectors mentioned. It is therefore essential to combine tracking information from all the sub-detectors which makes the internal and global alignment important. This is achieved by using $Z^o \to \mu^+\mu^-$ events, with LEP operating at the Z^o peak.

	Position		Acceptance	Max. No. Points	Resolution
	R(cm)	$\|z\|$(cm)	θ(deg)	along track	per point (σ)(mm)
VD	6.6/9.2/10.6	$\leq$24	$\geq$21	$R\phi$: 3 z: 3	$R\phi$: 0.008 z: 0.010
VFT			11-26	4	x, y: 0.1
ID drift	11.8-22.3	$\leq$62	$\geq$10	24	$R\phi$: 0.085
ID straws	23-28	$\leq$105	$\geq$15	5	$R\phi$: 0.1
TPC	35-111	$\leq$134	$\geq$20	$R\phi, z$: 16 $R\phi$: 192	$R\phi$: 0.23 z: 0.9
OD	198-206	$\leq$232	$\geq$43	$R\phi$: 5 z: 3	$R\phi$: 0.11 z: 35
FCA	30-103	155-165	11-33	6	0.3
FCB	53-195	267-283	11-35	12	0.15

Table 2.1: Specifications and performance of the DELPHI tracking detectors. The resolution in z is given for tracks which cross the VD at 90°

Solenoid

The tracking system is enclosed within the worlds largest superconducting solenoid: it is 7.4 m long and has a radius of 2.6 m. The solenoid generates a highly uniform 1.2 Tesla field; correcting coils at the ends ensure that the field remains parallel to the z axis. The return yoke of the solenoid incorporates the hadron calorimeter (see 2.3.2).

Vertex Detector (VD) and Very Forward Tracker (VFT)

A significantly upgraded vertex detector [32] was installed during the spring of 1996 when the length of the detector was doubled to 48 cm (see Figure 2.3). The barrel

vertex detector (VD) consists of three concentric shells of silicon microstrip detectors at average radii of 6.6, 9.2 and 10.6 cm. The first and third layers consist of double sided detectors with strips both parallel and perpendicular to the z axis, thus providing both $R\phi$ and z information. The Very Forward Tracker (VFT) forms a crown of ministrips and pixel detectors capping both ends of the VD. It allows the tracking coverage to be extended down to a polar angle of 11°.

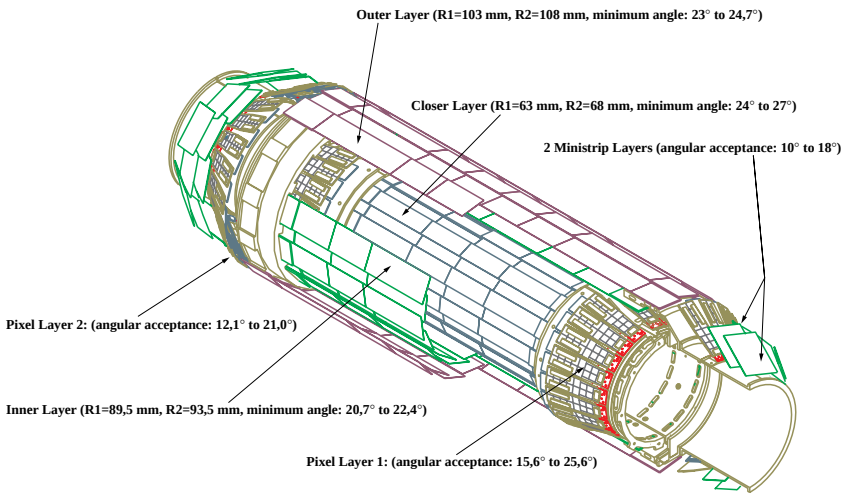

Figure 2.3: The Silicon tracker consists of three concentric cylinders of silicon strips known as vertex detector and in the forward region two layers of pixels and two of ministrips referred to as the very forward tracker.

Time Projection Chamber (TPC)

The principal tracking detector of Delphi is the Time Projection Chamber (TPC) (see Figure 2.4). The chamber is filled with Argon-Methane gas mix held at 1 atmosphere pressure. The TPC provides three dimensional spatial information, and measurements of particle $\frac{dE}{dx}$ to aid particle identification. The chamber is symmetric around the $z = 0$ plane. Each end cap is divided into 6 azimuthal sectors, each with 192 sense wires, used for $\frac{dE}{dx}$ measurement and 16 circular pad rows which enables 3 dimensional track reconstruction using 16 points per track.

A charged particle passing through the detector causes ionisation to occur in the active drift volume. The created electrons drift towards the anode in an axial electric field which is a uniform 150 Vcm^{-1} and directed towards the central plane at $z = 0$

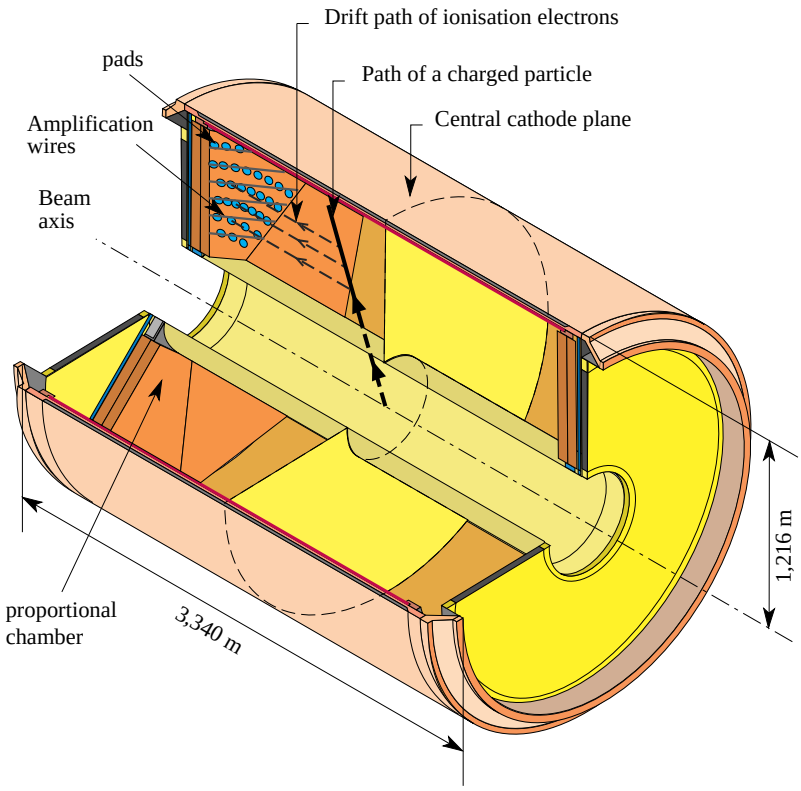

Figure 2.4: Schematic layout of the Time Projection Chamber.

in each half of the detector. The z position is calculated from the arrival time of the drifted electrons. The $R\phi$ coordinate is determined from the charge induced in the cathode pads by the avalanche around the anode.

The Inner (ID) and Outer Detector (OD)

The Inner Detector (ID) consists of two concentric sections: an inner drift chamber, surrounded by straw detectors. The drift chamber is divided in 24 azimuthal sectors, each sector having 24 anode wires. It gives a maximum of 24 $R\phi$ measurements per track. The outer part is formed by 5 concentric layers of straw tubes which perform fast ($t < 3\mu$s) $R\phi$ measurements that participate in the first level trigger. Information on the z coordinate is also available due to the small stereo angle of 2 layers.

The Outer Detector (OD), composed of five layers of drift tubes, improves the momentum resolution of high p_T charged particles. All layers provide an $R\phi$ coordinate measurement and three also provide a z measurement.

Forward Chambers (FCA and FCB)

The Forward chamber A (FCA) is mounted on both ends of the TPC. Each side consists of three modules with 2 staggered planes of drift tubes turned with respect to each other by 120° and operated in limited streamer mode. The Forward chamber B (FCB) situated at $z = \pm$ 267cm, consists of 12 sense wire planes rotated in pairs by 120° with respect to each other.

2.3.2 Calorimeters

The Delphi calorimetry system is used to measure the energy of charged and neutral particles. Electromagnetic and hadron calorimeters have the common feature that the particle is made to shower in order to fully deposit its energy. They have some basic differences due to the fact that they aim to measure the energy of distinct types of particles, which interact with matter in a very different way. The acceptance and resolutions of the DELPHI calorimeters are summarised in Table 2.2

Detector	Position		Acceptance	Depth	Shower Resolution
	r (cm)	$\|z\|$ (cm)	θ (deg)		σ_E/E (%)
HPC	208-260	$\leq$ 254	$\geq$ 43	$18X_0{}^\dagger$ ($\sim 0.6\lambda^\ddagger$)	$4.3 \oplus 32/\sqrt{E}$
FEMC	46-240	$280 - 340$	10-36.5	$20X_0(\sim 1\lambda)$	$3.0 \oplus 12/\sqrt{E} + 11/E$
HCAL barrel	65-479	< 489	$\geq$ 10	$\sim 6\lambda(\sim 57X_0)$	$21 \oplus 112/\sqrt{E}$
STIC	6.4-41	$218 - 249$	$1.7 - 10.6$	$27X_0$	$1.5 \oplus 13.5/\sqrt{E}$

Table 2.2: Specifications and performance of the DELPHI calorimeters.

Electromagnetic Calorimeters

Electromagnetic calorimeters measure the energy of electrons and photons, via cascade bremsstrahlung and pair production processes. The combined effect of these processes is the development of electromagnetic showers.

The DELPHI detector uses two different designs of electromagnetic calorimeters in the barrel and forward regions.

† A radiation length, X_0, is the mean distance over which a high energy electron loses all but $1/e$ of its energy.

‡ The interaction length, λ, in a material is defined as the mean free path of a hadron before undergoing an inelastic interaction.

High Density Projection Chamber (HPC) The barrel electromagnetic calorimeter is a sampling calorimeter which uses the time projection technique to collect the charge from electromagnetic showers. The detector consists of 144 modules with 24 segmentation in ϕ and 6 along z. It is 508 cm long and has an inner radius of 208 cm and and an outer radius of 260 cm, covering an angular region of 41.5^o to 138.5^o. Each module (see Figure 2.5) is a trapezoidal box filled with 41 layers of lead separated by gas (80%-20% Argon-Methane). The electromagnetic particles shower in the lead and ionise the gas. The lead wires provide also the electric field cage. As in the TPC, a proportional wire chamber is used to readout the drift volume. The shower arrival position gives the $R\phi$ information, while the drift time gives the z. The energy resolution $\sigma(E)/E$ for 45 GeV electrons is about 6.5% [31].

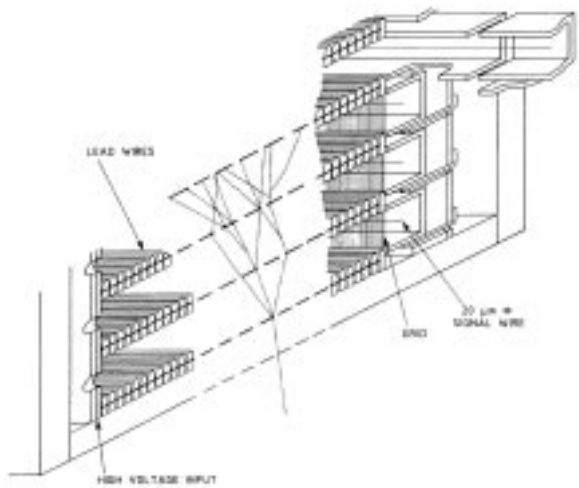

Figure 2.5: Internal structure of the HPC module, showing the development of a typical electron shower.

Forward Electromagnetic Calorimeter (FEMC)

The forward electromagnetic calorimeter, situated in each end-cap, beyond the FCB, is a lead glass calorimeter. Each end cap calorimeter consists of 4532 Čerenkov lead-glass blocks and cover polar angles between 8° and 35° from the beam pipe. The charged particles of the electromagnetic shower that develops in the blocks emit Čerenkov photons collected by vacuum photo-diodes at the end of each block. The energy resolution $\sigma(E)/E$ for 45 GeV electrons is about 4.8% [31].

Small Angle Tile Calorimeter (STIC)

The STIC (see Figure 2.6) is a sampling lead scintillator calorimeter that covers polar angles between 1.7^o and 10.6^o. As well as providing accurate luminosity mea-

surements from low angle Bhabha scattering (see Section 2.2.1) with a precision of 0.09%, the STIC can also be used, as is done in this analysis, to tag high energy, low angle, photons and electrons.

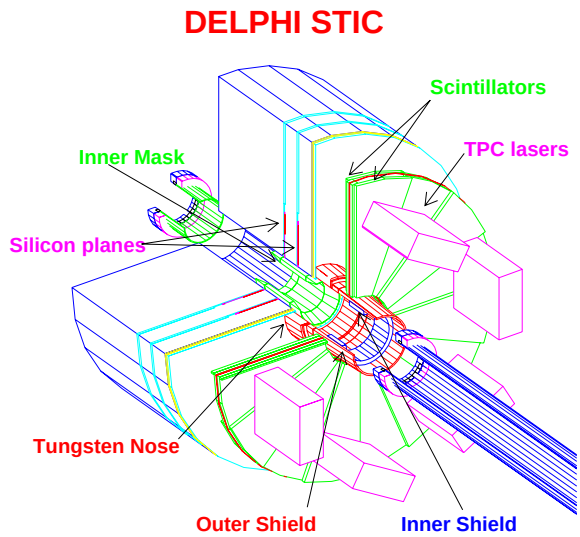

Figure 2.6: A cut away diagram of the STIC detector.

Threaded through the 47 lead-scintillator layers of the calorimeter are 1600 wavelength shifting optical fibers. These read-out fibers run perpendicular to the scintillator plates. This calorimeter geometry is known as the *Shashlik* technique: it combines a highly uniform energy resolution with good photon collection, while retaining excellent detector hermeticity. In order to separate charged and neutral particles, two layers of scintillator planes are located in front of the calorimeter. The reconstruction of the shower is aided by two layers of Silicon strips embedded in the calorimeter.

Hadronic Calorimeters (HCAL)

Hadron calorimeters rely on detecting the showers of secondary particles produced by inelastic hadronic interactions with the nucleons of a converter material. The DELPHI hadron calorimeter is incorporated into the return yoke of the superconducting solenoid and cover both the barrel and the end-caps. The barrel section is divided into 24 sectors with 20 layers, where a layer consists of a 5 cm thick plate of iron followed by a sampling detector. The end-cap regions have 19 such layers. Hadronic showers initiated in the iron are sampled by streamer tubes to produce an energy measurement.

2.3.3 Muon Chambers

The identification of muons is based on the association of hits in the DELPHI muon chambers to the extrapolation of charged particle tracks. The iron of the calorimeters absorbs most of the hadrons, though there is residual background due to fake muon signatures caused by hadrons.

The DELPHI muon detection system consists of three separate sub-detectors: the first system covers the barrel region, the second the forward region and the third covers the gap between the barrel and the end-cap regions. Table 2.3 summaries the specifications and performance of the DELPHI muon chambers.

	Position		Acceptance	Max. No. Points	Resolution
	R(cm)	$\|z\|$(cm)	θ(deg)	along track	per point (σ)(mm)
MUB	~ 445	≤ 385	52-128	2-6	$R\phi$: 1.5 z: 10
MUF	70-460	463/500	9-43	$4(x, y)$	x, y: 1 z: 10
MUS	550	487	42-53	2	10×10

Table 2.3: Specifications and performance of the DELPHI muon chambers. The resolution quoted for the MUS is given in the local coordinate system of each chamber

Barrel Muon Chambers (MUB)

The MUB consists of three layers of muon chambers modules divided in 24 azimuthal sectors. A typical sector of the barrel muon chambers is illustrated in Figure 2.7. The inner modules lie 20 cm inside the HCAL and the outer modules outside the iron. the peripheral modules are arranged behind any gaps not covered by the previous two layer of modules. Each module layer comprises a number of drift chambers arranged in two active layers. The chambers within each module are staggered in order to resolve the inherent right-left ambiguity of the drift chambers.

An electric field is produced between the central anode wire and the 13 copper cathode strips which run along the top and bottom inner surfaces of the chamber. The timing of the signal on the anode wire is used to determine the $R\phi$ hit position. One of the central cathode strips is comprised of an insulated copper winding with a signal propagation speed approximately of 0.5 cm/ns. The z-coordinate of a particle is determined by the relative timing of the signals travelling on this delay line to the

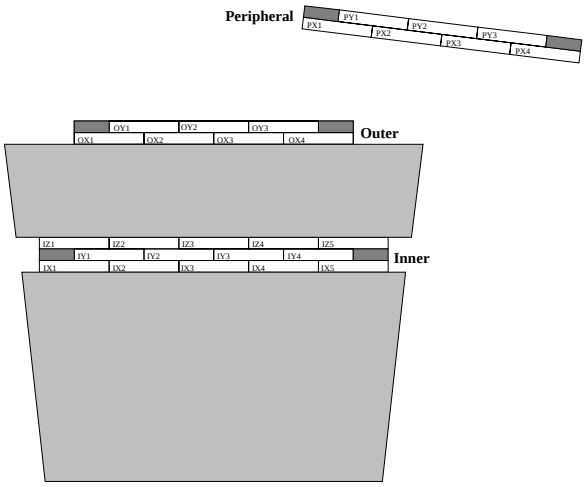

Figure 2.7: A typical sector of the DELPHI barrel muon chambers.

ends of the chamber.

Forward Muon Chambers (MUF) The forward muon detectors consist of two detection planes; the first lies at 20 cm inside the iron of the forward HCAL and the second outside. Each set of chambers is divided into quadrants consisting of two orthogonal planes of drift chambers.

Surround Muon Chamber (MUS) The surround muon chambers cover the gap between the MUB and the MUF chambers at a polar angle of around 45° and 137°. At each end of DELPHI, eight chambers are attached in pairs to the edges of the end-caps. The modules on the top and sides of the end-cap are inclined to 45° to obtain the maximum angle coverage. Each modules is comprised of two staggered layers of streamer tubes, based on those used in the HCAL.

2.4 The DELPHI Online System

The Data Acquisition System (DAS) [31] [33] reads out digitised data from the detector, storing the results for subsequent analysis. The data flow is subject to the Delphi trigger systems and proceeds according to timing signals from a central trigger control supervisor. Detector operation is monitored and controlled by the Slow Controls system.

2.4.1 Trigger

The role of the trigger system is to reduce the rate of beam cross-overs (BCO) (45 kHz) to the desired read-out and storage rate (a few Hz). The Delphi triggering algorithm is composed of four successive levels of increasing selectivity (T1,T2,T3,T4) [34]. The first two triggers are hardware triggers and operate synchronous with respect to the beam cross-over signal, while the last two are software triggers.

The first level trigger (T1) is taken at $3.5\mu s$ after the BCO and relies only on information from the fast tracking detectors (ID, OD, FCA, FCB), the scintillator arrays in the barrel (Time Of Flight, TOF [35]) and in the endcaps (Forward Hodoscope, HOF), by scintillators embedded in the HPC, by the FEMC and the MUB. T1 acts as a loose pre-trigger to get a crude impression of whether the event may be interesting or not. The trigger rate is typically 700 Hz.

In T2, the information from the TPC, HPC and MUF, and detector correlation information are now available. If the second level trigger results in a positive decision, all sub-detector systems are read out. The trigger rate is typically 5Hz.

The T3 level repeats the T2 logic using more detailed detector information. Signals from tracks, muon chamber hits, and calorimeter deposits are analysed. The decision is taken asynchronously with respect to the BCO. This trigger halves the T2 trigger rate.

T4 is based on a tailored version of the Delphi reconstruction program DELANA [36] and rejects events without tracks pointing to the interaction region or significant energy deposits in the calorimeters. This final trigger level again roughly halves the T3 trigger rate.

The trigger efficiency for various types of event topology has been studied and for the topology studied in this analysis is close to 100% [34].

2.5 The DELPHI Offline Analysis Chain

The raw data is written out by the data acquisition system. The raw data consist of the unprocessed digitized signals from each of the detectors for each triggered event. This data must be processed by the Delphi offline system to produce data suitable for direct use in physics analyses. This procedure is summarised by the flow

diagram in Figure 2.8.

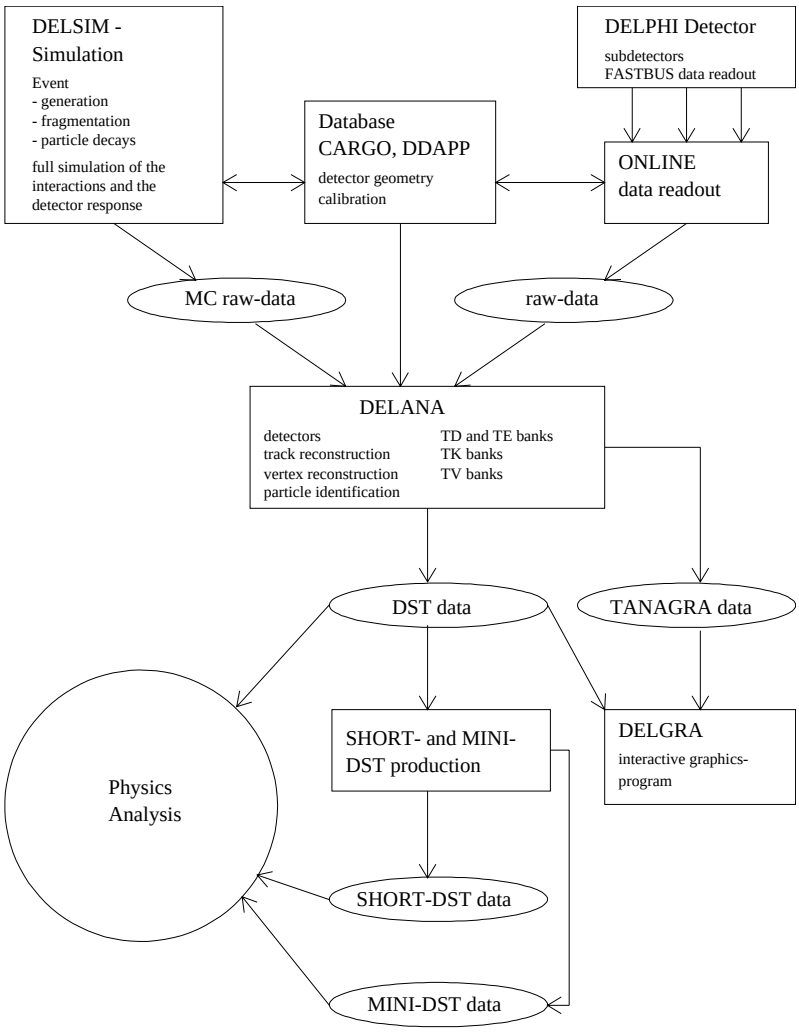

Figure 2.8: DELPHI offline analysis chain.

DELANA [36] is the main reconstruction program, converting raw data in the form of tracking hits and calorimeter deposits into charged tracks and energy clusters. DELANA reconstructs events using the detector raw data and the up-to-date information from the CARGO database.

The data output of DELANA is in the form of Data Summary Tape (DST), which contain all the information required for physics analysis. The DST ANAlysis program DSTANA is then run on DST, providing some corrections not implemented at the DELANA level. SHORT and MINI-DST are also produced at this stage, providing efficient summaries of the event information.

Chapter 3

Search for the supersymmetric scalar tau, stau ($\widetilde{\tau}$) with DELPHI at $\sqrt{s} = 189$ to 202 GeV

3.1 Introduction

During the 1998 data taking period, the LEP accelerator was operating for the first time at a centre of mass energy of 189 GeV. During the following year, the centre of mass energy was increased from 192 GeV up to 202 GeV. These increases in energy allow the extension of the search for the scalar partner of the tau (stau) which is predicted by supersymmetric models (see sections 1.3 1.4.1). This chapter reports on the search for the stau using a sequential cut analysis on the data taken by DELPHI at centre of mass energies between 189 GeV and 202 GeV and shows, for this energy range, the combined exclusion region in the right handed stau-neutralino ($\widetilde{\tau}_R$) ($\tilde{\chi}_1^0$) mass plane .

Section 3.2 describes the data samples used. Section 3.3 reviews the various background processes taken into account. Section 3.4 describes in detail the sequential cuts analysis using the data sample at 189 GeV. Section 3.5 describes the extension of the analysis to the 1999 data samples. In Section 3.6, the method used to determine the systematic errors is discussed. Finally, the results are presented in Section 3.7 and the conclusions are given in Section 3.9.

3.2 Data samples

The analysis was initially performed using the data taken in 1998 with the DELPHI detector at $\sqrt{s}$ = 189 GeV. The search was extended to the 1999 data where LEP was operating at centre of mass energies between 192 and 202 GeV. Table 3.1 summarises the integrated luminosities recorded for each centre of mass energy after requiring that the EMF, HPC and TPC efficiencies be greater than 95%.

$\sqrt{s}$ [GeV]	Luminosity [pb^{-1}]
189	154.2
192	25.1
196	75.9
200	82.7
202	40.3

Table 3.1: Integrated luminosities for each data sample after run quality checks on the EMF, HPC and TPC.

3.3 Monte Carlo samples

The signal topology expected from the decay of a stau pair is a $\tau^+\tau^-$ pair which have large acoplanarity and missing energy. The τ lepton decays mainly to one charged track (1-Prong) or three charged tracks (3-Prong). The leptonic and hadronic Branching ratios (BR) are $BR(\tau \to l\nu_l\nu_\tau) \simeq 35\%$ and $BR(\tau \to h\nu_\tau;\ h = \pi\ or\ K) \simeq$ 64% (50% 1-Prong and 14% 3-Prong decays). The standard model processes which present a similar signature are numerous. With the higher centre of mass energy that LEP attained during the LEP 2 phase, new processes such as W^+W^- pairs can be produced. Figure 3.1 shows the evolution in cross section of the SM processes as a function of the centre of mass energy.

The different generators used to simulate the SM backgrounds relevant to this analysis are discussed below as well as the generator used to simulate the stau signal.

3.3.1 SM backgrounds

Two fermion backgrounds

At LEP 2, two fermion production ($e^+e^- \to Z^0/\gamma \to f\bar{f}$) remains one of the dominant processes. At energies above the Z^0 peak, the emission of hard photons may

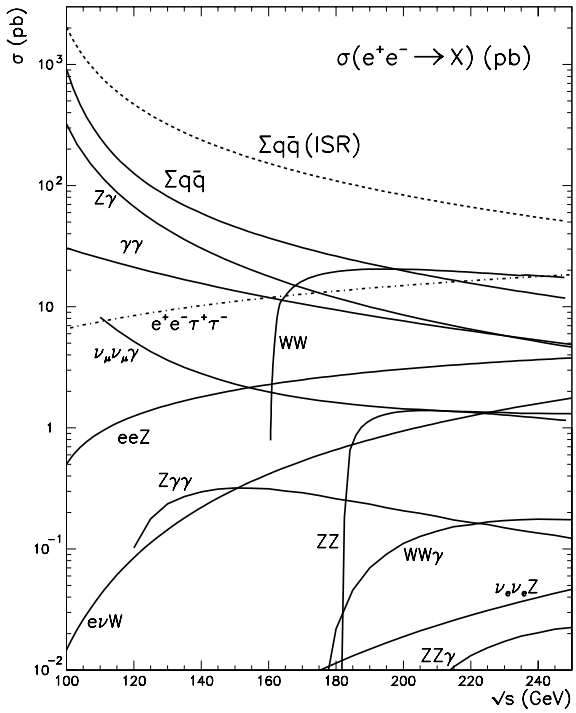

Figure 3.1: Cross sections of some typical SM processes. Some generator cuts have been applied making this diagram [37]

bring the effective energy close to the Z^0 mass, such events are referred to as "radiative return to the Z^0" ($e^+e^- \to Z^0\gamma$). The emitted photon is called the "Initial State Radiation" photon (ISR). In those events, the energy of the ISR is such that the Z^0 is real. The ISR photon is preferentially emitted at low polar angle and often lost in the beam pipe. The two fermion backgrounds $e^+e^- \to Z^0/\gamma \to \mu^+\mu^-$ and $\tau^+\tau^-$ were simulated using KORALZ 4.2 [43] while $e^+e^- \to Z^0/\gamma \to q\overline{q}$ was produced using PYTHIA [44]. The generator BHWIDE [40] was used to simulate Bhabha scattering. Those backgrounds are labeled in yellow in the plots which follow.

Two photon backgrounds

In the two photon processes ($e^+e^- \to e^+e^-X$), the system X is produced by the scattering of the two quasi-real photons, $\gamma\gamma \to X$. Two photon interactions leading to muons and taus in the final state were simulated using BDKRC [39] where the muon sample has a generator cut at $E_T > 2$ GeV. Leptonic final states with electrons were modeled using BDK [38] and TWOGAM [45] was used for hadronic final states. Those backgrounds are labeled in green in the plots.

Compton scattering and W^+W^- backgrounds

Compton scattering was generated using CMPT. W^+W^- events were generated using EXCALIBUR 1.08 [42] with $M_W = 80.35$ GeV/c^2. In addition, for the 189 GeV analysis, a second sample of W^+W^- events was generated with EXCALIBUR 1.01 where the same W mass was used. Those backgrounds are labeled in red in the plots.

Energies of the simulated MC samples

The Monte Carlo backgrounds used to analyse the data taken at 189 GeV and 192 GeV were generated at 189 GeV apart from all the $\gamma\gamma$ samples and the Bhabha sample which were generated at 184 GeV. All Monte Carlo backgrounds used to analyse the data taken at 196 GeV and 200 GeV were generated at those energies apart for $e^+e^- \to q\overline{q}$ which was generated at 184 GeV. Finally, the data taken at 202 GeV were analysed using the 200 GeV Monte Carlo samples. Table 3.2 summarises the different background generators and cross sections used.

Process		Generator	σ_{189} [pb]	σ_{196} [pb]	σ_{200} [pb]
2 fermions	e^+e^-	BHWIDE	1261†	1119	1081
	$\mu^+\mu^-$	KORALZ	8.35	7.63	7.3
	$\tau^+\tau^-$	KORALZ	8.30	7.55	7.20
	$q\overline{q}$	PYTHIA	100.0	90.4	86.1
$\gamma\gamma$	e^+e^-	BDK	2165†	2168	2185
	$\mu^+\mu^-$	BDKRC	1909†	1900	1940
	$\tau^+\tau^-$	BDKRC	436.3†	440.7	444.1
	$q\overline{q}$	TWOGAM	2307†	2307†	2307†
Comptons		CMPT	54.2	49.6	47.66
W^+W^-		EXCALIBUR1.01	17.48	N/A	N/A
		EXCALIBUR1.08	17.73	18.48	18.72

Table 3.2: Simulation Data sets

†184 GeV Monte Carlo samples used

3.3.2 Stau signal simulation

The generator SUSYGEN [46] was used to produce stau signals at $\sqrt{s} = 189$ GeV ranging from $M_{\tilde{\tau}} = 30$ GeV/c^2 to 90 GeV/c^2 in 10 GeV/c^2 steps and from 10 GeV/c^2 to $M_{\tilde{\chi}_1^0} = (M_{\tilde{\tau}} - 10)$GeV/$c^2$ in 10 GeV/c^2 steps, and used to calculate cross sections and branching ratios at all centre of mass energies. The SUSY parameters were set to:

$$\tan\beta = 1.5 \; ; \qquad \mu = -200 \text{ GeV}/c^2 \tag{3.1}$$

where $\tan\beta$ is the ratio of the vacuum expectation values of the two Higgs doublets and μ is the mixing parameter of the Higgs doublets.

Generated backgrounds and signals have been passed through the DELPHI detector simulation program (DELSIM) [41] and then processed with the same reconstruction and analysis programmes as the data samples.

3.4 Search for Staus

The characteristic signature of the production of staus is the detection of the decay products of a $\tau^+\tau^-$ pair which have large acoplanarity and missing energy. The decay products of the τ considered are $\tau \rightarrow\ e\nu_e\nu_\tau,\ \mu\nu_\mu\nu_\tau,\ h\nu_\tau,\ hn\pi^o\nu_\tau$ where the tau decays to one charged track (1-Prong), with $h = \pi\ or\ K$ and $\tau \rightarrow\ hhhn\pi^o\nu_\tau$ where the tau decays to three charged tracks (3-Prong). Both the 1-vs-1 Prong and 1-vs-3 Prongs topologies were taken in account. Due to tracking effects, these topologies sometimes appear in the detector in the 1-vs-2 Prong topology which were also included in this analysis.

Section 3.4.1 describes in detail the preselection. Section 3.4.2 describes the sequential cuts which suppress the Standard Model backgrounds while preserving any potential stau signals.

3.4.1 Preselection

This section presents distributions of the variables on which preselection cuts were applied showing the data superimposed upon the expected backgrounds, as well as the expected stau signal, for two kinematically different mass combinations: $M_{\tilde{\tau}_R} =$ 50 GeV/c^2, $M_{\tilde{\chi}_1^0} =$ 40 GeV/c^2 ; and $M_{\tilde{\tau}_R} =$ 80 GeV/c^2, $M_{\tilde{\chi}_1^0} =$ 20 GeV/c^2. At each stage of the preselection, the variables are plotted with all previous cuts applied.

The event must have between two to six "good" charged tracks of momenta greater than 1 GeV/c. A "good" charged track is defined as a track with momentum error δp less than half the beam energy and $\delta p/p < 1$ and a track length greater than 50 cm. In the case where a charged track does not fit those criteria, but has some electromagnetic or hadronic energy deposit associated with it, it is considered as a neutral. Tracks below 1 GeV/c are less trustworthy in DELPHI and in this analysis are more typical of background processes such as $\gamma\gamma$ events and beam gas events. The event is divided into two jets. The first jet is created by opening a cone of half angle 17° around the largest momentum track and assigning all charged tracks within this cone to the jet. A second jet is created around the highest momentum track of the remaining tracks. The highest momentum track in the cone is referred as the leading track. The opening angle between the two jets, referred as the jet opening angle, is required to be greater than 17°. It is required that the event has at least two jets, and in the case where there are only two tracks in the event, it

is required that they have opposite charge. The invariant mass of the leading track pair, is required to be greater than 4.5 GeV/c^2, which corresponds to generator level cuts for the $\gamma\gamma$ backgrounds.

The distribution of the track length is shown in Figure 3.2. In order to remove ID-VD tracks which are typical of bad reconstruction or conversions in DELPHI and for which the momentum estimate is poor, it is required that both of the two leading tracks have a track length greater than 100 cm.

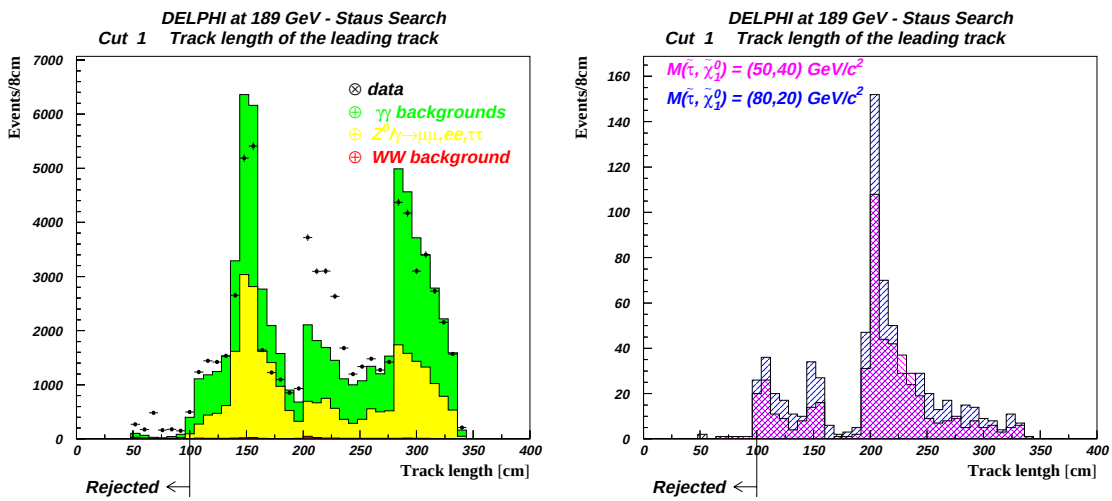

Figure 3.2: Track length of the highest momentum leading track for data superimposed on the expected backgrounds. The right plot shows the signal expectation for ($\widetilde{\tau}_R$,$\tilde{\chi}^0_1$) of (50,40) GeV/c^2 and (80,20) GeV/c^2.

NB: Some backgrounds may not be visible in a plot if their contribution are too small.

Cosmic rays are independent of the interaction point, and therefore are characterised by large impact parameters. The plots of the polar angle and the z and Rϕ impact parameters [1], as shown in Figure 3.3, show the presence of cosmic rays in the data. Events are rejected if for the two leading tracks, the Rϕ impact parameters are both greater than 0.5 cm or if the z impact parameters are both greater than 2 cm, or if the difference in z impact parameters is greater than 2 cm. The effectiveness of those cuts is shown by the good agreement which can be observed by replotting the previous variables shown in Figure 3.3 once these cuts have been applied (Figure 3.4). In particular, the theta distribution which has not been cut on, shows good agreement around $\theta = 90^o$, the region where cosmic rays would be present.

[1]Impact parameter is defined as the distance of closest approach of a particle to the centre of the beam spot envelope.

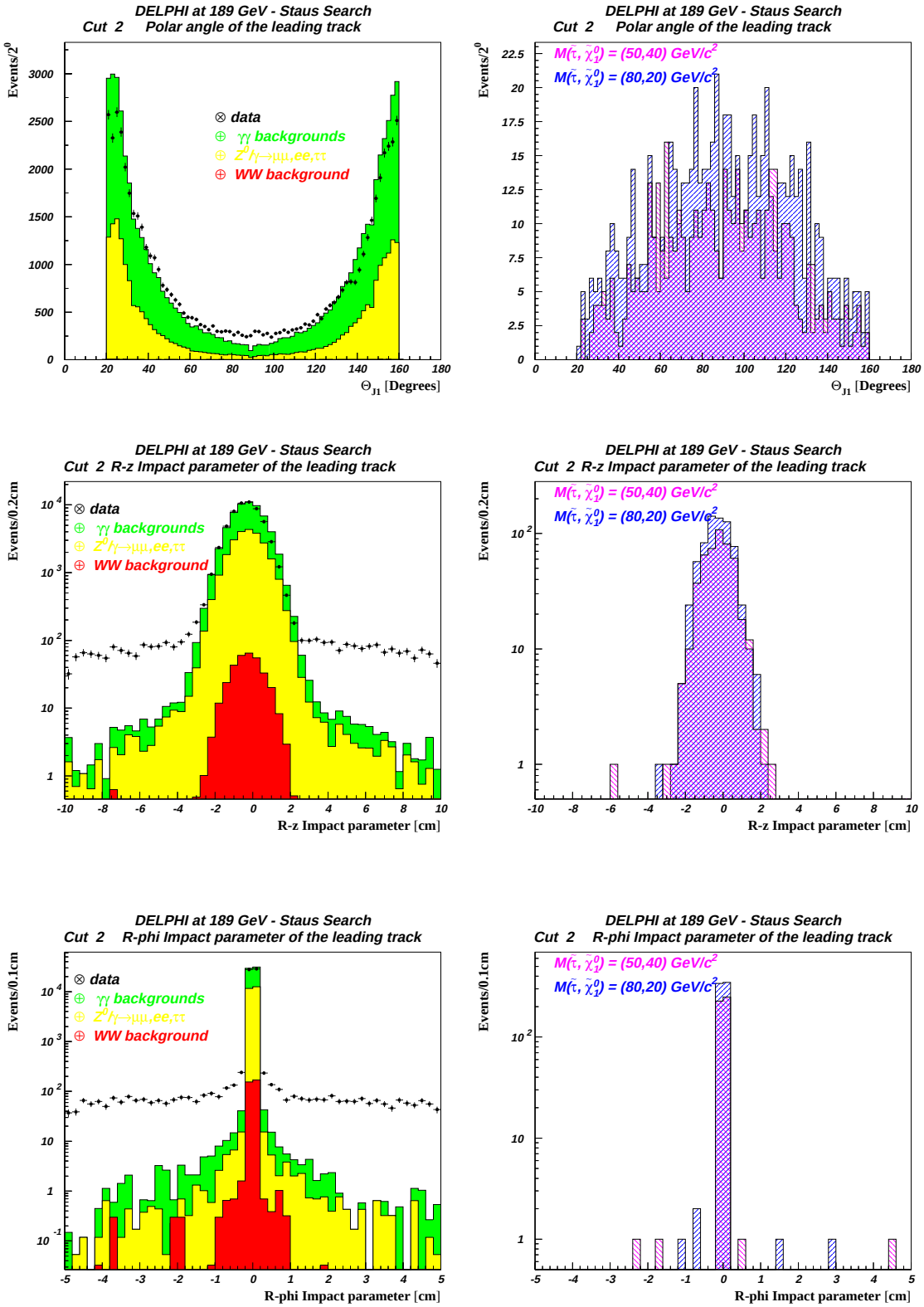

Figure 3.3: Theta distribution (top), z impact parameter (middle) and the Rϕ impact parameter (bottom) before cosmic rejection for data superimposed on the expected background (left) and ($\tilde{\tau}_R$,$\tilde{\chi}_1^0$) signal of (50,40) GeV/c^2 and (80,20) GeV/c^2 (right).

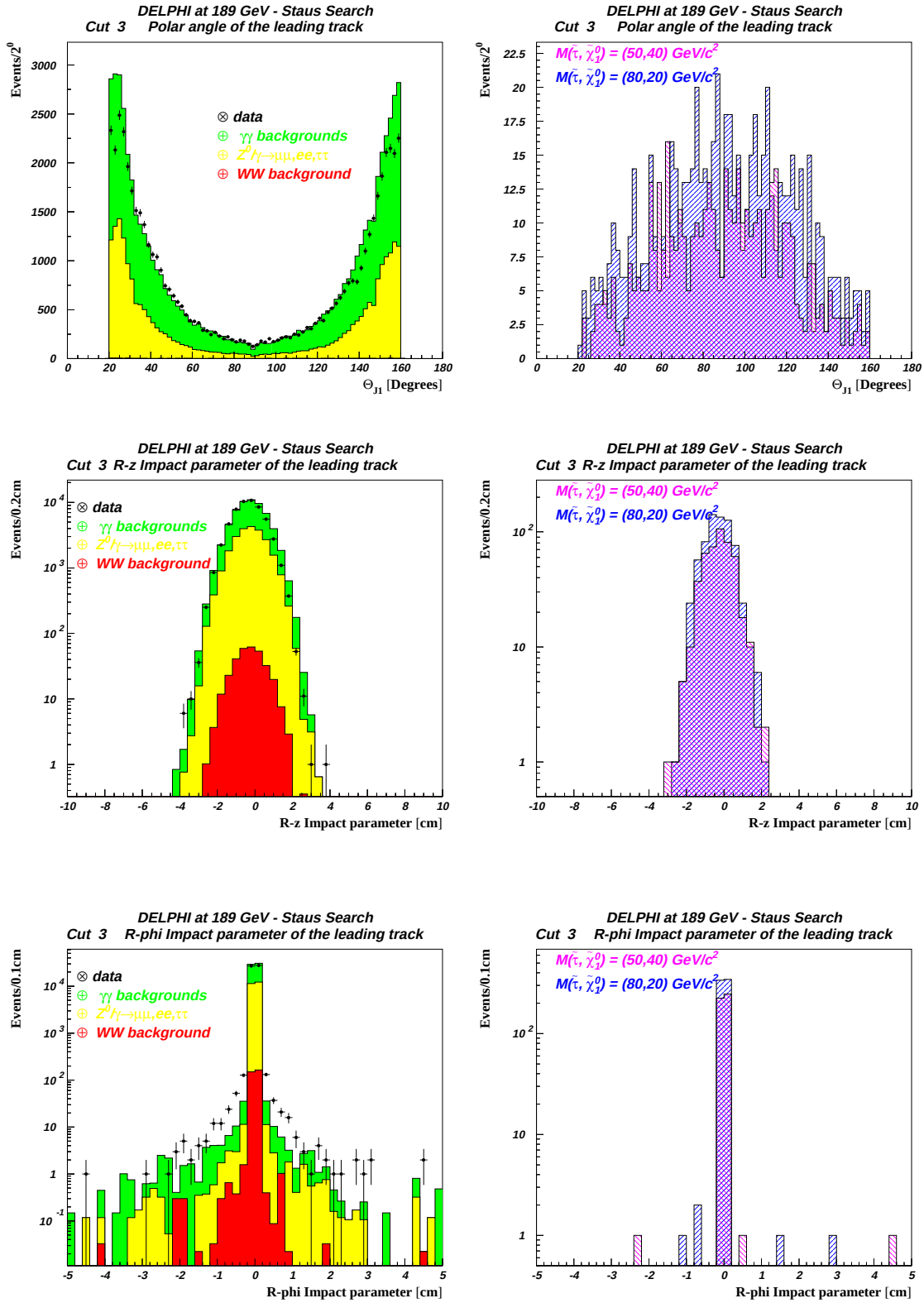

Figure 3.4: Theta distribution (top) and z impact parameter (middle) and the $R-\phi$ impact parameter (bottom) for data superimposed on the expected background (left) and $(\widetilde{\tau}_R,\widetilde{\chi}_1^0)$ signal of (50,40) GeV/c^2 and (80,20) GeV/c^2 (right) after the cosmic rejection cuts.

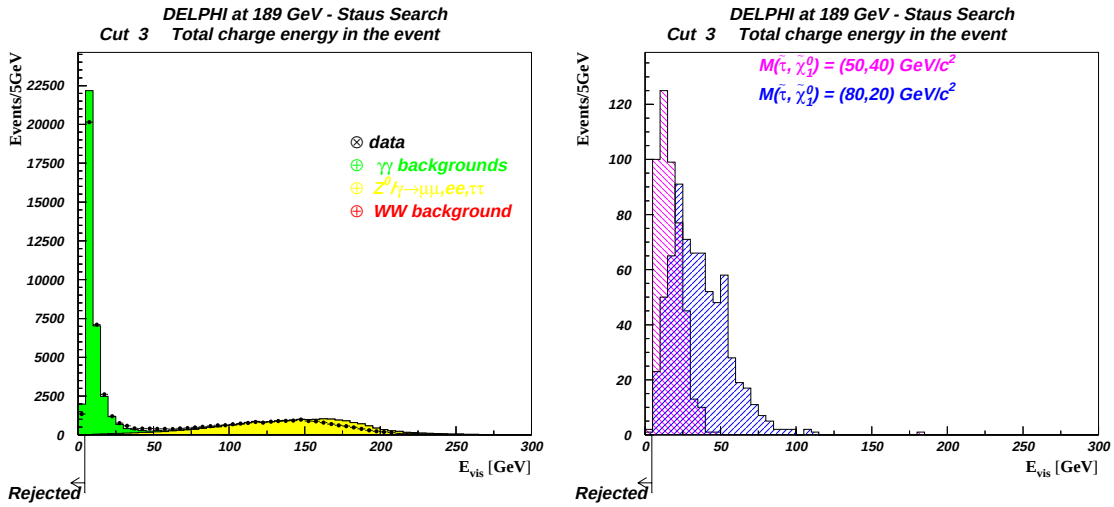

Figure 3.5: Total visible charge energy in the event for data superimposed on the expected backgrounds. The right plot shows the signal expectation for $(\widetilde{\tau}_R,\tilde{\chi}_1^0)$ of (50,40) GeV/c^2 and (80,20) GeV/c^2

The visible charged energy [2] in the event, plotted in Figure 3.5, is required to be greater than 5 GeV so that only events with a reasonable amount of energy are selected. The fact that the first bin is lower than the second one for both data and simulation is due to trigger thresholds and generator cuts.

Figure 3.6 shows the energy distribution in the FEMC detector. The peaks at half the centre of mass energy and at the centre of mass energy are due to Bhabha events where respectively one or both of the beam particles have been deflected into the FEMC. In order to reject those events while preserving the stau signals, the energy in the FEMC detector is required to be less than 50 GeV.

The $\gamma\gamma$ backgrounds are characterised by the total of the transverse momentum of the jets, $p_T^{jets} = \sqrt{\sum p_{x_j}{}^2 + \sum p_{y_j}{}^2}$, peaking towards zero (Figure 3.7) while the stau signals peak away from zero. At this stage of the preselection, events with p_T^{jets} less than 3 GeV/c are rejected. This cut removes more stau signal events in the region where the mass difference between the $\widetilde{\tau}_R$ and $\tilde{\chi}_1^0$ is small (see Table 3.3).

In order to further suppress backgrounds where a photon has been radiated, the energy of the largest isolated [3] neutral is required to be less than 20 GeV. This

[2] The visible charge energy is defined as: $E_{vis} = \sum_{i=1}^{i=Ntrack} \sqrt{p^2 + m_\pi^2}$, where m_π is the pion mass.

[3] An isolated neutral is defined as an electromagnetic energy deposit outside the cones

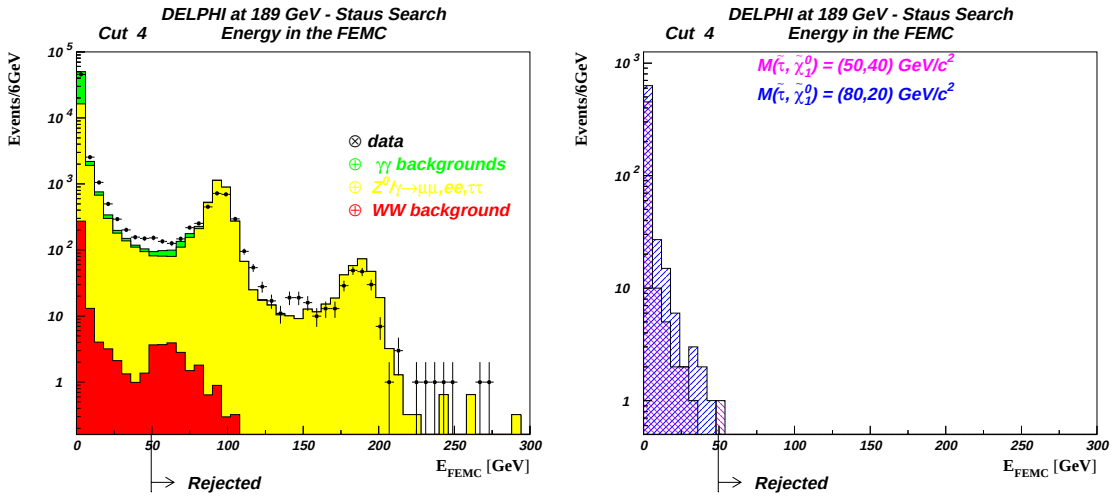

Figure 3.6: Energy in the FEMC detector for data superimposed on the expected backgrounds. The right plot shows the signal expectation for $(\widetilde{\tau}_R,\tilde{\chi}_1^0)$ of (50,40) GeV/c^2 and (80,20) GeV/c^2

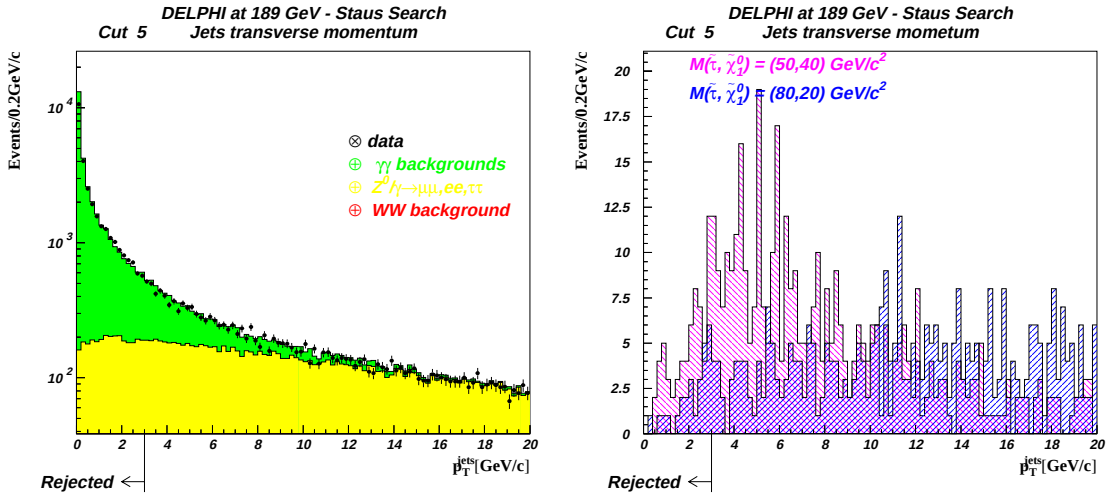

Figure 3.7: Sum of the jets transverse momenta for data superimposed on the expected backgrounds. The right plot shows the signal expectation for $(\widetilde{\tau}_R,\tilde{\chi}_1^0)$ of (50,40) GeV/c^2 and (80,20) GeV/c^2

variable is plotted in Figure 3.8; the peak at 73 GeV is indicative of "radiative return to the Z^0" events.

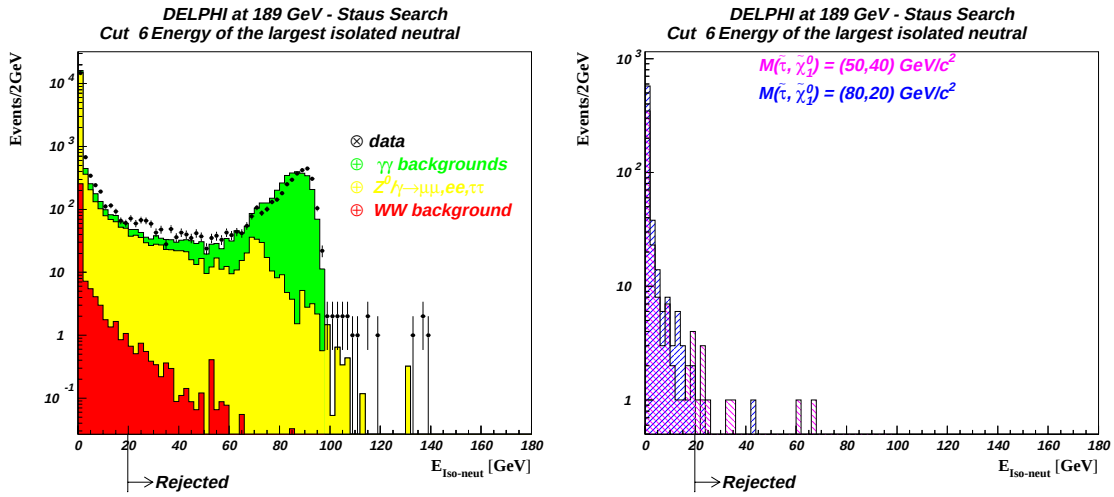

Figure 3.8: Energy of the largest isolated neutral for data superimposed on the expected backgrounds. The right plot shows the signal expectation for $(\widetilde{\tau}_R,\tilde{\chi}_1^0)$ of (50,40) GeV/c^2 and (80,20) GeV/c^2

Figure 3.9 shows the distribution of the charged tracks topology from each cone in the event for the forward and barrel regions separately. The poor agreement between the data and Monte Carlo in the forward region is due to electron interactions which are more numerous in the data, indicating an underestimate of the material budget in the Monte Carlo. Only events with the topology 1-vs-1, 1-vs-2 and 1-vs-3 are accepted in order to remove events with hadrons in the final states, which are characterised by high multiplicity. Furthermore, a cut is applied such that no charged tracks are allowed outside the cones (Figure 3.10). This removes events with tracks which have scattered in the forward region, typically Bhabha events.

In the forward region, due to the amount of material, the tracking efficiency for events with electrons in the final state is strongly influenced by the effects of scattering, interactions and bremsstrahlung. Because these effects are difficult to simulate, DELSIM is somewhat optimistic in the reconstruction of such events. This can be seen in the left plot of Figure 3.11 which shows an excess of expected background over data at small and large values of polar angle where Bhabha events dominate.

In order to correct this difference in tracking efficiency between simulation and data, the distribution of the polar angle of the two leading tracks for Bhabha, $\gamma\gamma \rightarrow e^+e^-$ and Compton scattering samples have been used to estimate a tracking

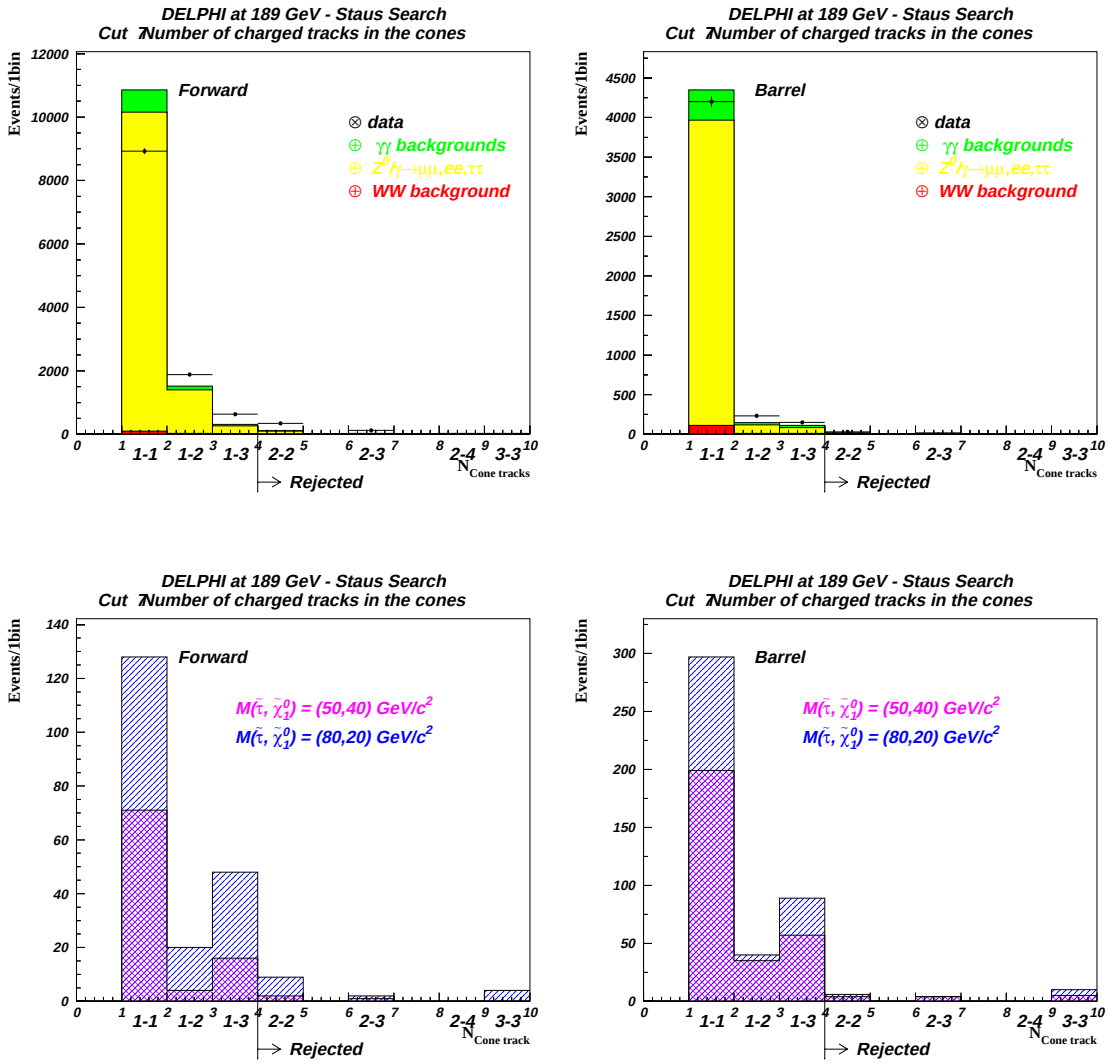

Figure 3.9: Charged tracks topology in the event for forward (left) and barrel (right). The data are plotted superimposed on the expected backgrounds. The two lower plots show the signal expectation for $(\tilde{\tau}_R,\tilde{\chi}_1^0)$ of (50,40) GeV/c^2 and (80,20) GeV/c^2

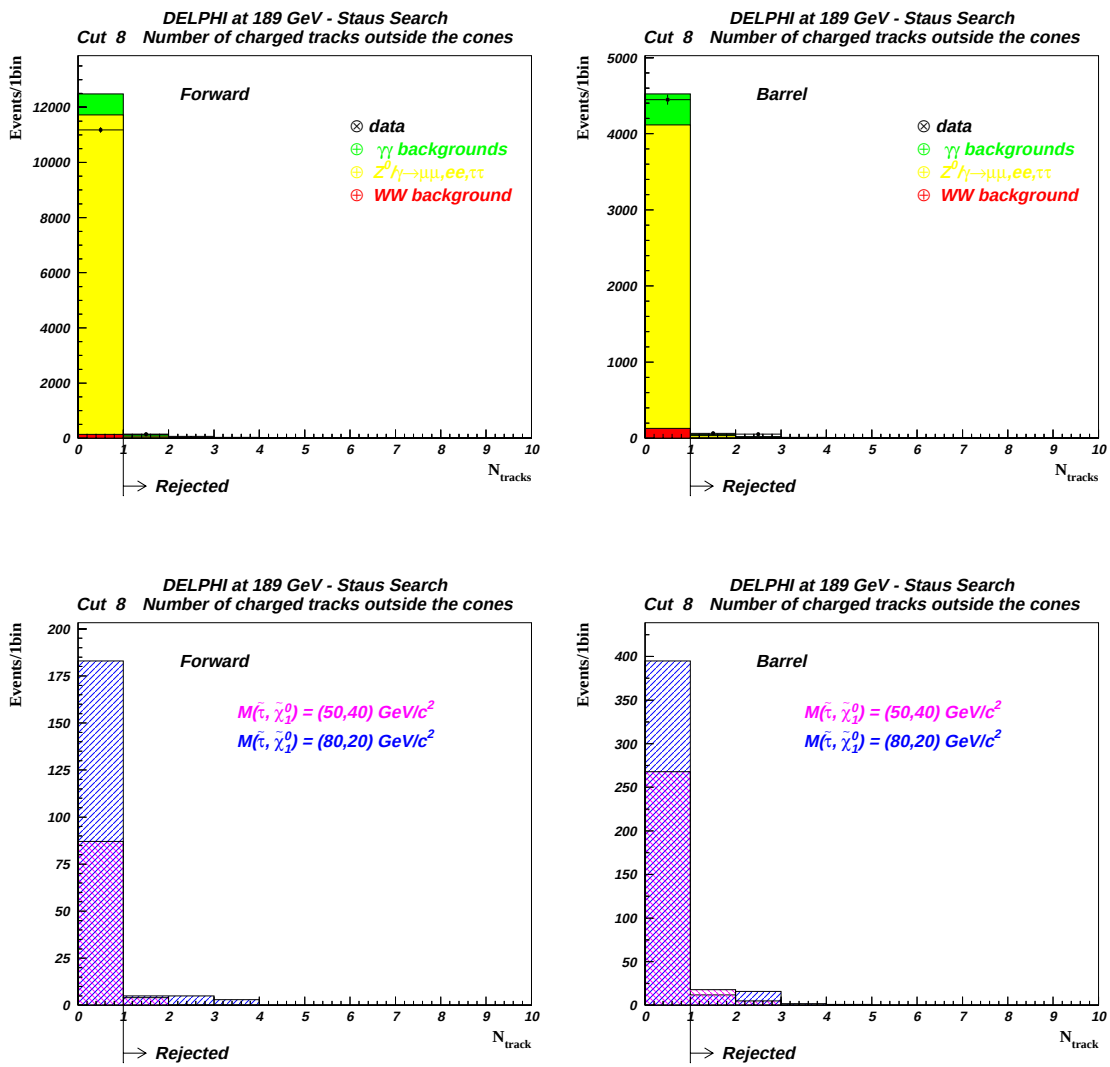

Figure 3.10: Number of charged tracks outside the cones in the event for forward (left) and barrel (right). The data are plotted superimposed on the expected backgrounds. The two lower plots show the signal expectation for $(\widetilde{\tau}_R,\tilde{\chi}_1^0)$ of (50,40) GeV/c^2 and (80,20) GeV/c^2

efficiency correction factor in the forward region. Figure 3.11 shows the polar angle distribution of the leading tracks before and after the forward tracking efficiency correction.

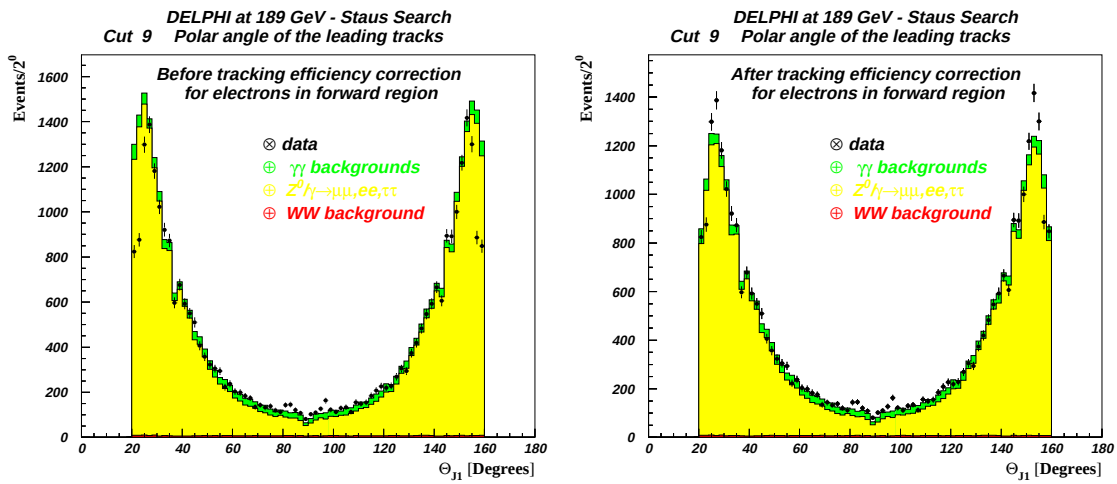

Figure 3.11: Theta distribution of the leading tracks before (left) and after (right) tracking efficiency correction in the forward region for data superimposed on the expected background.

At the end of the preselection (cut 1 to 8), 15624 data events remain for 17011 expected background. After the efficiency correction (called "cut 9") in the forward region, 15601 expected background events remain. The average stau signal efficiency, $< \epsilon_{\tilde{\tau}_R} >$, (found by averaging over all the stau samples from $(\tilde{\tau}_R, \tilde{\chi}_1^0)$ of (30,10) GeV to (90,60) GeV) is 51 %. Table 3.3 summarises the effects of the preselection cuts on the data, on the expected background, split into their different sources, and on $(\tilde{\tau}_R, \tilde{\chi}_1^0)$ signals of (50,40) GeV/c^2 and (80,20) GeV/c^2. Perfect agreement during the preselection is not expected, firstly, due to events caused by cosmic rays or beam gas which have not been simulated, and secondly, due to the material description in the forward region which prevents an accurate description of the response of DELPHI, particularly for electrons.

Cuts	2 fermions	$\gamma\gamma$	W^+W^-	Total Background	Data	$(M_{\tilde{\tau}_R}, M_{\tilde{\chi}_1^0})$ (50,40) GeV/c^2	$(M_{\tilde{\tau}_R}, M_{\tilde{\chi}_1^0})$ (80,20) GeV/c^2
1.Trklgt	24248	36349	332	60929	60169	47.9	69.2
2.Cosmic	23646	36110	318	60074	55391	47.4	68.7
3.E_{vis}	23645	34124	318	58087	54048	47.2	68.6
4.E_{FEMC}	19669	34012	299	53981	50429	47.1	68.6
5.p_T^{jets}	16826	4400	288	21514	20752	40.7	65.9
6.$Neut_{iso}$	16154	1050	283	17487	16603	39.8	65.7
7.topology	15987	1030	276	17293	16022	38.2	62.2
8.#q tracks	15839	905	268	17011	15624	35.5	57.8
9.Eff_{Trk}	14460	879	262	15601	15624	35.5	57.8

Table 3.3: Number of events in data and expected background after each of the preselection cuts. The last line give those numbers after the forward tracking efficiency correction. The last two columns give the stau efficiency for ($\tilde{\tau}_R$,$\tilde{\chi}_1^0$) of (50,40) GeV/c^2 and (80,20) GeV/c^2

3.4.2 Main Selection

This section describes the main series of sequential cuts applied after preselection to suppress the Standard Model backgrounds while keeping maximum efficiency for the stau signals. In order to motivate each cut, the variables on which cuts are applied are shown for the data superimposed upon the expected backgrounds and for the same two simulated stau signals presented in the previous section. At each stage of the sequential cut analysis, the variable in question is plotted with all previous cuts applied. In order to have an estimate of the effect of a cut on the stau signal, the average stau efficiency loss is also quoted.

A careful study of the normalisations and distributions of some variables after preselection show that the shape of the distributions for data and simulation are in good agreement, but that there are some discrepancies between the number of data and expected background events. In order to estimate those discrepancies, the background samples have been refitted to the data after preselection and weights for the Monte Carlo samples have been calculated. A detailed description of the method used is given in Section 3.6. From now on, all plots and number of expected backgrounds will be given using these refitted Monte Carlo weights. The difference between original and refitted weights provides an estimate of the systematic errors

and is also described in Section 3.6. After preselection, there were 15624 data with 15601 background events expected. Reweighting the background with the procedure described in Section 3.6, the background estimate changes to 15542 events.

Suppression of two fermion backgrounds

Due to conservation of momentum, two fermion processes favour back to back topologies in $R\phi$ and Rz. The distribution of the jet opening angle is shown in Figure 3.12. Two fermion events peak back to back while stau signals are more isotropic. By requiring that events have an jet opening angle less than 170°, 90 % of the two fermion background events are removed while the average efficiency of the stau signal is reduced by 1 %. After this cut, 2876 data events remain for 2667 expected backgrounds.

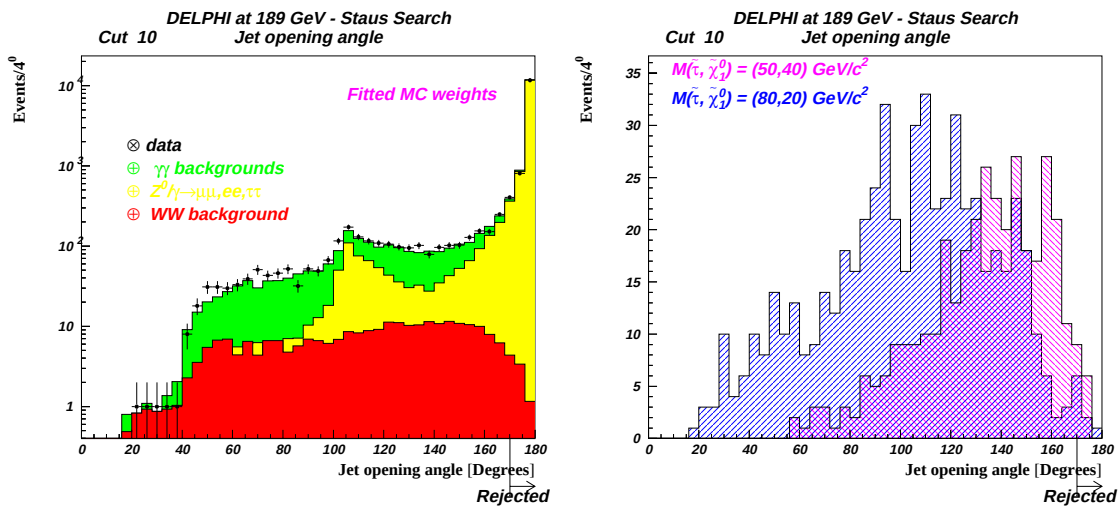

Figure 3.12: Jet opening angle for data superimposed on the expected backgrounds. The right plot shows the signal expectation for $(\tilde{\tau}_R,\tilde{\chi}_1^0)$ of (50,40) GeV/c^2 and (80,20) GeV/c^2

In a stau event, because of the missing neutralino and neutrino, the visible energy is lower than for SM background events. Figure 3.13 shows the distribution of the total visible energy in the event. Cutting on this variable allows a large amount of the remaining two fermion backgrounds to be removed. Events which have two tracks and a visible energy greater than 75 GeV are rejected. The cut is loosened to 100 GeV for 3 and 4 track events. 76 % of the two fermion background is removed while the average efficiency of the stau signal is reduced by 1.6 %. After this cut, 1520 data events remain for 1419 expected background events.

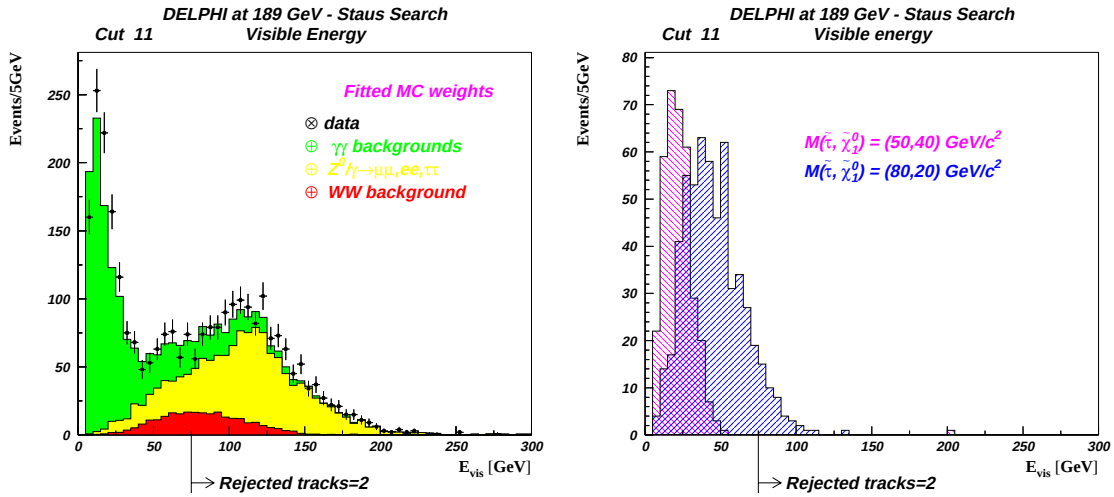

Figure 3.13: Total visible energy in the event for data superimposed on the expected backgrounds. The right plot shows the signal expectation for $(\widetilde{\tau}_R,\tilde{\chi}_1^0)$ of (50,40) GeV/c^2 and (80,20) GeV/c^2

Suppression of $\gamma\gamma$ backgrounds

This section describes the series of cuts used to reduce the $\gamma\gamma$ backgrounds. Those backgrounds are characteristically forward produced, and back to back in the $R\phi$ projection due to conservation of transverse momentum. They have generally low momentum and because they are forward produced, the transverse momentum of the two leading tracks is particularly low.

Stau signals where the stau-neutralino mass difference is small also have low transverse momentum, and therefore, those mass regions can be particularly affected by cuts that reduce $\gamma\gamma$ backgrounds.

The preselection cut on p_T^{jets} is tightened to 5 GeV/c for two track events (Figure 3.14) and to 4 GeV/c for three and four track events. This cut removes 75 % of the $\gamma\gamma$ backgrounds left over at this stage of the analysis. The average stau efficiency loss is 4.2 %, though for $(\widetilde{\tau}_R,\tilde{\chi}_1^0)$ of (50,40) GeV/c^2 it is 7.8 %. After this cut 713, data events remain for 658 expected background.

The distributions of $cos^2(\theta_{J1}) + cos^2(\theta_{J2})$; where θ_{J1} and θ_{J2} are the polar angles of the jets and their acoplanarity [4] are plotted in Figure 3.15 and illustrate the characteristics of $\gamma\gamma$ events described above and 2 fermion backgrounds. Cutting on

[4] Acoplanarity is defined as the projection of the jet opening angle in the $R\phi$ plane

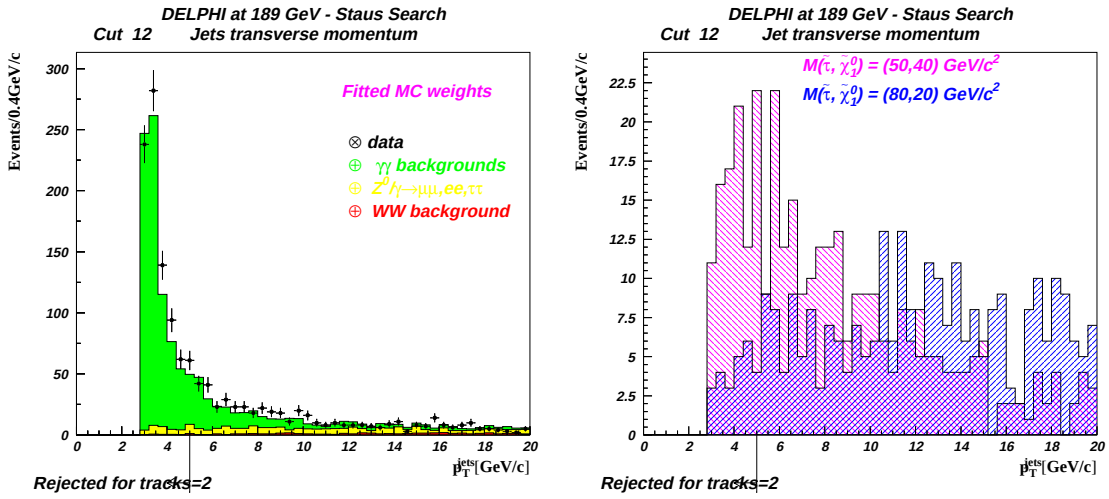

Figure 3.14: p_T^{jets} of the two leading tracks for two track events for data superimposed on the expected backgrounds. The right plot shows the signal expectation for ($\widetilde{\tau}_R$,$\tilde{\chi}_1^0$) of (50,40) GeV/c^2 and (80,20) GeV/c^2

those variables separately would however remove much of the stau signal. Therefore, a cut on the two dimensional distribution of these variables is used.

Figure 3.16 shows the two dimensional distribution for the $\gamma\gamma$ backgrounds and of the two stau signals. One can see that the backgrounds accumulate in a different region than the stau signals. The line indicated provides good separation; events above the line are rejected. In order to test the normalisation and shape of the distribution, the two variables are projected onto the indicated line to create a one dimensional variable:

$$F_1 = [cos^2(\theta_{J1}) + cos^2(\theta_{J2})] - (0.075 \ \times \ jets\ acoplanarity) + 0.15 \qquad (3.2)$$

which is plotted in Figure 3.17. Thus, events with F_1 greater than zero are rejected. This cut removes 96.5 % of the remaining two fermion backgrounds and 76 % of the remaining $\gamma\gamma$ backgrounds. The average efficiency loss for the stau signal is 3 % of the total. After this cut, 154 data events remain for 150 expected background.

A further feature of the $\gamma\gamma$ backgrounds is their low momentum. The quantity $J_{prad} = \sqrt{p_{J1}^2 + p_{J2}^2}/E_b$ is plotted in Figure 3.18, where p_{J1} and p_{J2} are the momenta of the two jets and E_b is the beam energy. Cutting directly on this variable would remove much of the stau signal, especially in the region where the mass difference between the $\widetilde{\tau}_R$ and $\tilde{\chi}_1^0$ is small. Therefore a two dimensional variable is used.

Figure 3.19 shows the distribution of J_{prad} against the previously constructed one

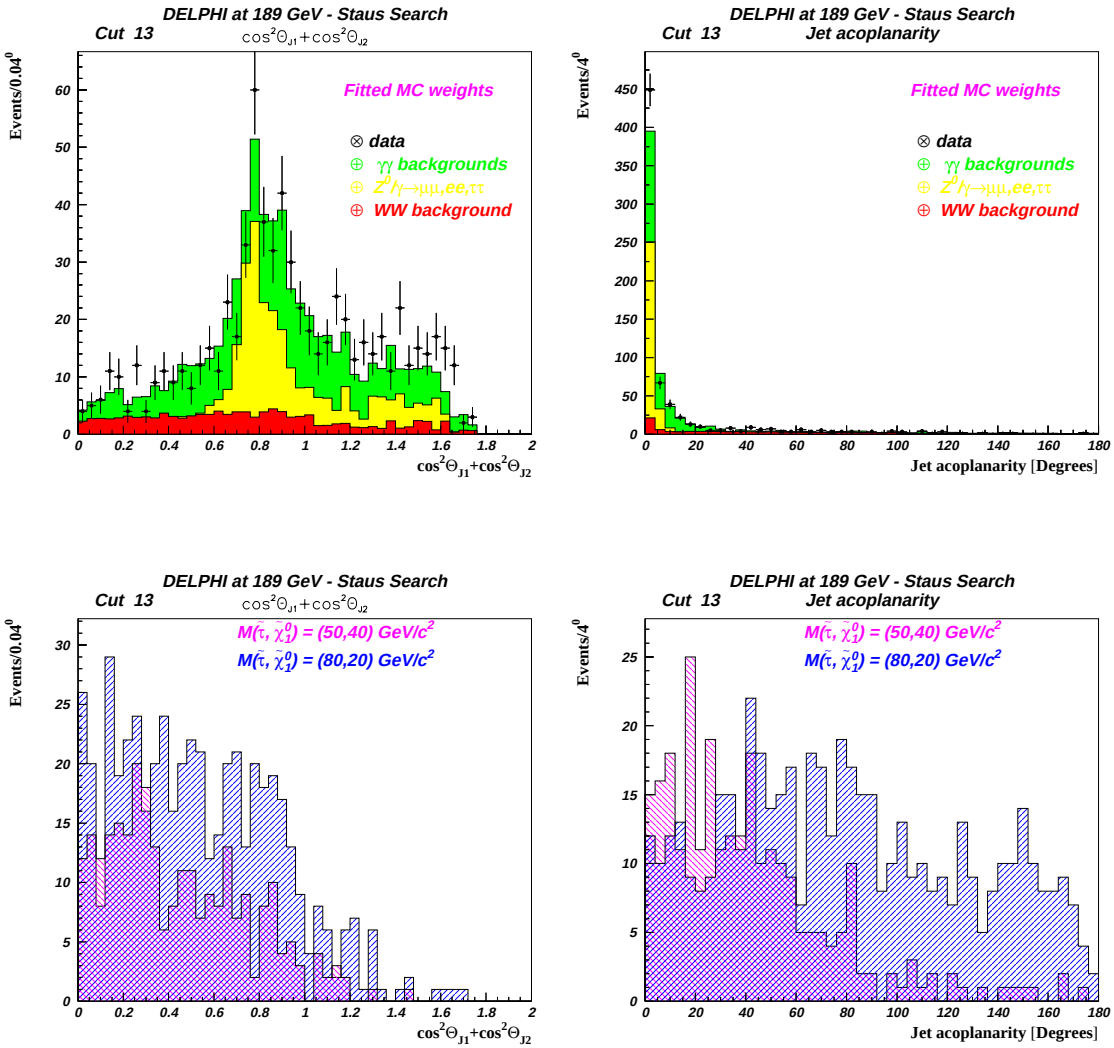

Figure 3.15: Distributions of $cos^2(\theta_{J1}) + cos^2(\theta_{J2})$ (left) and acoplanarity (right). The data are plotted superimposed on the expected backgrounds. The two lower plots show the signal expectation for $(\widetilde{\tau}_R,\tilde{\chi}_1^0)$ of (50,40) GeV/c^2 and (80,20) GeV/c^2.

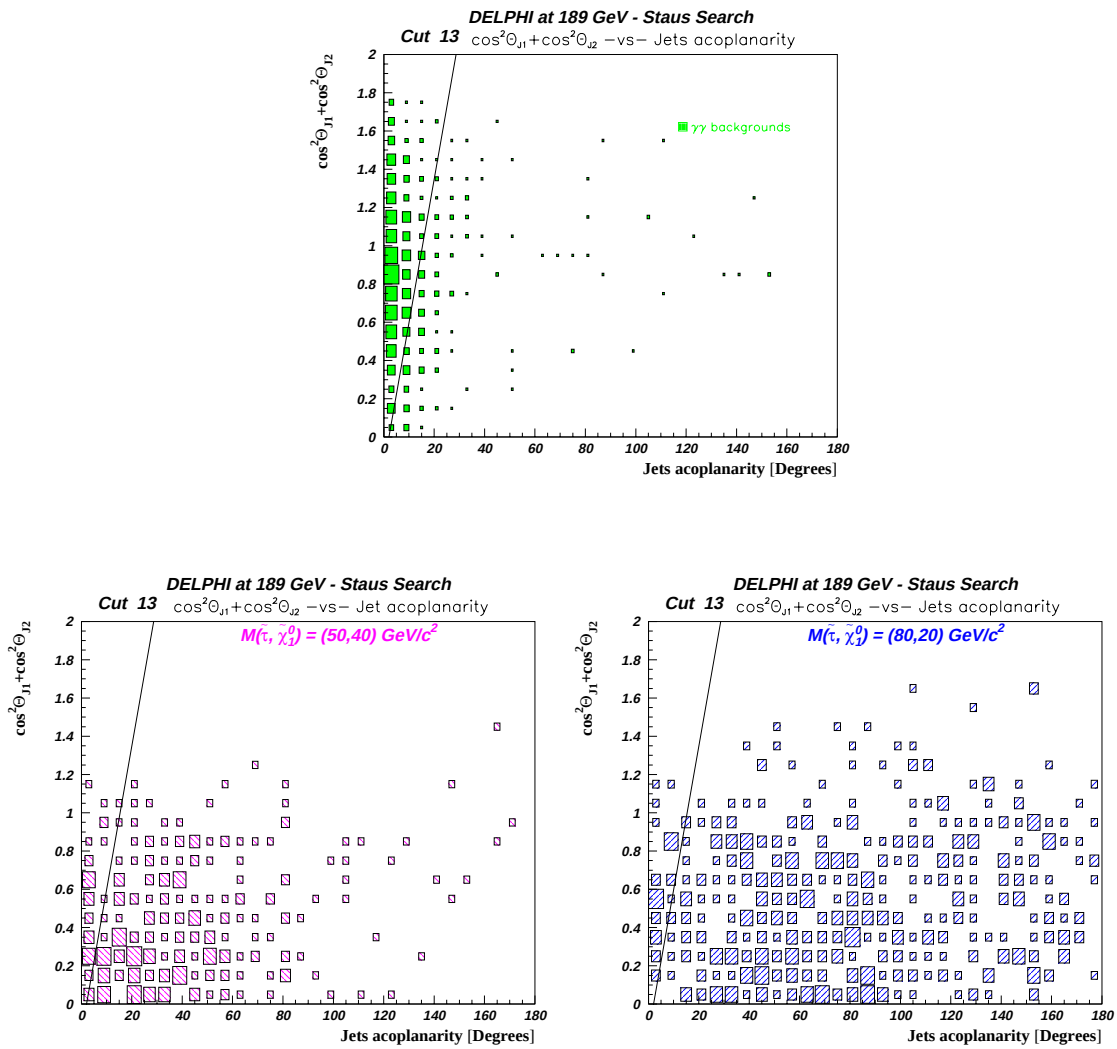

Figure 3.16: 2-dimensional plot of $cos^2(\theta_{J1}) + cos^2(\theta_{J2})$ -vs- jets acoplanarity. The upper plot shows this distribution for $\gamma\gamma$. The two lower plots show the signal expectation for $(\widetilde{\tau}_R, \tilde{\chi}_1^0)$ of (50,40) GeV/c^2 and (80,20) GeV/c^2. The two variables are projected onto the indicated line.

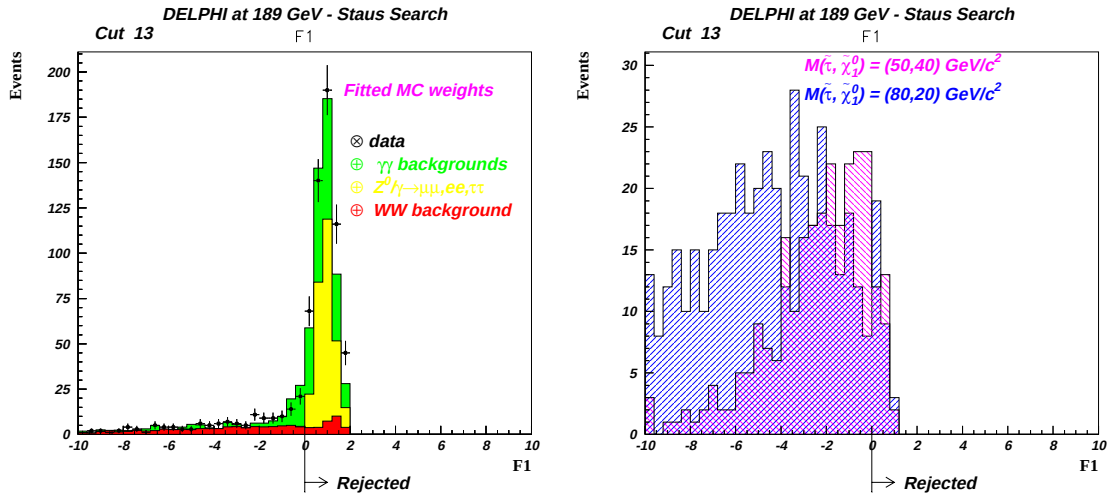

Figure 3.17: Distributions of $F_1 = [cos^2(\theta_{J1}) + cos^2(\theta_{J2})] - 0.075 \times$jets acoplanarity$+$ 0.15. The data are plotted superimposed on the expected backgrounds. The right plot shows the signal expectation for $(\widetilde{\tau}_R, \widetilde{\chi}_1^0)$ of (50,40) GeV/c^2 and (80,20) GeV/c^2

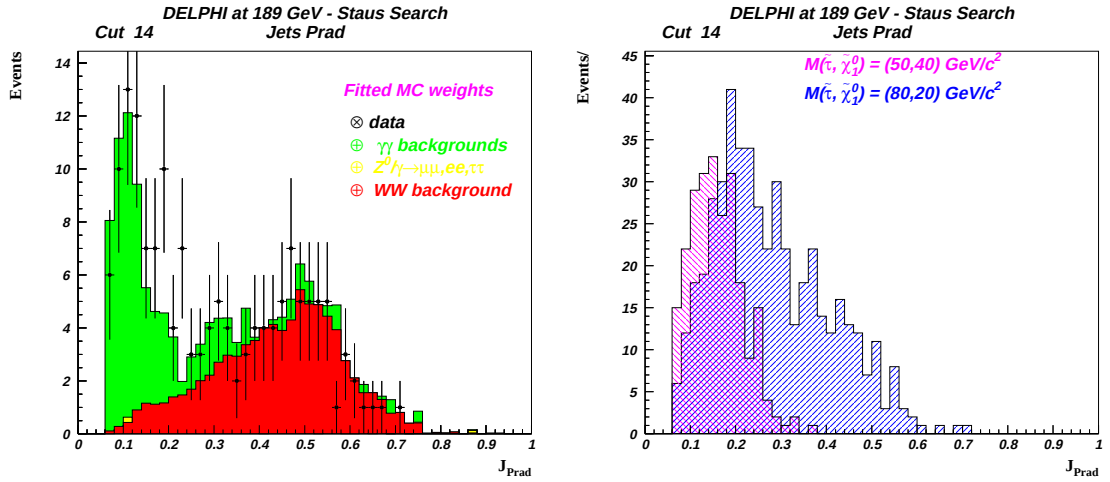

Figure 3.18: Distribution of $\sqrt{(p_{J1}^2 + p_{J2}^2)}/E_b$ for data superimposed on the expected backgrounds. The right plot show the signal expectation for $(\widetilde{\tau}_R, \widetilde{\chi}_1^0)$ of (50,40) GeV/c^2 and (80,20) GeV/c^2.

dimensional variable, F_1. Since the $\gamma\gamma$ backgrounds again inhabit a different region of space than the stau signals, the two variables can be projected onto the indicated line to create a new variable:

$$F_2 = J_{prad} - 0.075 \ \times \ F_1 - 0.2 \tag{3.3}$$

which is plotted in Figure 3.20.

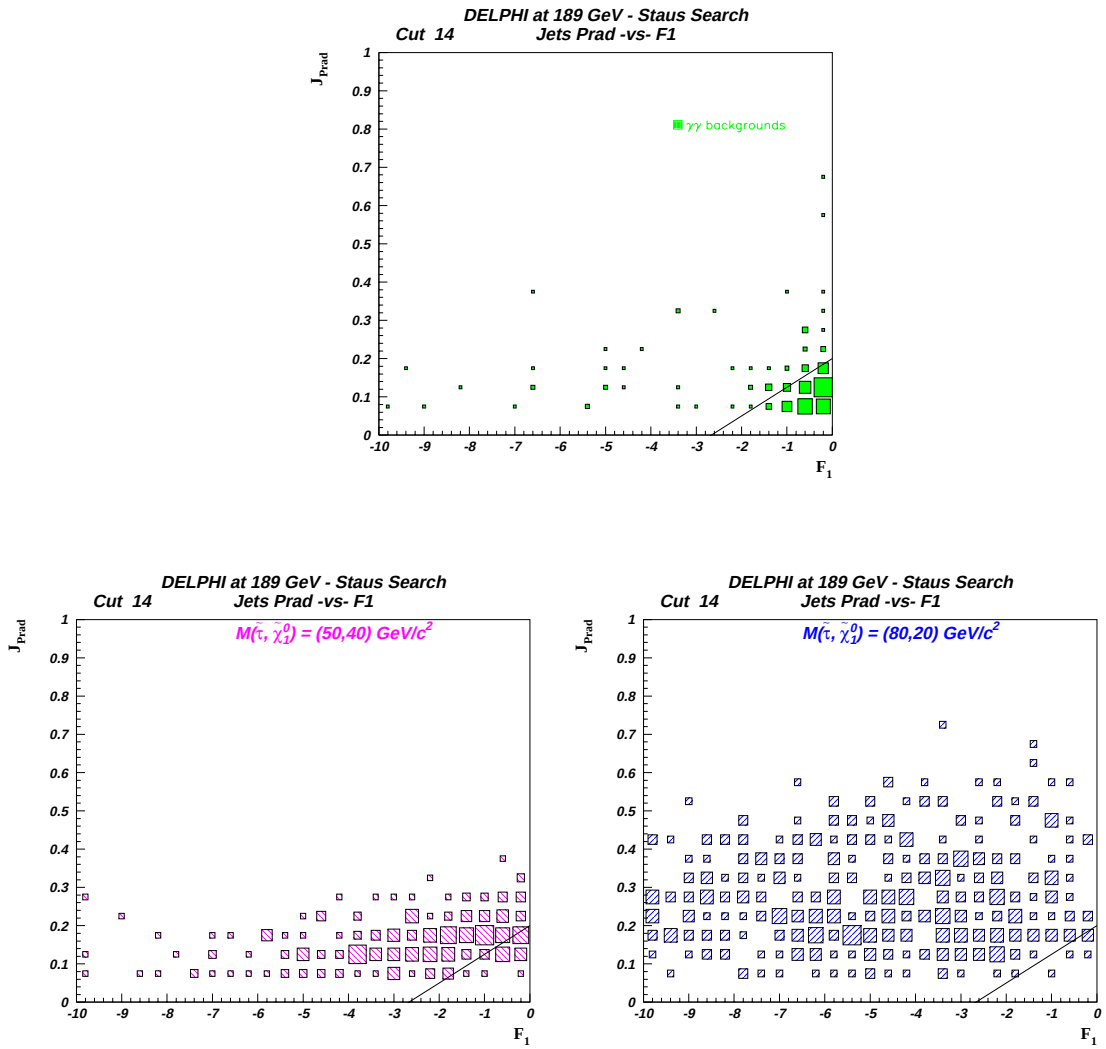

Figure 3.19: 2-dimensional plot of $J_{prad} = \sqrt{p_{J1}^2 + p_{J2}^2}/E_b$ -vs- F_1. The upper plot shows this distribution for $\gamma\gamma$. The two lower plots show the signal expectation for $(\tilde{\tau}_R,\tilde{\chi}_1^0)$ of (50,40) GeV/c^2 and (80,20) GeV/c^2. The two variables are projected onto the indicated line.

Events below the line in Figure 3.19, corresponding to $F_2 < 0$ in Figure 3.20 are rejected. This cut removes 48 % of the remaining $\gamma\gamma$ backgrounds for a loss in the average stau efficiency of 1.1 %. After this cut, 131 data events remain for 120 expected background.

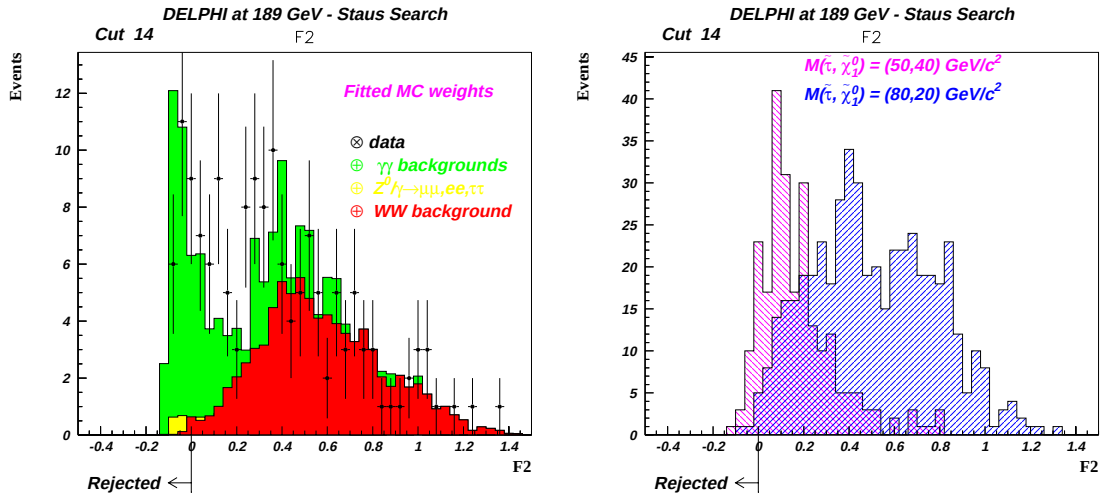

Figure 3.20: Distribution of $F_2 = J_{prad} - 0.075 \times F_1 - 0.2$. The data are plotted superimposed on the expected backgrounds. The right plot shows the signal expectation for $(\widetilde{\tau}_R,\tilde{\chi}_1^0)$ of (50,40) GeV/c^2 and (80,20) GeV/c^2.

The $\gamma\gamma$ backgrounds are also characterised by the fact that the polar angle of the missing momentum vector, θ_{miss}, points in the forward region. Figure 3.21 shows the quantity $|90^o - \theta_{miss}|$ which extends to higher values for the $\gamma\gamma$ backgrounds than for the stau signals. Events for which this quantity is less than 60° are accepted.

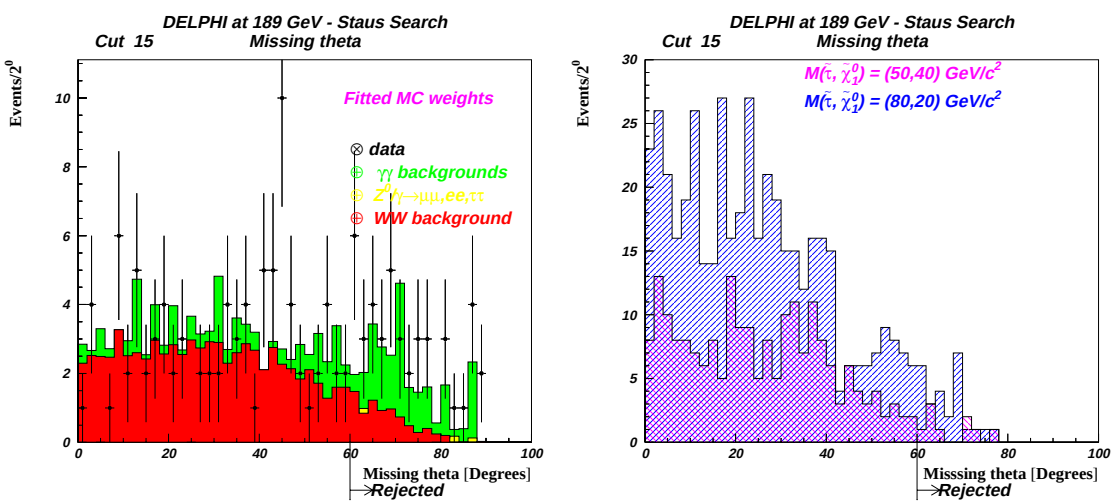

Figure 3.21: Distribution of $|90^o - \theta_{miss}|$. The data are plotted superimposed on the expected backgrounds. The right plot shows the signal expectation for $(\widetilde{\tau}_R,\tilde{\chi}_1^0)$ of (50,40) GeV/c^2 and (80,20) GeV/c^2

To remove events with radiated photon(s), a cut is applied on the energy in the STIC detector and the cut on the isolated neutral energy is tightened. Figure 3.22 plots the energy in the STIC detector which is required to be less than 2 GeV. Figure 3.23 shows the largest energy of isolated neutrals which is required to be less than 4 GeV.

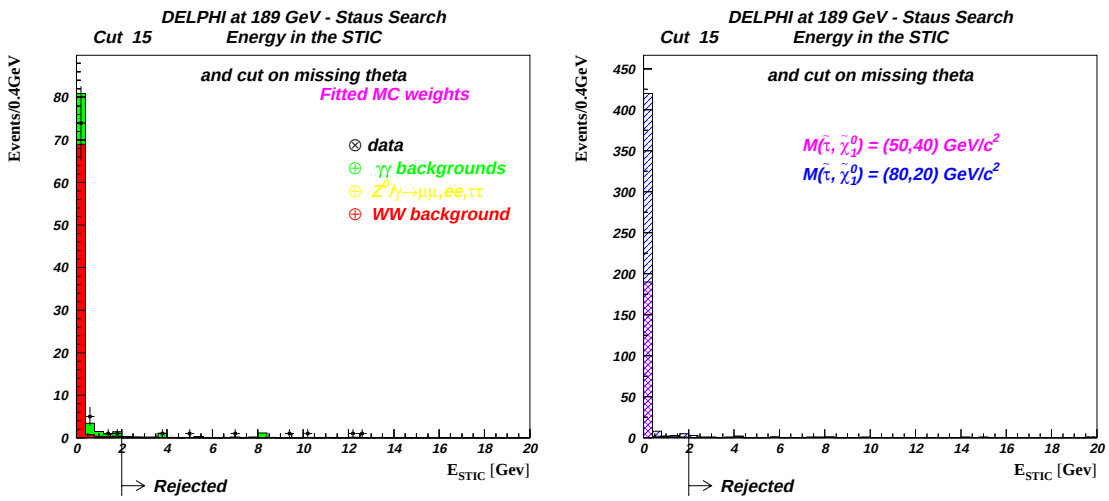

Figure 3.22: Distribution of the energy in the STIC detector.The data are plotted superimposed on the expected backgrounds. The right plot shows the signal expectation for $(\widetilde{\tau}_R,\tilde{\chi}_1^0)$ of (50,40) GeV/c^2 and (80,20) GeV/c^2

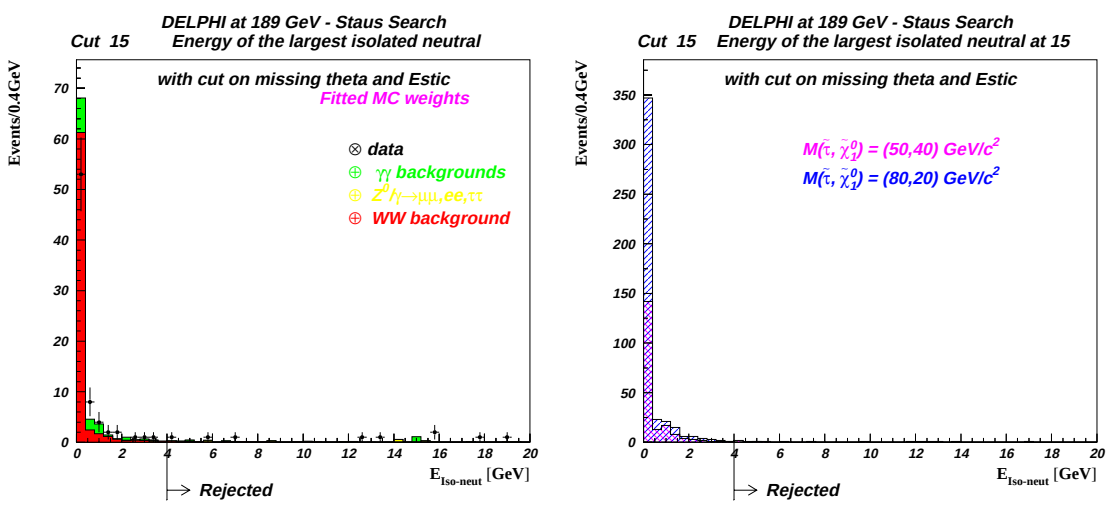

Figure 3.23: Distribution of the isolated neutral energy .The data are plotted superimposed on the expected backgrounds. The right plots show the signal expectation for $(\widetilde{\tau}_R,\tilde{\chi}_1^0)$ of (50,40) GeV/c^2 and (80,20) GeV/c^2

At this point, 72 data events remain for 81 expected background events. 70 % of the remaining $\gamma\gamma$ backgrounds have been removed while the average stau signal efficiency loss is 4.5 %.

$\gamma\gamma \rightarrow l^+l^-, (l = e, \mu, \tau)$ events can be further reduced by examining two track events which contain electrons or muons in the final states. A tighter cut placed on p_T^{jets} requiring it to be greater that 10 GeV/c removes 7.3 of the 7.6 $\gamma\gamma$ background events expected to remain in the sample (see Figure 3.24). In addition, no three track events with two identified electrons or muons are accepted (see Figure 3.25), since these are likely to originate from $\gamma\gamma$ events with an additional track from a converted photon. These cuts remove 79 % of $\gamma\gamma$ backgrounds at the expense of 1.8 % of the average staus efficiency; 71 data events remain for 72 expected background events.

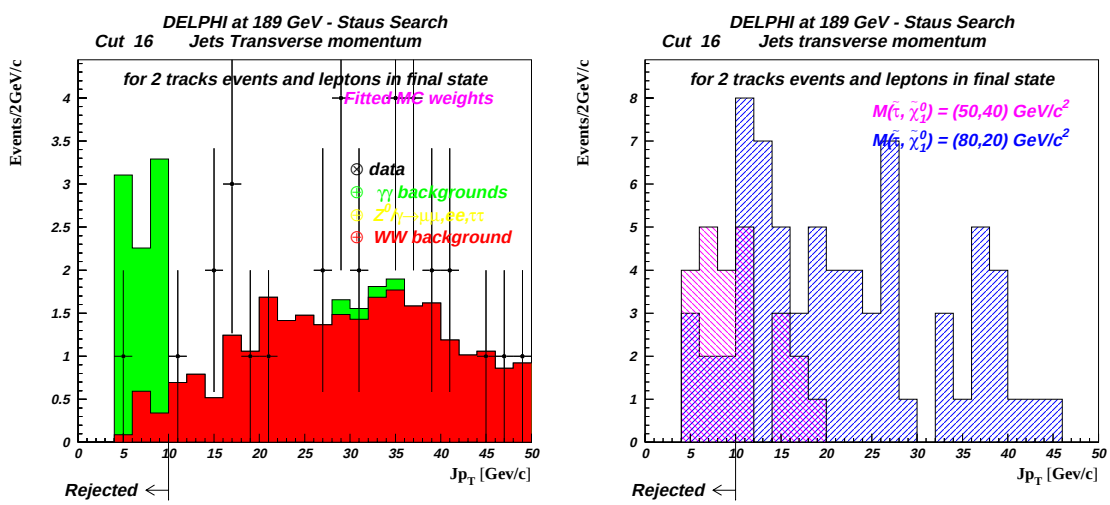

Figure 3.24: p_T^{jets} for two track events with identified leptons in the final state. The data are plotted superimposed on the expected backgrounds. The right plot shows the signal expectation for ($\tilde{\tau}_R$,$\tilde{\chi}_1^0$) of (50,40) GeV/c^2 and (80,20) GeV/c^2

Suppression of W^+W^- background

At this stage of the sequential cut analysis, the main background remaining comes from $e^+e^- \rightarrow W^+W^-$, where both W have decayed leptonically. To some extent, this background is irreducible since it has the same final state topology as a stau decay and contains missing energy due to the neutrinos.

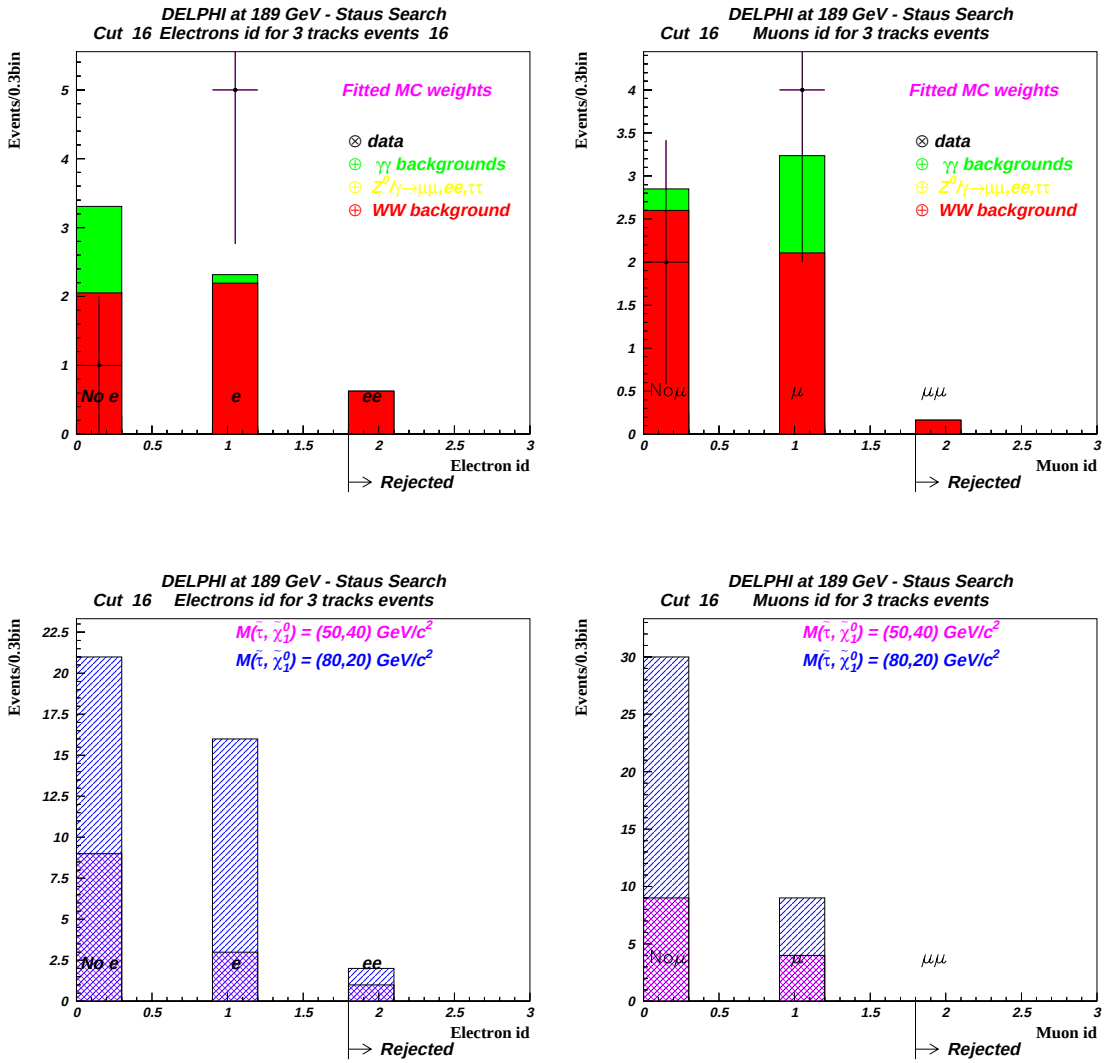

Figure 3.25: Number of electrons (left) and muons (right) for 3 track events. The data are plotted superimposed on the expected backgrounds. The two lower plots show the signal expectation for ($\widetilde{\tau}_R$,$\tilde{\chi}_1^0$) of (50,40) GeV/c^2 and (80,20) GeV/c^2.)

In the case of the fully-leptonic decay, W^+W^- decay directly to $ee, e\mu, \mu\mu$, 45% of the time and 16% of the time indirectly via a τ, while the stau decays to the same final states 12% of the time (see Figure 3.26).

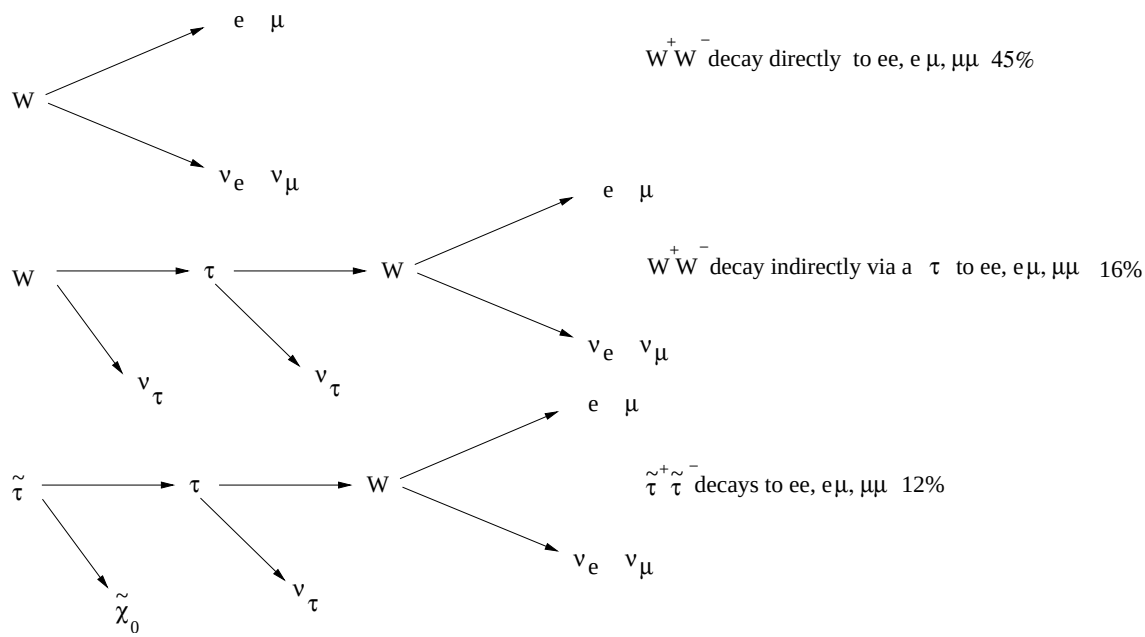

Figure 3.26: Fully leptonic decay modes of the W^+W^- and $\widetilde{\tau}^+\widetilde{\tau}^-$Stau for two track events.

In the case of the $W^+W^- \rightarrow ee, e\mu, \mu\mu$ directly, the minimum momentum possible for the lepton can be calculated to be 22 GeV/c. Figure 3.27 shows the distribution of the lower momentum track for two track events. Because of the larger missing energy in the $\widetilde{\tau}$ decay, the momentum peaks lower than for the W^+W^- events and is nearly always less than 22 GeV/c. Thus, it is required that for two track events with electrons or muons in the final state, the momentum be less than 22 GeV/c.

This cut removes 15.5% of the W^+W^- backgrounds, while the stau average efficiency is reduced by 0.2%. After this cut, 61 data events remain for 61 expected background.

To further suppress the W^+W^- backgrounds, a likelihood ratio has been considered. The four quasi-independent discriminant variables, x_i, chosen are:

- P_{J1}: total momentum of the first jet.
- P_{J2}: total momentum of the second jet.

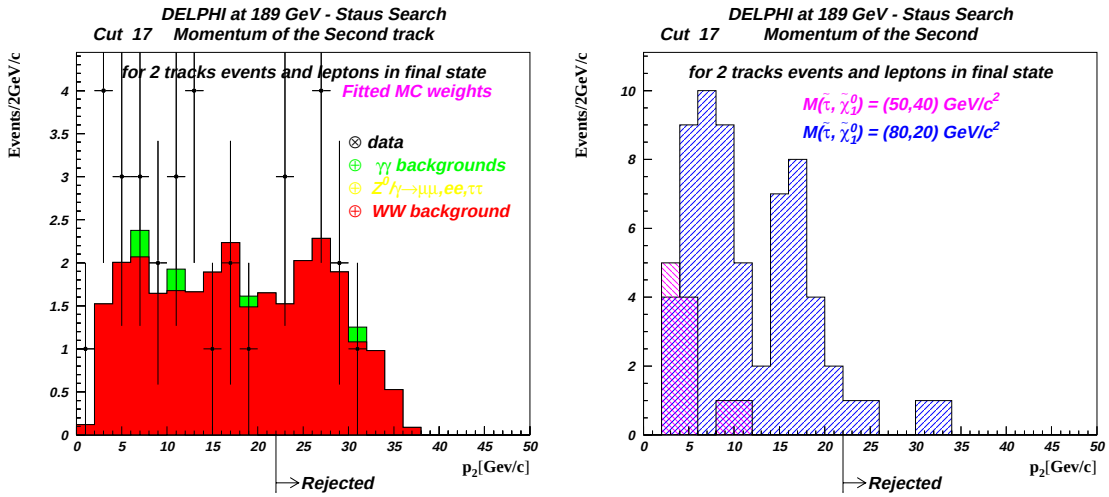

Figure 3.27: Distribution of the secondary leading track momentum for two track events. The data are plotted superimposed on the expected background. The right plot shows the signal expectation for ($\widetilde{\tau}_R$,$\tilde{\chi}_1^0$) of (50,40) GeV/c^2 and (80,20) GeV/c^2

- $\frac{1}{2}(q_{J1} \times cos(\theta_{J1}) + 1)$ where q_{J1} is the charge of the first jet [5] and θ_{J1} its polar angle.
- $\frac{1}{2}(q_{J2} \times cos(\theta_{J2}) + 1)$ where q_{J2} is the charge of the second jet and θ_{J2} its polar angle.

These quantities are plotted in Figure 3.28 for the W^+W^- Monte Carlo (red) and for the stau signals ($\widetilde{\tau}_R$,$\tilde{\chi}_1^0$) (light blue) of (70,10) and (80,10) as these are the mass combination closest to the W mass. Some discrimination can be seen in each of the plots but is insufficient to place direct cuts on those variables. The method of a likelihood ratio has been used in order to separate the W^+W^- backgrounds from the $\widetilde{\tau}$ signals.

The probability density functions, $P(x_i|y)$, for each of the four variables, x_i, have been calculated given that they originated from sample y, where y refers to the W^+W^- or stau signals. The likelihood ratio is defined as:

$$L_{ratio} = \frac{P(p_{J1}, p_{J2}, q_{J1} \times cos(\theta_{J1}), q_{J2} \times cos(\theta_{J2})|W)}{P(p_{J1}, p_{J2}, q_{J1} \times cos(\theta_{J1}), q_{J2} \times cos(\theta_{J2})|\widetilde{\tau})} \tag{3.4}$$

$$L_{ratio} \approx \frac{P(p_{J1}|W)P(p_{J2}|W)P(q_{J1} \times cos(\theta_{J1})|W)P(q_{J2} \times cos(\theta_{J2})|W)}{P(p_{J1}|\widetilde{\tau})P(p_{J2}|\widetilde{\tau})P(q_{J1} \times cos(\theta_{J1})|\widetilde{\tau})P(q_{J2} \times cos(\theta_{J2})|\widetilde{\tau})} \tag{3.5}$$

[5] As the topologies considered are 1-vs-n. where n=1,2,3; the charge of the jet which has one track is taken to be the same as the track in that jet, and the charge of the other jet is taken as the opposite.

where the approximate equality would be exact if each of the variables were independent. The logarithm of this likelihood ratio is plotted in Figure 3.29.

The optimum place for a cut on the log likelihood ratio can be found by maximising $\frac{Signal}{\sqrt{background}}$ for the simulation, which is plotted in Figure 3.30. The cut is placed at -1.5 which is indicated by the line.

This cut removes 74.2 % of the W^+W^- background left over while the average stau efficiency is reduced by 7 %, but for the worst case of ($\tilde{\tau}_R$,$\tilde{\chi}_1^0$) (70,10), 11.4 % of the efficiency is lost. After this cut, 21 data events remain for 18 expected background.

Finally, since the invariant mass of decay products of a τ is less than the τ mass, M_τ = 1.777 GeV/c^2, the invariant mass of each of the cones, taking into account the neutral particles within the cone, are required to be less than 2 GeV/c^2 (see Figure 3.31).

At the end of the sequential cut analysis, 19 data events remain for 16.92 expected background events.

3.4.3 Results summary for 189 GeV analysis

Tables 3.4 and 3.5 detail the effect of the cuts on data, simulated backgrounds and stau signals ($\tilde{\tau}_R$,$\tilde{\chi}_1^0$) of (50,40) GeV/c^2 and (80,20) GeV/c^2, as well as the average signal efficiency. Both numbers of reweighted backgrounds and numbers of original DELSIM background are provided.

The number of expected background events remaining at the end of the analysis, split into the different sources with their Monte Carlo statistical errors and an estimate of systematic errors, as described in Section 3.6, are given in Table 3.6.

Table 3.7 gives the efficiencies after the selection for each of the $\tilde{\tau}_R - \tilde{\chi}_1^0$ mass combinations. At the end of the analysis there are 19 data candidates for 16.92 $\pm$1.81 (stat.) $\pm$0.26 (sys.) expected background events.

Figure 3.32 shows an event display of a $\tilde{\tau}^+\tilde{\tau}^-$ candidate. The event shows two acoplanar tracks, one being identified as an electron with energy deposits in the electromagnetic calorimeter and the other one as a pion with energy deposits in the hadron calorimeter. The arrow indicates the direction of the missing energy.

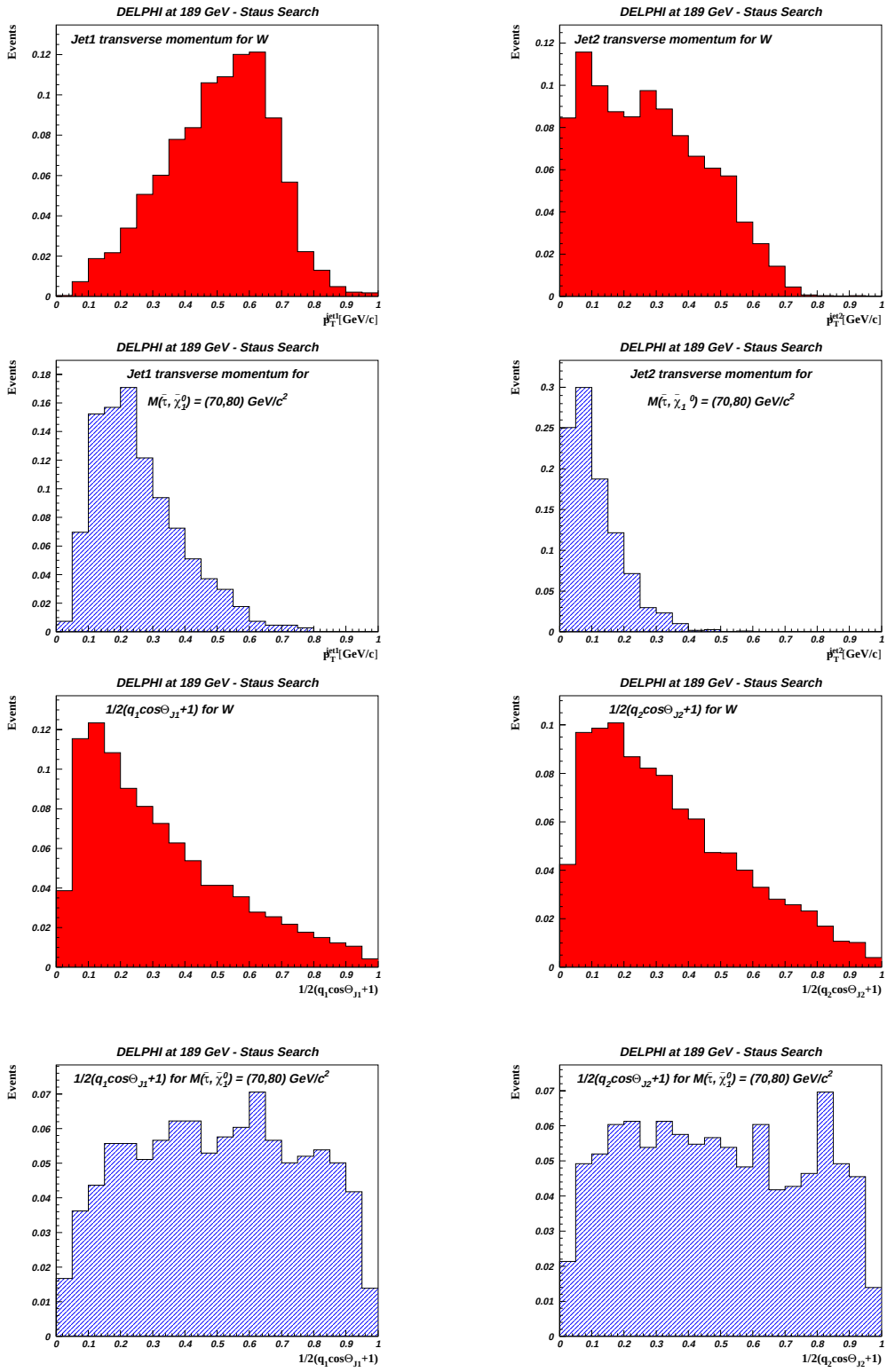

Figure 3.28: The four upper plots show the distribution of total momentum in the 1st jet (left) and 2nd jet (right) for W^+W^- Monte Carlo (1st row) and Stau (2nd row). The four lower plot show the distribution of $\frac{1}{2}(q_J \times cos(\theta_J) + 1)$ for the 1st jet (left) and 2nd jet (right) for W^+W^- Monte Carlo (3rd row) and Stau (4th row). The stau signal plots combine ($\widetilde{\tau}_R$,$\tilde{\chi}_1^0$) masses of (70,10) GeV/c^2 and (80,10) GeV/c^2.

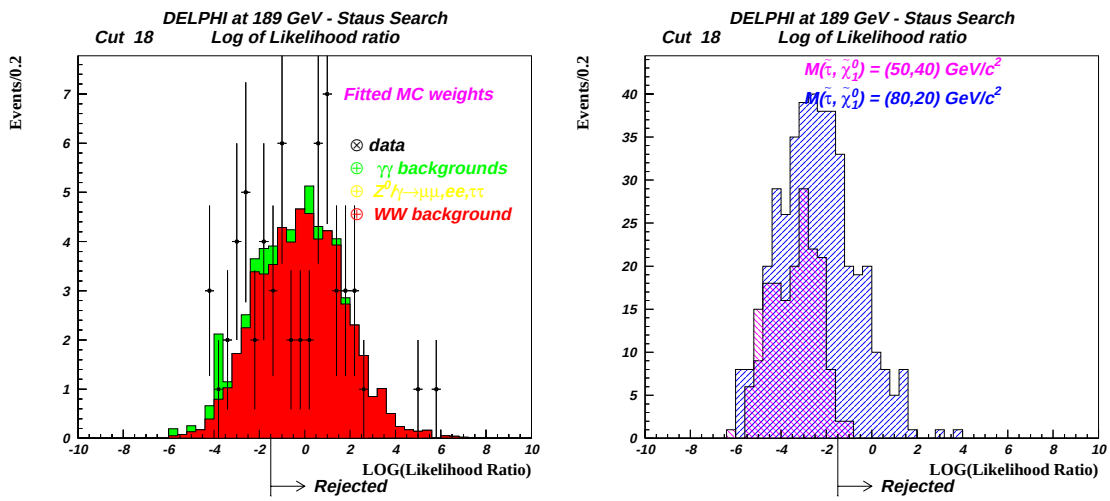

Figure 3.29: Distribution of the log(likelihood ratio) described in the text. The data are plotted superimposed on the expected background. The right plot shows the signal expectation for $(\widetilde{\tau}_R,\tilde{\chi}_1^0)$ of (50,40) GeV/c^2 and (80,20) GeV/c^2

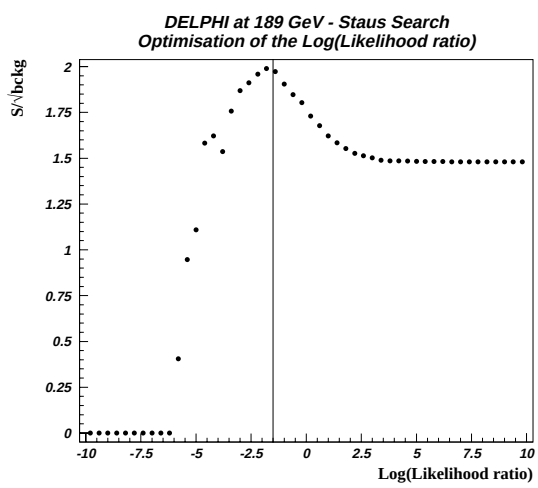

Figure 3.30: $\frac{Signal}{\sqrt{background}}$ of the log(likelihood ratio) for simulation

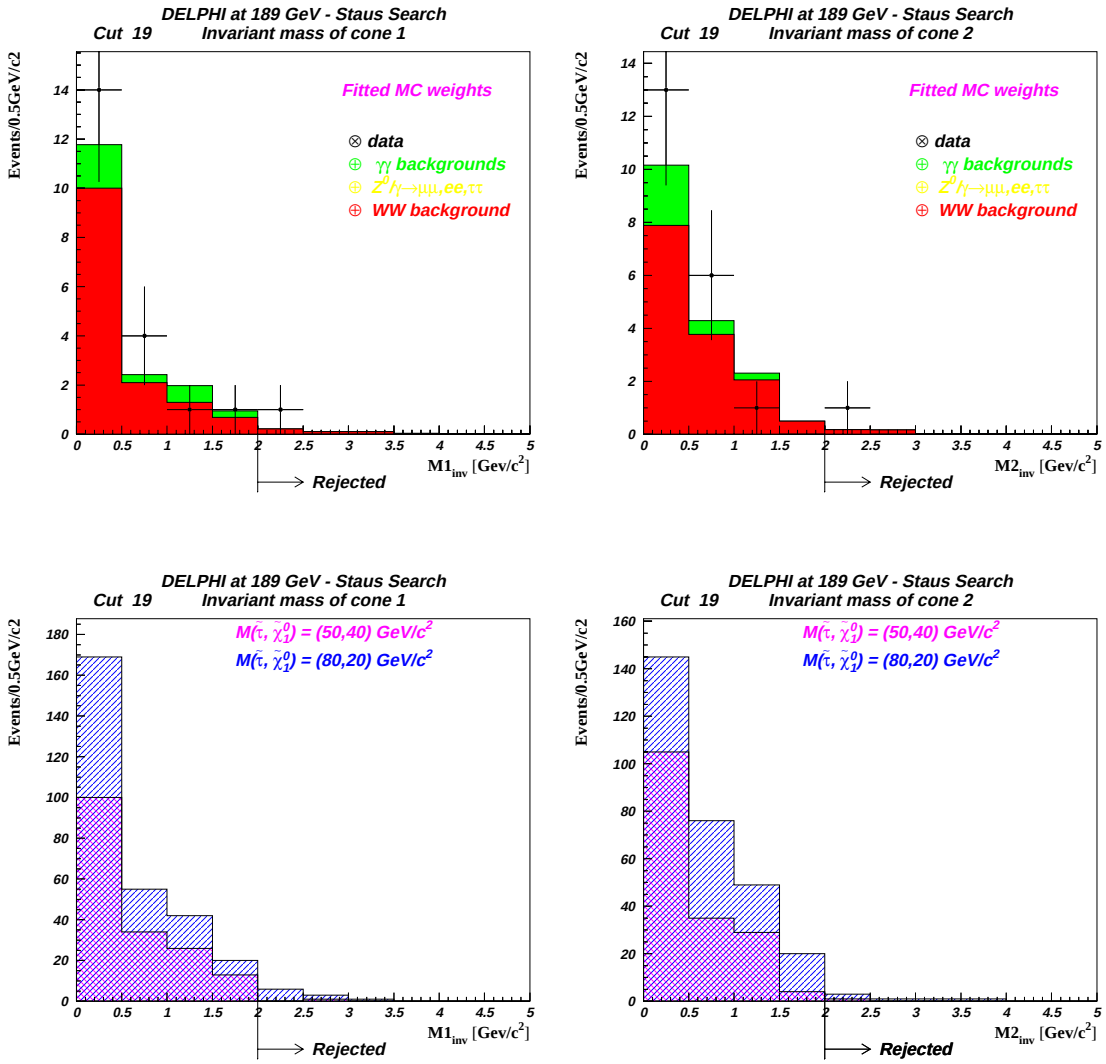

Figure 3.31: Invariant mass of each of the cones. The data are plotted superimposed on the expected backgrounds. The two lower plots show the signal expectation for $(\widetilde{\tau}_R, \widetilde{\chi}_1^0)$ of (50,40) GeV/c^2 (middle) and (80,20) GeV/c^2 (bottom)

Selection	Data	Total background	2 fermions bckg	$\gamma\gamma$ bckg	WW & Compton
9. Preselection	15624	15542.0 (15601.0)	14208.6 (14460.1)	1071.8 (879.3)	261.6 (261.6)
10. Jet opening angle	2876	2667.1 (2453.1)	1388.5 (1359.1)	1023.5 (838.8)	255.1 (255.1)
11. E_{vis}	1520	1419.4 (1239.2)	331.6 (325.7)	974.5 (800.3)	113.2 (113.2)
12. p_T^{jets}	713	658.0 (606.5)	302.5 (297.4)	244.9 (198.4)	110.6 (110.6)
13. F_1	154	150.1 (141.2)	10.6 (10.1)	58.3 (49.9)	81.2 (81.2)
14. F_2	131	120.3 (114.4)	9.2 (8.8)	30.5 (24.9)	80.7 (80.7)
15. θ_m, & IsoNeut	72	81.2 (79.7)	3.3 (3.1)	9.3 (8.0)	68.7 (68.7)
16. Leptons	71	71.8 (71.3)	3.0 (2.8)	1.9 (1.7)	66.9 (66.9)
17. P_{min}	61	61.3 (60.9)	2.8 (2.7)	1.9 (1.7)	56.5 (56.5)
18. $Log(L_R)$	21	17.6 (17.3)	1.1 (1.1)	1.9 (1.7)	14.6 (14.6)
19. M_{Inv}	19	16.9 (16.5)	1.1 (1.1)	1.9 (1.7)	13.9 (13.8)

Table 3.4: Effect of the sequential cuts on the data and simulated backgrounds using both the refitted weights and the original weights (in brackets). The difference between these two numbers is an indication of the systematic uncertainty in the selection.

Selection	$M_{\tilde{\tau}_R}, M_{\tilde{\chi}_1^0}$		$< \epsilon_{\tilde{\tau}_R} >$
	50-40	80-20	
Preselection	35.5	57.8	51.0
Jet opening angle	34.5	56.9	49.9
E_{vis}	34.4	53.2	48.2
p_T^{jets}	26.6	51.1	44.1
F_1	23.9	48.1	41.1
F_2	21.3	47.7	39.9
θ_{mis}&E_{STIC}	19.2	42.8	35.4
Leptons	17.8	41.9	33.7
P_{min}	17.8	41.6	33.5
$Log(L_R)$	17.4	29.6	26.4
M_{Inv}	17.2	28.0	24.8

Table 3.5: Effect of the sequential cuts on the stau signals ($\tilde{\tau}_R$,$\tilde{\chi}_1^0$) of (50,40) GeV/c^2 and (80,20) GeV/c^2. The average stau efficiency is given in the last column.

Backgrounds		Events	σ_{stat}	σ_{sys}
2f	e^+e^-	0.0	0.31	-
	$\mu^+\mu^-$	0.0	0.14	-
	$\tau^+\tau^-$	1.13	0.38	0.15
	$q\overline{q}$	0.0	0.05	-
$\gamma\gamma$	e^+e^-	0.0	0.61	-
	$\mu^+\mu^-$	1.01	1.01	0.10
	$\tau^+\tau^-$	0.90	0.37	0.19
	$q\overline{q}$	0.0	1.01	-
Comptons		0.0	0.30	-
W^+W^-		13.88	0.61	0.00
Total		16.92	1.81	0.26

Table 3.6: Composition of the different backgrounds generated at 189 GeV remaining at the end of the analysis, with their Monte Carlo statistical errors and estimated systematic errors.

$M\widetilde{\tau}_R$	30	40	50	60	70	80	90
$M\tilde{\chi}_1^0$							
10	15.4 ±1.1	20.1±1.3	22.5±1.3	22.1±1.3	23.6±1.3	22.3±1.3	22.8±1.3
20	14.9 ±1.1	22.9±1.3	24.1±1.4	25.6±1.4	27.2±1.4	28.0±1.4	28.7±1.4
30		16.2±1.2	25.3±1.4	26.7±1.4	30.8±1.5	30.5±1.5	29.0±1.4
40			17.2±1.2	26.5±1.4	28.3±1.4	30.9±1.5	34.9±1.5
50				16.3±1.2	27.7±1.4	34.1±1.5	36.2±1.5
60					12.3±1.0	28.0±1.4	35.5±1.5
70						11.2±1.0	28.0±1.4
80							7.6±0.8

Table 3.7: Stau signal efficiency in percentage with error at the end of the analysis for each $\widetilde{\tau}_R - \tilde{\chi}_1^0$ mass combination.

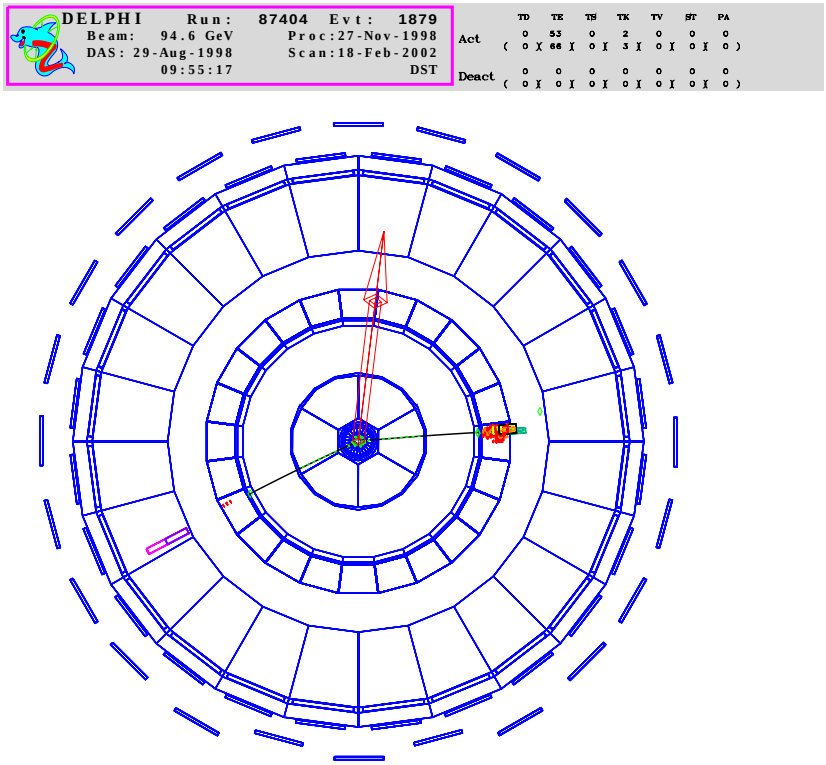

Figure 3.32: Event display of a $\widetilde{\tau}^+\widetilde{\tau}^-$ candidate with an electron and a pion in the final state. The arrow indicates the direction of the missing energy.

3.5 Extension to 1999 data sets

The data collected in 1999 at centre of mass energies of 192 GeV, 196 GeV, 200 GeV,and 202 GeV were analysed using the same sequential cuts. The MC background samples used for the analyses at 192(202) GeV were the ones generated at 189(200) GeV and the ones used for 196 and 200 GeV analyses were generated at those energies. Due to the higher energies, some of the cuts have been rescaled. The same functions calculated using the W^+W^- and staus MC generated at 189 GeV were used in the calculation of the likelihood ratio for the higher energy samples. When forming the probability distribution (p.d.f) for the higher energy samples, the jet momenta were scaled appropriately.

A few of the more important plots are shown in Figures 3.33 to 3.35 for each of the higher energies using the refitted weights. Figure 3.33 shows the jet opening angle distribution after preselection. Figure 3.34 shows the principle variable used in rejecting $\gamma\gamma$ events while Figure 3.35 shows the likelihood ratio used to suppress W^+W^- events. The analysis was tuned on the 189 GeV data but the same cuts were applied for the higher energy samples. The good agreement between data and MC at other energies is an indication of the stability of the analysis as can be seen in Figures 3.33 and 3.34.

The number of expected background events remaining at the end of the analysis for the samples at 196 GeV and 200 GeV, split into the different sources with their Monte Carlo statistical errors and an estimate of systematic errors, as described in Section 3.6, are given in Table 3.8 and in Table 3.9. The number of expected background events for the samples at 192(202) GeV and their errors are calculated by rescaling the values obtained with 189(200) GeV samples to the luminosity acquired at 192(202) GeV. The number of data candidates obtained at 192 GeV, 196 GeV, 200 GeV and 202 GeV are respectively 5, 11, 10 and 3 compared to the background estimates of 2.75, 9.59, 9.70 and 4.73 as listed in Table 3.16.

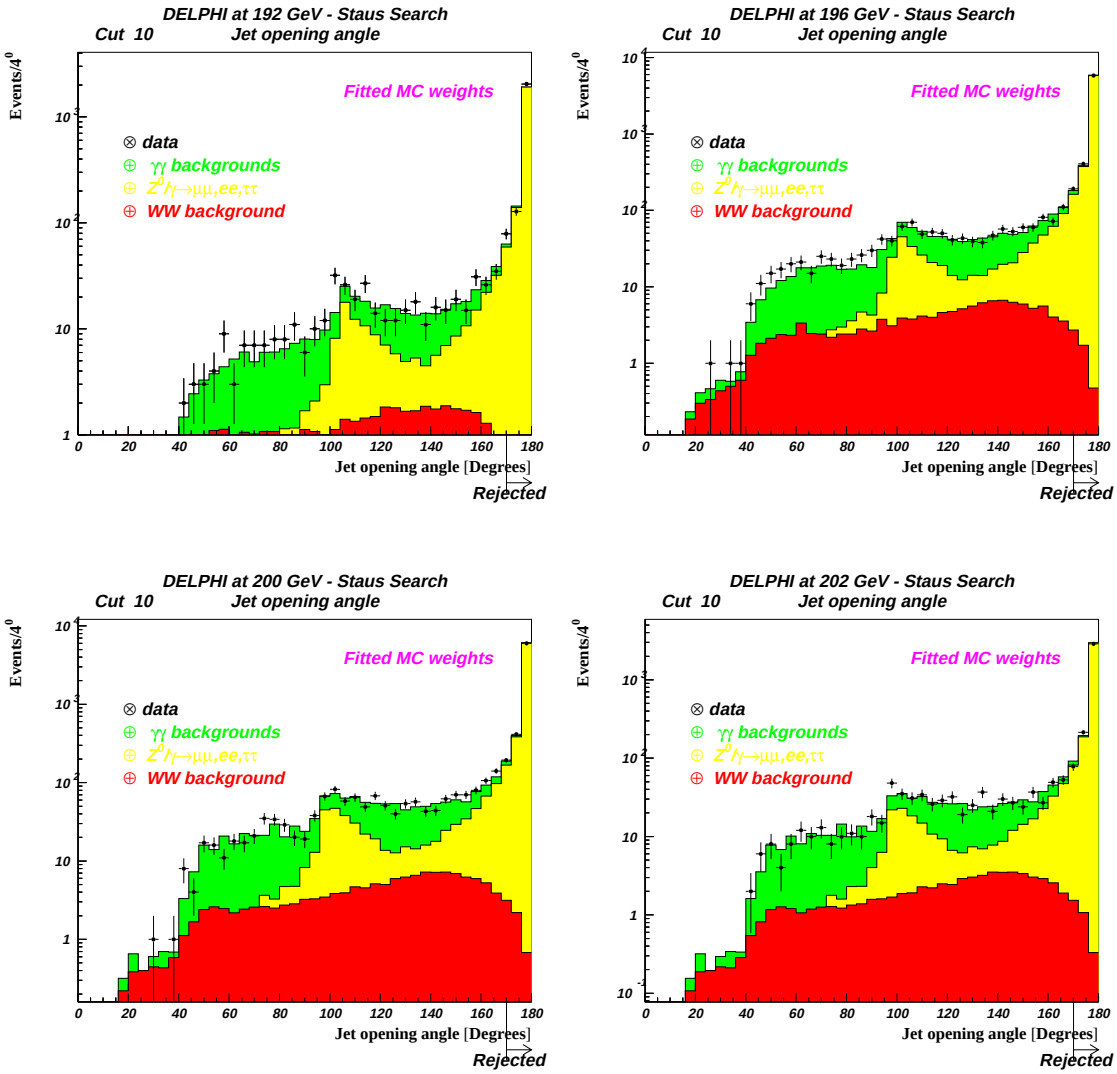

Figure 3.33: Jet opening angle after preselection for data superimposed on the expected backgrounds for 192 GeV (top left), 196 GeV (top right), 200 GeV (bottom left) and 202 GeV (bottom right).

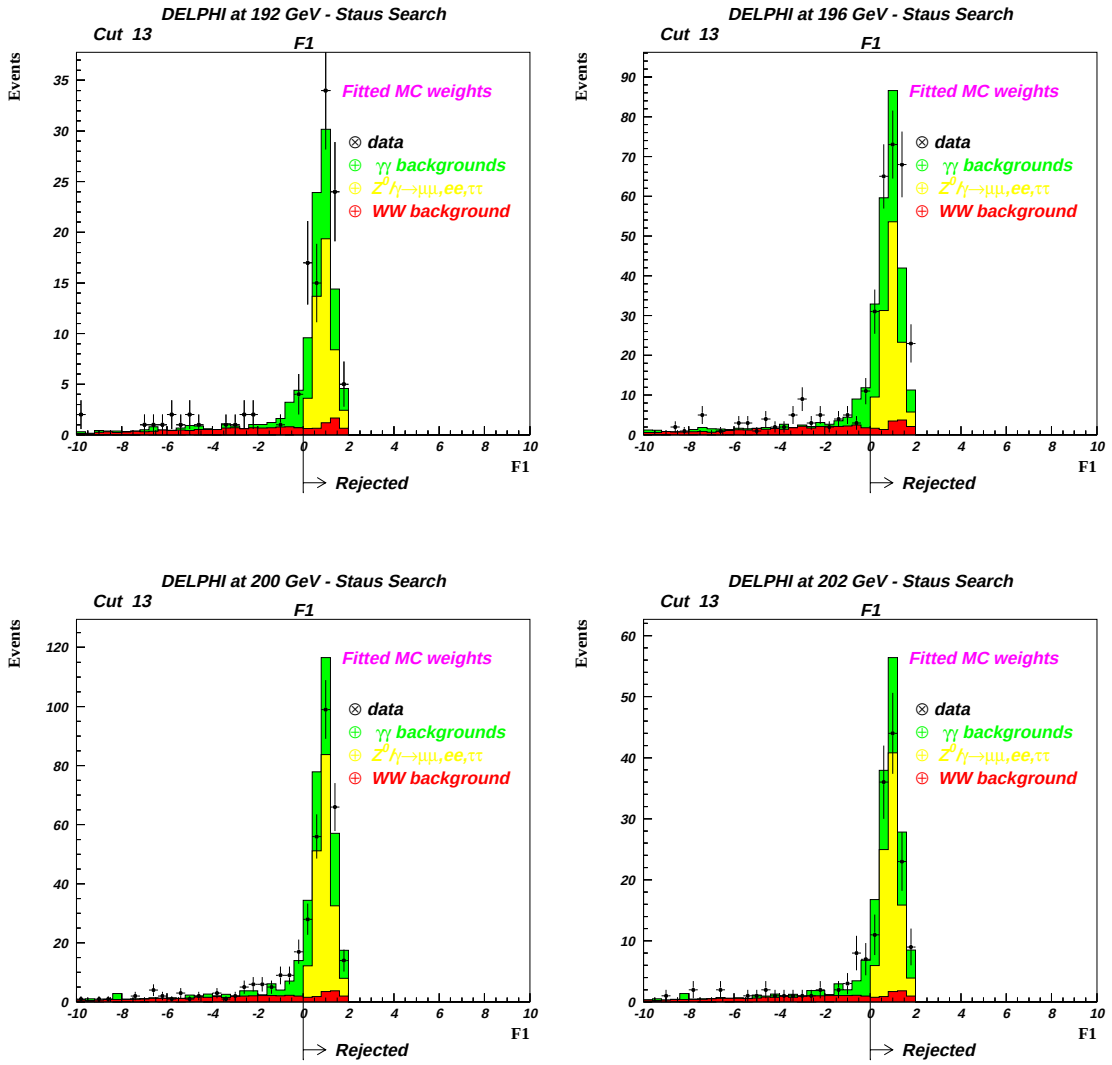

Figure 3.34: Distributions of $F_1 = [cos^2(\theta_{J1}) + cos^2(\theta_{J2})] - 0.075 \times$jets opening angle$+$ 0.15 after cut on p_T^{jets} for the data superimposed on the expected backgrounds for 192 GeV (top left), 196 GeV (top right), 200 GeV (bottom left) and 202 GeV (bottom right).

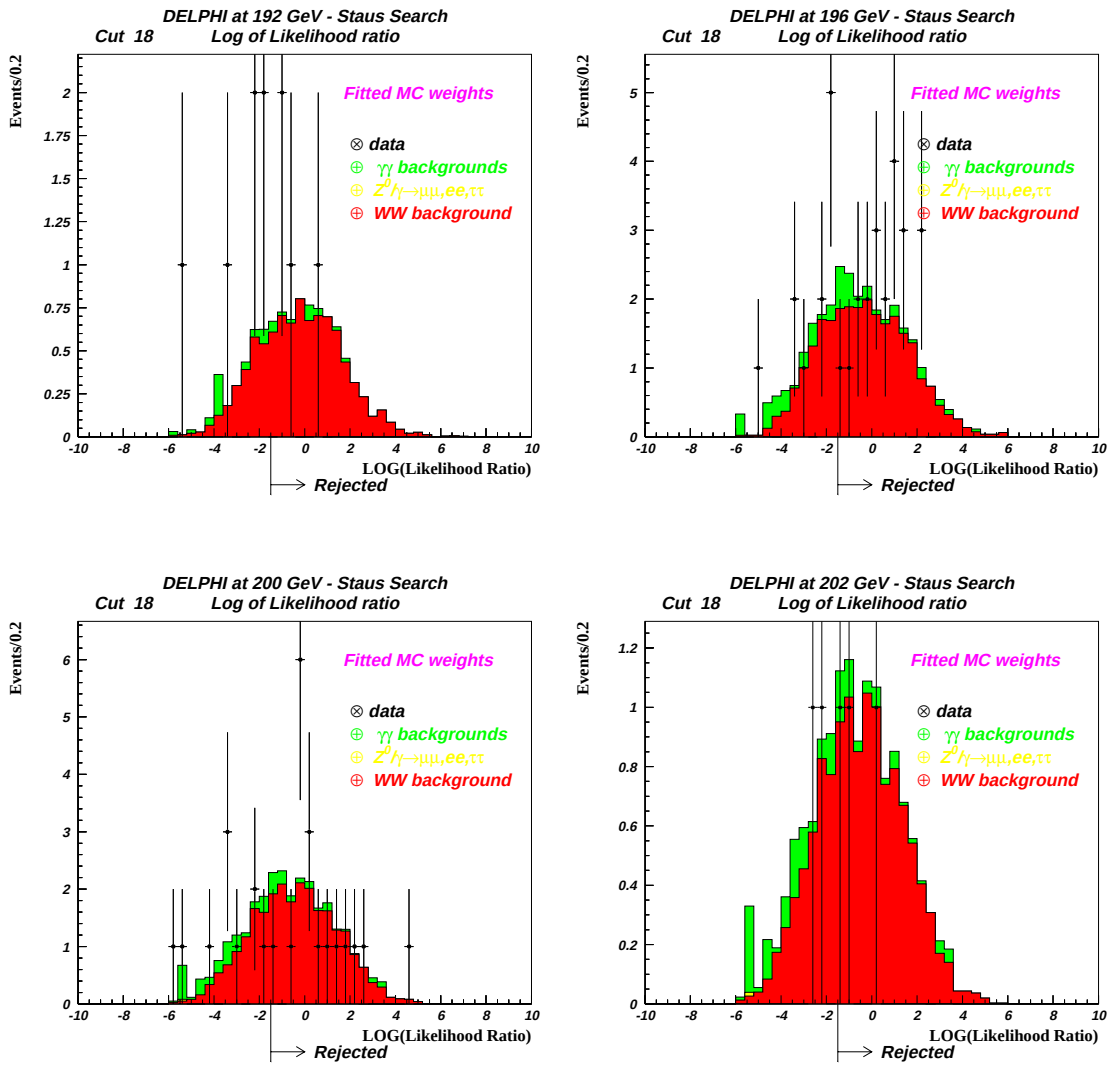

Figure 3.35: Distribution of likelihood ratio for data superimposed on the expected background for 192 GeV (top left), 196 GeV (top right), 200 GeV (bottom left) and 202 GeV (bottom right).

Backgrounds		Events	σ_{stat}	σ_{sys}
2f	e^+e^-	0.0	0.08	-
	$\mu^+\mu^-$	0.0	0.05	-
	$\tau^+\tau^-$	0.53	0.14	0.17
	$q\overline{q}$	0.0	0.07	-
$\gamma\gamma$	e^+e^-	0.0	0.31	-
	$\mu^+\mu^-$	0.31	0.31	0.05
	$\tau^+\tau^-$	1.33	0.44	0.43
	$q\overline{q}$	0.0	0.50	-
Comptons		0.0	0.15	-
W^+W^-		7.42	0.30	0.00
Total		9.59	0.88	0.47

Table 3.8: Composition of the backgrounds generated at 196 GeV at the end of the analysis with their Monte Carlo statistical errors and estimated systematic errors.

Backgrounds		Events	σ_{stat}	σ_{sys}
2f	e^+e^-	0.12	0.12	0.00
	$\mu^+\mu^-$	0.15	0.08	0.02
	$\tau^+\tau^-$	0.83	0.15	0.16
	$q\overline{q}$	0.0	0.07	-
$\gamma\gamma$	e^+e^-	0.47	0.47	0.06
	$\mu^+\mu^-$	0.0	1.04	-
	$\tau^+\tau^-$	0.84	0.35	0.16
	$q\overline{q}$	0.0	0.54	-
Comptons		0.0	0.04	-
W^+W^-		7.29	0.22	0.00
Total		9.70	1.35	0.24

Table 3.9: Composition of the backgrounds generated at 200 GeV at the end of the analysis with their Monte Carlo statistical errors and estimated systematic errors.

3.6 Evaluation of systematic errors

In order to estimate the systematic errors, the agreement between data and expected background was monitored throughout the sequential cut analysis using the large statistic samples at 189 GeV, 196 GeV and 200 GeV. The systematic errors ascribed to the small data samples at 192(202) GeV were taken from the studies of the 189(200) GeV data.

Table 3.10 shows, for the 189 GeV analysis, the number of data events, expected background events and the number of standard deviations by which the data exceeds the simulated background after each cut.

Figure 3.36 shows, for the forward and barrel regions separately, the plots of the jets acolinearity, E_{vis}, p_T^{jets} and the jets acoplanarity after each of the first four cuts of the analysis following the preselection. Significant discrepancies between data and background can be observed, particularly in the forward regions of the detector, where the $\gamma\gamma$ backgrounds are poorly described.

Selection	Barrel			Forward		
	Data	Backgrounds	σ	Data	Backgrounds	σ
Preselection	4447	4524	-1.1	11177	11077	+1.0
Acolinearity	864	798	+2.2	2012	1655	+8.0
E_{vis}	419	380	+1.9	1101	859	+7.3
p_T^{jets}	183	181	+0.2	530	425	+4.6
F_1	78	77	+0.1	76	64	+1.4
F_2	61	60	+0.1	70	54	+1.9
P_{min}	37	40	-0.5	24	21	+0.6
$Log(L_R)$	18	12	+1.4	3	5	-1.2
M_{Inv}	17	11	+1.6	2	5	-2.1

Table 3.10: Number of data, expected background and standard deviations by which data exceed background for the barrel and forward regions during the sequential cuts, using original MC weights for the 189 GeV analysis.

To estimate the impact of these discrepanices on the analysis, a simultaneous fit is performed to the four quasi-independent variables: acolinearity, E_{vis}, p_T^{jets} and $cos^2(\theta_{J1}) + cos^2(\theta_{J2})$ of the jets. The fits are performed separately for the barrel and forward regions of the detector. It is assumed that the simulation adequately

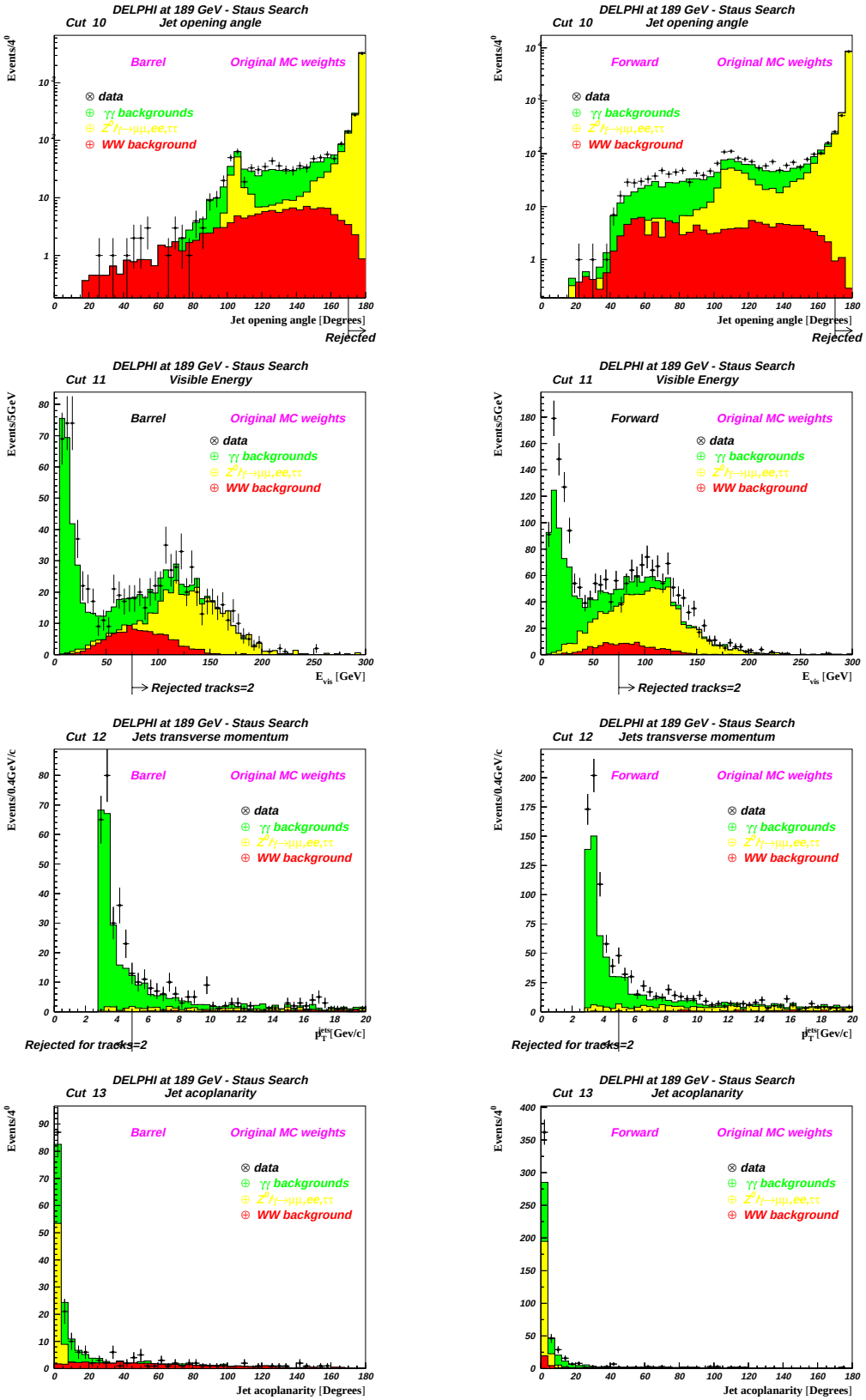

Figure 3.36: Distributions of the jets acolinearity (1st row) at cut 1, Visible Energy (2nd row) at cut 2, p_T^{jets} (3rd row) for barrel (left) and forward (right) at cut 3 and the jets acoplanarity (4th row) at cut 4, for data superimposed on expected background using the original Monte Carlo weights.

describes the shapes of the distributions, but not their normalisation. Consequently, the contributions of the various background sources are allowed to float in the fits, but the simulated shapes of distributions are retained.

In order to make the fitting procedure sensitive to the different background source distributions, three independent categories of events are isolated using lepton identification. Those categories are two tagged electron events or two tagged muon events or neither two electron nor two muon events. The contributions of the various background sources to these three categories are summarised in Table 3.11.

Firstly, for the forward and barrel region samples with two tagged electrons containing 9298 and 3937 events respectively, the dominant background sources are Bhabhas, $(\gamma\gamma)e^+e^-$ and $\tau^+\tau^-$ events. Therefore, in the fitting procedure to the two-electron samples only these background sources are allowed to float.

Secondly, for the forward and barrel region samples with two tagged muons containing 497 and 516 events respectively, the dominant background sources are $\mu^+\mu^-$ and $(\gamma\gamma)\mu^+\mu^-$ and $\tau^+\tau^-$. In addition, these samples show some sensitivity to the W^+W^- background. Thus, in the fits to the two-muon samples, the normalisation of these sources is left free except for the $\tau^+\tau^-$.

Finally, the third samples consisting of all events not falling into the first two categories contain 1294 and 152 events for the forward and barrel regions respectively. These samples show sensitivity to $\tau^+\tau^-$, $(\gamma\gamma)\tau^+\tau^-$ and Bhabhas contributions.

Samples		Forward			Barrel		
		e^+e^- tag	$\mu^+\mu^-$ tag	$e^+e^-/\mu^+\mu^-$ veto	e^+e^- tag	$\mu^+\mu^-$ tag	$e^+e^-/\mu^+\mu^-$ veto
2f	e^+e^-	95%*	-	87%‡	89%*	-	15%‡
	$\mu^+\mu^-$	-	29%†	-	-	50%†	4%
	$\tau^+\tau^-$	1%	14%	5%‡	4%*	18%	46%‡
$\gamma\gamma$	e^+e^-	3%*	-	3%	3%*	-	7%
	$\mu^+\mu^-$	-	38%†	-	-	12%†	-
	$\tau^+\tau^-$	-	8%	4%‡	-	4%	23‡%
W^+W^-		-	11%†	-	2%	15%†	4%

Table 3.11: Composition of the selected samples with lepton identification for forward and barrel for the 189 GeV analysis. The symbols indicate for each sub-sample which backgrounds are fitted (* for e^+e^-; † for $\mu^+\mu^-$; ‡ for $e^+e^-/\mu^+\mu^-$veto).

Samples		Default Weight	189 GeV Barrel e^+e^- tag	$\mu^+\mu^-$ tag	$e^+e^-/\mu^+\mu^-$ veto	Refitted Weight $W \pm \delta\, w$	Δ_W
2f	e^+e^-	.322	.308±.005	-	.315±.198	.308±.005	-.014
	$\mu^+\mu^-$	.112	-	.125±.008	-	.125±.008	+.013
	$\tau^+\tau^-$	.118	.154±.037	-	.12±.015	.125±.014	+.007
$\gamma\gamma$	e^+e^-	.483	.562±.099	-	-	.562±.099	+.078
	$\mu^+\mu^-$	.784	-	.658±.164	-	.658±.164	-.126
	$\tau^+\tau^-$	.148	-	-	.141±.038	.141±.038	-.007
W^+W^-		.0275	-	.0275±.006	-	.0275±.006	+.000

Table 3.12: Mean fitted values in the barrel, for each of the backgrounds for the 189 GeV analysis. The last two columns quote respectively the refitted weight and the difference between the refitted and default weights.

Samples		Default Weight	189 GeV Forward e^+e^- tag	$\mu^+\mu^-$ tag	$e^+e^-/\mu^+\mu^-$ veto	Refitted weight $W \pm \delta\, w$	Δ_W
2f	e^+e^-	.322	.316±.003	-	.300±.008	.315±.003	-.007
	$\mu^+\mu^-$	.112	-	.171±.014	-	.171±.014	+.059
	$\tau^+\tau^-$	.118	-	-	.125±.04	.125±.040	+.007
$\gamma\gamma$	e^+e^-	.483	.638±.076	-	-	.638±.076	+.156
	$\mu^+\mu^-$	.784	-	1.006±.104	-	1.006±.104	+.222
	$\tau^+\tau^-$	.148	-	-	.197±.048	.197±.048	+.049
W^+W^-		.0275	-	.0279±.017	-	.0279±.017	+.000

Table 3.13: Mean fitted values in the forward region, for each of the backgrounds for the 189 GeV analysis. The last two columns quote respectively the refitted weight and the difference between the refitted and default weights.

Tables 3.12 and 3.13 show the reweighting of each background source obtained by the fitting procedure in the barrel and forward detector regions. In the barrel region, the fitted weights are mostly in agreement with the default weights. However, in the forward region, the $\gamma\gamma$ and $\mu^+\mu^-$ background weights are significantly increased. The Bhabha background weight is left practically unchanged, as it was effectively "reweighted" by the electron efficiency correction applied at the end of the preselection (see Section 3.4.1). Since the fitted values for the W^+W^- background were found to be consistent within errors with the original value, the W^+W^- weight was left unchanged.

Table 3.14 summarises the deviations by which the data exceeds the simulated backgrounds in the forward and barrel regions for the first five cuts after preselection of the analysis at 189 GeV, 196 GeV and 200 GeV. As in the 189 GeV analysis, the discrepancies between simulated backgrounds and the data are significant.

Selection	189 GeV		196 GeV		200 GeV	
	σ_{Barrel}	$\sigma_{Forward}$	σ_{Barrel}	$\sigma_{Forward}$	σ_{Barrel}	$\sigma_{Forward}$
Preselection	-1.1	1.0	1.9	0.2	1.2	0.3
Acolinearity	2.2	8.0	0.1	4.1	1.3	4.6
E_{vis}	1.9	7.3	-0.1	4.9	-1.0	2.9
p_T^{jets}	0.2	4.6	-0.6	4.1	-1.2	2.7
F_1	0.1	1.4	-0.3	1.7	0.6	2.1

Table 3.14: Standard deviations by which data exceed background observed for the barrel and forward regions for the first five cuts of the analysis at 189 GeV, 196 GeV and 200 GeV.

The same refitting procedure was applied at 196 GeV and 200 GeV in order to estimate the systematic uncertainties at those energies, yielding similar results to those obtained with the 189 GeV samples.

After reweighting, the agreement between data and Monte Carlo is considerably better (see Table 3.15).

The errors, δw, obtained on the refitted weights of each of the Monte Carlo samples, separately for the forward and barrel region, were converted into systematic errors on the estimate of the number of background events. The systematic error on a MC sample i was calculated by adding in quadrature the barrel and forward contributions

Selection	189 GeV		196 GeV		200 GeV	
	σ_{Barrel}	$\sigma_{Forward}$	σ_{Barrel}	$\sigma_{Forward}$	σ_{Barrel}	$\sigma_{Forward}$
Preselection	0.4	0.5	0.3	0.4	0.1	-0.2
Acolinearity	2.2	3.2	0.3	2.6	1.5	0.9
E_{vis}	1.5	2.1	0.6	1.5	-0.4	-1.6
p_T^{jets}	-0.2	2.7	-0.5	2.4	-2.3	-0.5
F_1	0.1	.3	-0.2	1.1	0.0	1.8

Table 3.15: Standard deviations by which data exceed background observed for the barrel and forward regions using refitted MC weights for the first five cuts of the analysis at 189 GeV, 196 GeV and 200 GeV.

using the following formula:

$$\sqrt{(N_i^{bar} * \delta w_i^{bar})^2 + (N_i^{for} * \delta w_i^{for})^2} \tag{3.6}$$

where $N^{bar}(N^{for})$ is the number of background events predicted by the simulation in the barrel(forward) region and $\delta w^{bar}(\delta w^{for})$ is the error obtained on the refitted weight for the barrel(forward) region.

In the case of the W^+W^- background generated at 189 GeV, a different procedure was used since the refitted weight was found to be consistent within errors with the default weight. At the end of the 189 GeV analysis, the W^+W^- estimates from EXCALIBUR 1.08 was 14.46±0.80 and from EXCALIBUR 1.01 was 13.03±0.92. Since the two estimates are found to be consistent within less than 2σ, no systematic error was ascribed to the W^+W^- background. In the case of the W^+W^- sample generated at 196(200)GeV, one generator, EXCALIBUR 1.08, was used and the W^+W^- background contribution could not be fitted to the data due to low statistics. Therefore, based on the results obtained with the 189 GeV samples, no systematic error was ascribed to those samples.

The systematic errors for the 192(202) GeV analysis were taken as the systematic errors ascribed to the 189(202) GeV samples rescaled to the luminosity acquired at 192(202) GeV.

3.7 Results

Table 3.16 presents the number of data candidates for all energies analysed, as well as the expected number of background events. The statistical errors on the backgrounds are due to finite Monte Carlo statistics and the systematic errors are derived from the fitting procedure described in Section 3.6. Combining all the data taken from 189 GeV to 202 GeV, 48 events are observed, compared to 43.69 ± 3.04 ± 0.66 expected from Standard Model processes, where the first error is statistical and the second is systematic.

Energy GeV	Data	Total background	2 fermions	$\gamma\gamma$ bckg	WW & Compton
189	19	16.92±1.81±0.26	1.13	1.91	13.88
192	5	2.75±0.29±0.04	0.18	0.31	2.26
196	11	9.59±0.88±0.47	0.53	1.64	7.42
200	10	9.70±1.35±0.24	1.1	1.31	7.29
202	3	4.73±0.66±0.12	0.53	0.64	3.55
195.8	48	43.69±3.04±0.66	3.47	5.81	34.42

Table 3.16: Number of data candidates with expected total background from 189 GeV to 202 GeV. The last three columns give the estimated composition of each of the individual backgrounds.

3.7.1 Exclusion limits

The goal of the search is to express the confidence in the presence or absence of a $\widetilde{\tau}$ signal. This can be formulated in terms of two hypothesis tests:

- the null hypothesis where the signal is absent (background only);
- the alternate hypothesis where the signal is present (signal + background).

The number of signal events expected where $\widetilde{\tau} \rightarrow \tau\tilde{\chi}_1^0$ is defined as

$$s = L\ \epsilon\ \sigma\ BR^2 \tag{3.7}$$

where σ is the cross section, L the luminosity, ϵ the selection efficiency and BR the branching ratio of $\widetilde{\tau} \rightarrow \tau\tilde{\chi}_1^0$;

The modified Frequentist Approach adopted at LEP [47] starts by normalising the confidence level observed for a signal+background hypothesis, CL_{s+b} to the confidence level observed for the background only hypothesis, CL_b Thus, the signal confidence level CL_s is defined as:

$$CL_s = \frac{CL_{s+b}}{CL_b} \tag{3.8}$$

The confidence in the signal+background hypothesis is given by the probability that the test-statistic, described below, is less than or equal to the value observed, Q_{obs} in the experiment:

$$CL_{s+b} = P_{s+b}(Q \leq Q_{obs}) \tag{3.9}$$

where

$$P_{s+b}(Q \leq Q_{obs}) = \int_0^{Q_{obs}} P(Q_{s+b}) \tag{3.10}$$

and where $P(Q_{s+b})$ is the probability distribution (p.d.f) of the test-statistic for the signal+background hypothesis. Similarly, the confidence in the background hypothesis is given by the probability that the test-statistic is less than or equal to the value observed in the experiment, Q_{obs}:

$$CL_b = P_b(Q \leq Q_{obs}) \tag{3.11}$$

where

$$P_b(Q \leq Q_{obs}) = \int_0^{Q_{obs}} P(Q_b) \tag{3.12}$$

and where $P(Q_b)$ is the p.d.f of the test-statistic for the background only hypothesis.

The signal hypothesis is rejected at 95% confidence level when $CL_s < 0.05$.

The test statistic chosen is based on the likelihood ratio, $Q = \mathcal{L}(s+b)/\mathcal{L}(b)$, which is the ratio of the probability densities for a given experimental result for the two alternate hypotheses. In our case it is assumed that the number of events follow a Poisson distribution, and therefore $\mathcal{L}(b)$ is taken as being a Poisson distribution of mean value b and $\mathcal{L}(s+b)$ is taken as being a Poisson distribution of mean value $s+b$, where s is the expected number of signal events and b is the number of background events.

The test statistic combining different energies N_E can be written as:

$$Q = \prod_{i=1}^{N_E} \frac{\frac{e^{-(s_i+b_i)}(s_i+b_i)^{n_i}}{n_i!}}{\frac{e^{-b_i} b_i^{n_i}}{n_i!}} = e^{-s_{tot}} \prod_{i=1}^{N_E} \left(1 + \frac{s_i}{b_i}\right)^{n_i} \tag{3.13}$$

where

$$s_{tot} = \sum_{i=1}^{N_E} s_i \tag{3.14}$$

Since $P(Q \leq Q_{obs}) = P(ln(Q) \leq ln(Q_{obs}))$ and since the constant s_{tot} appears on both sides of the expression $ln(Q) \leq ln(Q_{obs})$, the test statistic for background only experiment can be written as:

$$\ln(Q_b) = \sum_{i=1}^{N_E} n_b \ln\left(1 + \frac{s_i}{b_i}\right) \tag{3.15}$$

and the test statistic for signal+background experiment can be written as:

$$\ln(Q_{s+b}) = \sum_{i=1}^{N_E} n_{s+b} \ln\left(1 + \frac{s_i}{b_i}\right) \tag{3.16}$$

where n_b and n_{s+b} come from the Poisson distribution of the number of events for the background only and signal+background hypotheses respectively.

The method consists then of comparing the observed value of the test statistic Q_{obs} with the integration of the distributions expected for the signal+background and background hypotheses. The signal confidence level can then be expressed as:

$$CL_s = \frac{P_{s+b}(Q \leq Q_{obs})}{P_b(Q \leq Q_{obs})} \tag{3.17}$$

3.7.2 Stau mass limits calculation

In order to obtain an exclusion limit on the $\widetilde{\tau}_R^+\widetilde{\tau}_R^-$ production, CL_s was calculated for each $M_{\widetilde{\tau}_R} - M_{\widetilde{\chi}_1^0}$ point. For each mass point hypothesis, an additional cut on the data and background candidates was placed using the expected maximum momentum of the visible τ coming from the $\widetilde{\tau}$ decay. Furthermore, the signal efficiency for each mass point was taken into account. A particular mass point hypothesis is then rejected as being inconsistent with the data at 95% confidence level, when $CL_s < 0.05$. By combining the CL_s obtained at each mass, an exclusion region is derived where a $\widetilde{\tau}$ signal has not been observed at 95% confidence level. Figure 3.37 shows the 95% CL $\widetilde{\tau}_R$ exclusion region obtained by combining the data at 189, 192, 196, 200 and 202 GeV (shaded region).

A stau mass limit can be set at 65 GeV/c^2 for mass differences between the stau and the neutralino above 15 GeV/c^2.

As well as calculating a data confidence level CL_s^{data} using the data and background candidates and the expected signal, it is also possible to calculate an expected

confidence level, $CL_s^{exp\ x\%}$, for background only experiments. Using $CL_s^{exp\ x\%}$, it is possible to define the 95% confidence level region for which $x\%$ background only pseudo-experiments would have given a higher limit. For instance, the $CL_s^{exp\ 50\%}$ exclusion curve indicates the region where 50% of background only experiments, would give a result lower/higher than the one indicated by the line. Similarly, the $CL_s^{exp\ 70\%}$ exclusion region indicates that 30%(70%) of background only experiments would give a limit lower(higher) than the line obtained. The contours for $CL_s^{exp\ 5\%}$ and $CL_s^{exp\ 95\%}$ are also shown in Figure 3.37. The different curves indicate the range for which background only experiments could be expected to fluctuate.

As one can see in Figure 3.37, the contour corresponding to $CL_s^{exp\ 70\%}$, fits the best to the data. One can conclude that in the absence of signal, 70% of background only pseudo-experiments would have given a limit higher than the one obtained with data.

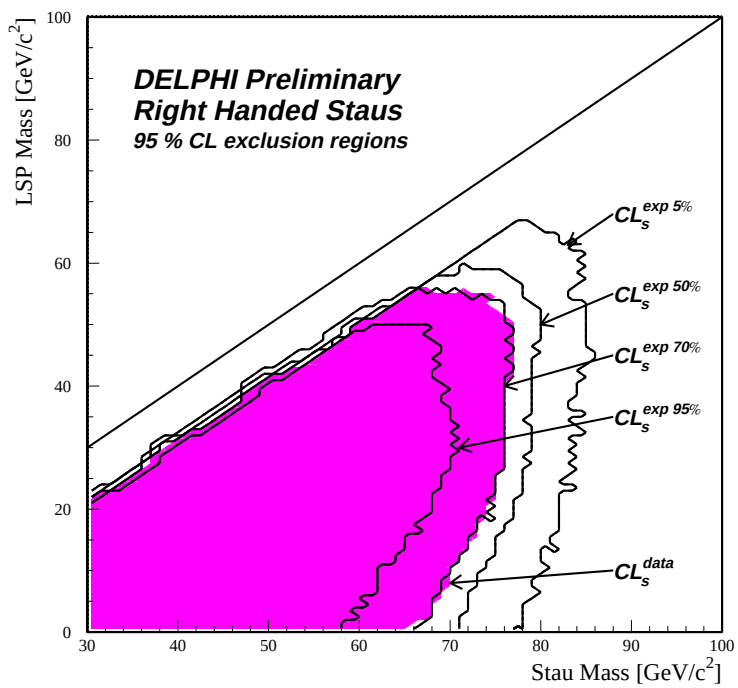

Figure 3.37: Mass limit for the scalar Stau 95% CL exclusion region. The purple region shows the data exclusion limit, and the solid curves show the expected limits obtained by 95%, 70%, 50% and 5% of background only experiments. The wiggles on solid curves are non-physical and are due to statistical fluctuations.

In order to have an estimate of how much the systematic and statistical errors can influence the data limit, the limit has been recomputed by fluctuating each background composition by $\pm$ 1 sigma of the total error, where the total error

is defined as the quadratic sum of the systematic and statistical errors. Since the W^+W^- is the dominant background, the maximum fluctuation in the data limit was obtained for this background. Figure 3.38 shows the exclusion limit for data (purple), the exclusion limit subtracting 1σ from the W^+W^- background, $CL_s^{data}(-1\sigma W)$, and the exclusion limit adding 1σ from W^+W^- background, $CL_s^{data}(+1\sigma W)$. The obtained limit varies at most by 2 GeV/c^2, and therefore, it can be concluded that the mass of the stau is greater than 63 GeV/c^2 at 95% confidence level where the difference between the stau and the LSP mass is greater than 15 GeV/c^2.

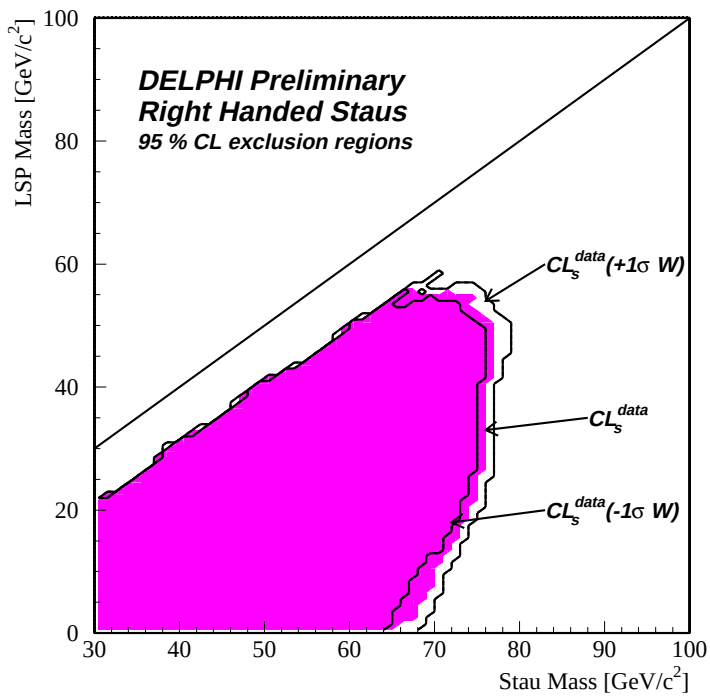

Figure 3.38: Mass limit for the scalar Stau 95% CL exclusion region. The purple region shows the obtained exclusion limit, and the lower solid lines show the data limit subtracting 1σ to the W^+W^- background and the higher solid lines show the data limit adding 1σ to to the W^+W^- background.

3.8 Model dependence on the stau limit

The stau limit obtained was computed using the conservative set of MSSM parameters recommended by the LEP SUSY Working group [9], $\mu = -200$ GeV/c^2 and $\tan\beta = 1.5$, where the limits on neutralinos from chargino and neutralino searches are the weakest. The cross section for the production of staus is not dependent on $\tan\beta$, however the branching ratio of $\tilde{\tau} \to \tilde{\chi}_1^0\ \tau$ is slightly reduced for large values of

$\tan\beta$ due to the onset of the process $\tilde{\tau}_R^{\pm} \rightarrow \nu_\tau + \tilde{\chi}_1^{\pm}$. Varying the value of μ affects the neutralino mass spectrum and therefore the branching ratio $\tilde{\tau} \rightarrow \tilde{\chi}_1^0\ \tau$.

It was shown that for $\mu = -100$ GeV/c^2, the stau mass limit is approximately 2 GeV/c^2 higher and that for $\tan\beta = 35$, the stau mass limit is about 1 GeV/c^2 lower [48].

3.9 Conclusion

Data taken by the DELPHI detector at centre of mass energies between 189 GeV and 202 GeV, corresponding to an integrated luminosity of 378.2 pb^{-1} were used to search for the scalar partner of the tau. In this analysis, the MSSM model with conservation of R-Parity is assumed. Consequently the stau is assumed to be pair produced and to decay to a tau plus the lightest neutralino ($\tilde{\tau} \rightarrow \tilde{\chi}_1^0\ \tau$).

With this analysis, 48 data events were selected when 43.69 $\pm$ 3.04 (stat.) $\pm$ 0.66 (sys.) background events are expected, where the dominant background came from W^+W^- decays. These results do not show evidence of physics beyond the Standard Model.

It is concluded that the mass of the stau is greater than 63 GeV/c^2 at 95% confidence level if the difference between the stau and the LSP mass is greater than 15 GeV/c^2.

The LEP experiments have ceased taking data since the 2nd of November 2000 and the construction of the Large Hadron Collider (LHC) is underway. During the 2000 data taking, the LEP2 collider ran at centre of mass energies up to 209 GeV thus probing further the SUSY parameters space. The preliminary results combining the data taken by the four LEP experiments [9], show no evidence of supersymmetry. The LEP results found that the right-handed stau mass limit is $m_{\tilde{\tau}_R} \geq 87$ GeV/c^2, the lightest chargino mass limit is $m_{\tilde{\chi}_1^{\pm}} \geq 103$ GeV/c^2 and the neutralino mass limit is $m_{\tilde{\chi}_1^0} \geq 47$ GeV/c^2.

Chapter 4

The CDF detector at FERMILAB

4.1 Introduction

This chapter introduces the TEVATRON proton-antiproton ($p\bar{p}$) collider at the Fermi National Accelerator Laboratory and the Collider Detector at FERMILAB (CDF). The TEVATRON, built in 1985 near Chicago, is and will remain the highest energy particle collider in the world until the start of the LHC at CERN. The data collected during Run I of the TEVATRON, between 1987 and 1996, allowed the two general purpose experiments, D0 and CDF, to make precision tests of the SM. These included the precision measurement of the W-boson mass and many of the b hadron lifetimes, a first attempt to measure CP-violation in the b-quark sector and, most importantly, the discovery of the t-quark.

For the past five years, the TEVATRON has been upgraded to increase the centre of mass energy of the proton and anti-proton collisions from 1.8 TeV to 2 TeV and to increase the frequency of the $p\bar{p}$ interactions. The increase in luminosity by up to a factor of 20 for Run IIa and the increase in centre of mass energy will extend the kinematic reach in transverse momentum and therefore extends the physics reach.

The CDF detector comprises a series of sub-detectors providing tracking information for charged particles, calorimetry energy deposit, muon identification and luminosity measurement. The CDF collaboration has completed a major upgrade of its tracking detectors, muon detectors and trigger system and has installed new forward calorimeters. From June 2001 to the beginning of October 2001, the upgraded CDF detector has started data collection with the main goal of commissioning the detector.

After a very brief description of the TEVATRON accelerator, the CDF detector is described, with special attention to the features used in the implementation of a cosmic ray tagger and in the identification for the first Run IIa $Z^0/\gamma^* \rightarrow \mu^+\mu^-$ signal.

4.2 The TEVATRON Accelerator

This section describes briefly the TEVATRON for Run IIa, additional information can be found in [49].

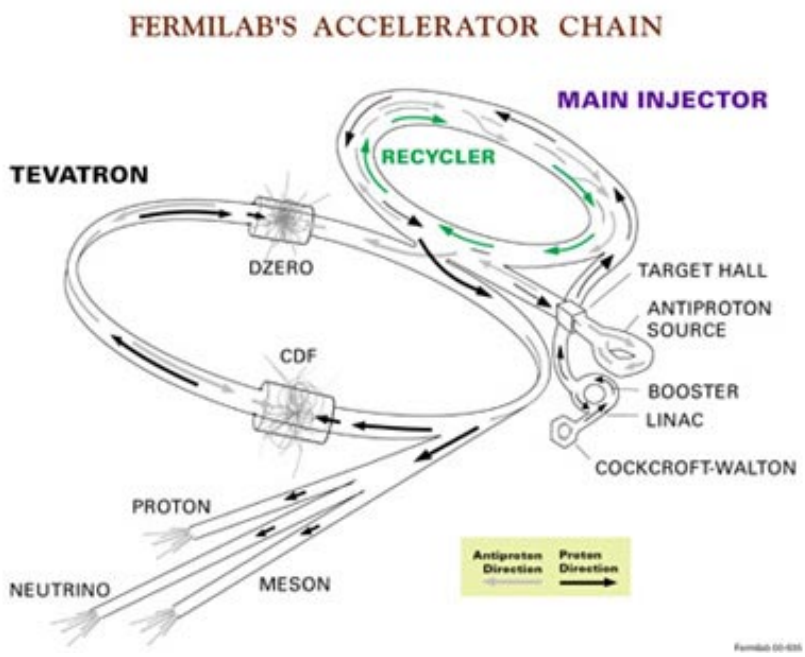

Figure 4.1: The FERMILAB accelerators

Figure 4.1 shows the path taken by the protons and anti-protons in the FERMILAB accelerators. The proton beam is created from hydrogen gas ions, H^-, which are accelerated by the Cockcroft-Walton accelerator to an energy of 750 keV. The H^- ions are then injected in to the Linac and accelerated to 400 MeV. Once the ions leave the Linac, they pass through a carbon foil, which removes the electrons, leaving only the positively charged protons. The protons are then accelerated in the Booster to 8 GeV before being injected into the Main Injector.

The Main Injector (MI), completed in 1999, has four functions:

- It accelerates protons from 8 GeV to 150 GeV.

- It produces 120 GeV protons, which are used for antiproton production.
- It receives antiprotons from the Antiproton Source and increases their energy to 150 GeV.
- It injects protons and antiprotons into the TEVATRON.

The $\bar{p}$ are produced by the collision of the 120 GeV protons provided by the MI onto a nickel target. The collisions produce a wide range of secondary particles including $\bar{p}$, which are then collected, focused and stored in the Accumulator ring. When a sufficient number of antiprotons has been produced, they are sent to the MI for acceleration and injection into the TEVATRON. Inside the Main Injector tunnel, an Anti-proton Recycler has been installed in order to to increase the number of $\bar{p}$ at the beginning of each store by a factor of two. The Recycler will allow the recovery of the $\bar{p}$ and reuse them in a later store. Additionally, the Recycler will also allow the existing Antiproton Source to perform more efficiently and produce more antiprotons per hour.

The TEVATRON receives 150 GeV protons and antiprotons from the MI and accelerates them to 1 TeV. Since the p and $\bar{p}$ have opposite charge, the same ring with the same magnetic field is used to circulate the $\bar{p}$ in the opposite direction to the p.

When the TEVATRON operates in collider mode, the 36 bunches of p collide with 36 bunches of $\bar{p}$. Each bunch of protons is designed to contain about 2.7×10^{11} p, while each bunch of $\bar{p}$ would contain 3×10^{10} $\bar{p}$. The low beta quadrupole magnets near the two experimental interaction points, focus the beams to achieve maximum luminosity. Current Run IIa data indicate an interaction region of about $\sim 40\mu m$ in $R\phi$ with an rms of 22 cm along the z direction. The beam crossings occur every 396 ns. The design instantaneous luminosity, $\mathcal{L}$, for Run IIa is $0.86 \times 10^{32} cm^{-2} s^{-1}$, corresponding to an average of ~ 2.3 interactions per crossing. Table 4.1 summarises the run parameters for Run 1b and Run IIa [49].

4.3 The CDF Detector

The CDF detector is a solenoidal detector with forward-backward and azimuthal symmetry. It comprises tracking chambers inside a superconducting magnet of 1.4 T with electromagnetic and hadronic calorimeters and muon chambers. Figure 4.2 shows a 3-dimensional perspective of the detector with the main components indicated.

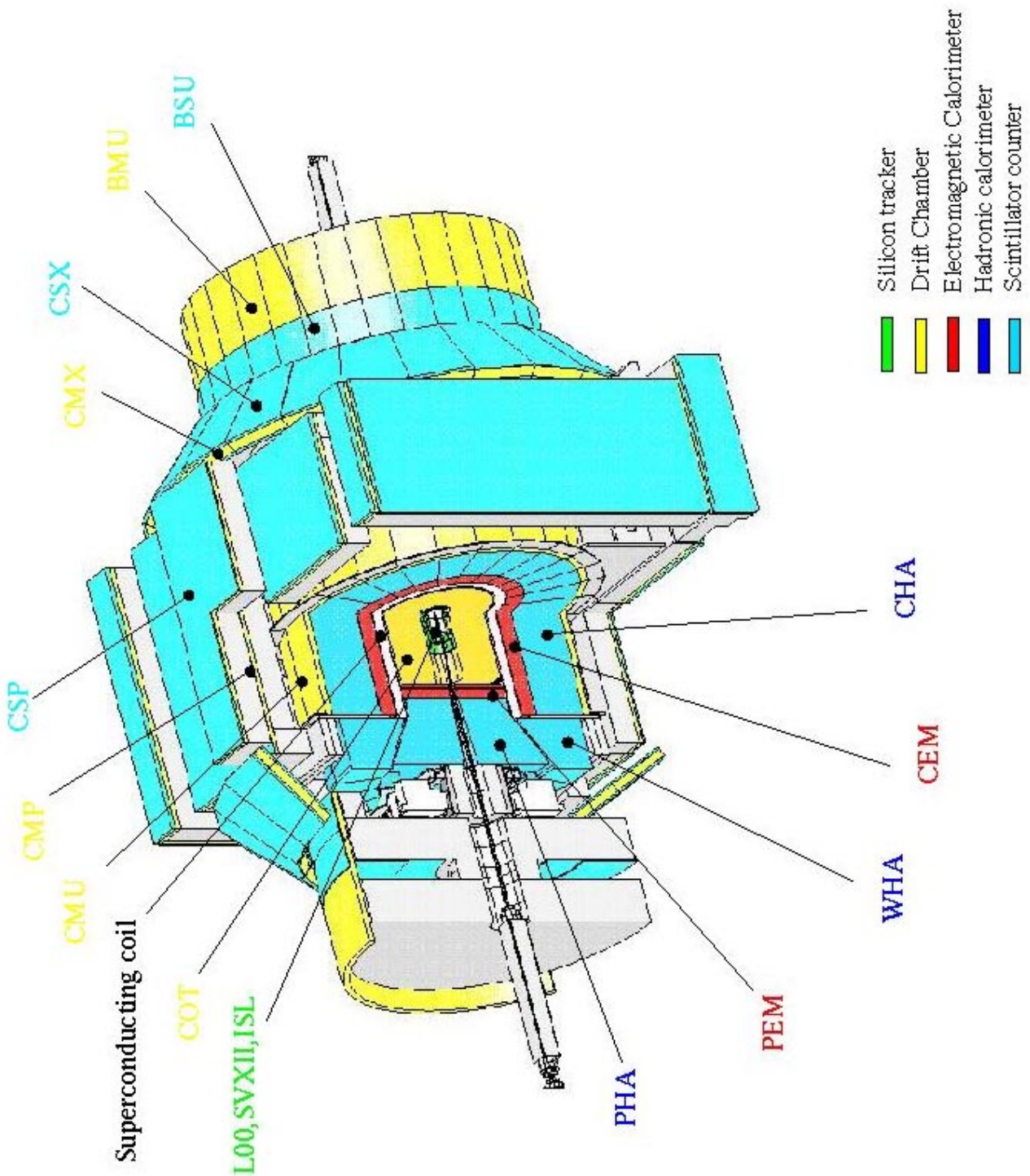

Figure 4.2: The CDF detector

Run	Run 1b (93-95) (6x6)	Run IIa (foreseen) (36x36)	Units
p/bunch	2.3×10^{11}	2.7×10^{11}	
$\bar{p}$/bunch	5.5×10^{10}	3.0×10^{10}	
Total Antiprotons	3.3×10^{11}	1.1×10^{12}	
$\bar{p}$ production rate	6.0×10^{10}	1.0×10^{11}	hr^{-1}
Energy	900	1000	GeV
$\bar{p}$ bunches	6	36	
Bunch length (rms)	0.6	0.37	m
Typical Luminosity	0.16×10^{31}	0.86×10^{32}	$cm^{-2}s^{-1}$
Integrated Luminosity	3.2	17.3	pb^{-1}/week
Bunch spacing	~ 3500	396	ns
Interactions/crossing	2.5	2.3	

Table 4.1: Run 1b and Run IIa foreseen parameter list

The nominal interaction point is assumed to be at (0,0,0) in the geometrical centre of the detector. The CDF coordinate system is defined as follows: the z axis is along the proton direction (eastward at CDF), the x axis points horizontally outward from the centre of the ring (northward at CDF) and the y axis points vertically upward.

The rest frame of the hard collision is generally boosted relative to the lab frame along the beam direction. The detector solid angle segmentation is designed to be invariant under boost along the z direction. The angular coordinates η and ϕ are used to describe the particle kinematics and to define the angular segmentation of the detector. The azimuthal angle ϕ is defined with respect to the x axis and $\phi = 0$ is the positive x axis. The pseudo-rapidity, η is a relativistic limit of rapidity, $\mathcal{Y}$, defined as:

$$\mathcal{Y} \equiv \frac{1}{2} \ln \frac{E + p_z}{E - p_z} \tag{4.1}$$

$$\eta \equiv -\ln \tan \frac{\theta}{2} \tag{4.2}$$

The pseudo-rapidity, η is equivalent to the rapidity, $\mathcal{Y}$, of a particle in the limit of $p >> m$ where p is the momentum of a particle and m is its mass.

Because of the forward scattered particles (the remnants of the p and $\bar{p}$), also refered to as the underlying event, the total momentum in the event cannot be measured. In this case, the useful variables are the transverse momentum, p_T, and the transverse energy, E_T. For particles with momenta large compared to their masses, the E_T

and p_T are nearly identical. However, the convention used is that E_T refers to the energy measured by the calorimeters, while p_T refers to the momentum measured by the tracker.

Since this chapter concerns muon identification and cosmic ray rejection, only the relevant detector components will be described. Additional information concerning the upgrade of the CDF detector for Run IIa can be found in [50].

4.3.1 Tracking detectors

The tracking detectors lie inside a 1.4 T solenoidal field. They consist of the silicon detectors (Layer00, SVXII and ISL) and the Central Outer Tracker (COT). Figure 4.3 shows a quadrant of the CDF tracking system.

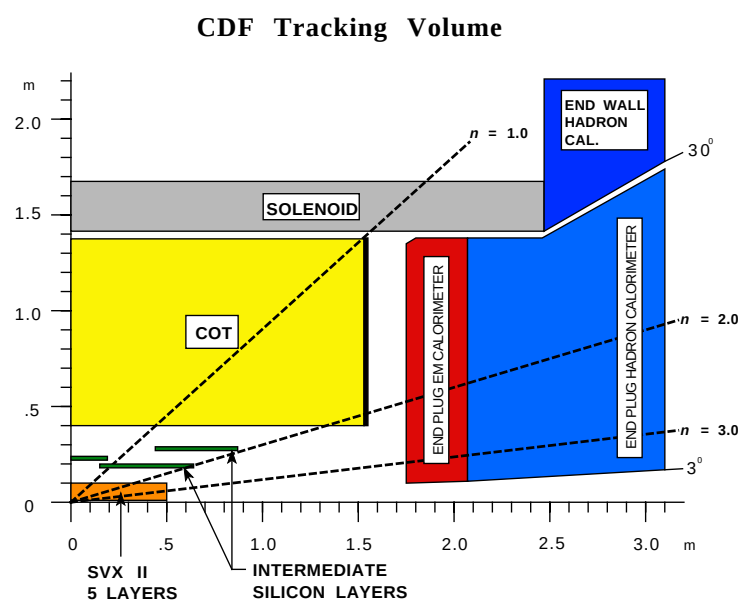

Figure 4.3: Quadrant of the CDF tracking system

Silicon detectors

The silicon tracking system consists of eight layers arranged in cylinders spanning radii from 1.35 cm to 29 cm, and lengths from 90 cm to nearly two meters (see Figure 4.4) . Table 4.2 details the specification of the CDF silicon trackers.

Layer 00 [51] consists of single sided radiation tolerant silicon detectors assembled on a low mass carbon fiber structure with integrated cooling and mounted

Layer	z coverage (cm)	Radii (cm)	Axial pitch(μm)	Stereo Angle	Stereo pitch (μm)
1 Layer 00	$\|z\| < 96$	1.35-1.62	25	-	-
2 SVX	$\|z\| < 94$	2.5-3.0	60	90°	141
3 SVX	$\|z\| < 94$	4.1-4.6	62	$+1.2^o$	125.5
4 SVX	$\|z\| < 94$	6.5-7.0	60	90°	60
5 SVX	$\|z\| < 94$	8.2-8.7	60	90°	141
6 SVX	$\|z\| < 94$	10.1-10.6	65	-1.2^o	65
7 ISL forward	$20 < \|z\| < 64$	19.7-20.2	112	$\pm 1.2^o$	112
7 ISL central	$\|z\| < 22$	122.6-23.1	112	$\pm 1.2^o$	112
8 ISL forward	$42 < \|z\| < 87$	28.6-29.0	112	$\mp 1.2^o$	112

Table 4.2: Specifications the CDF silicon tracking detectors.

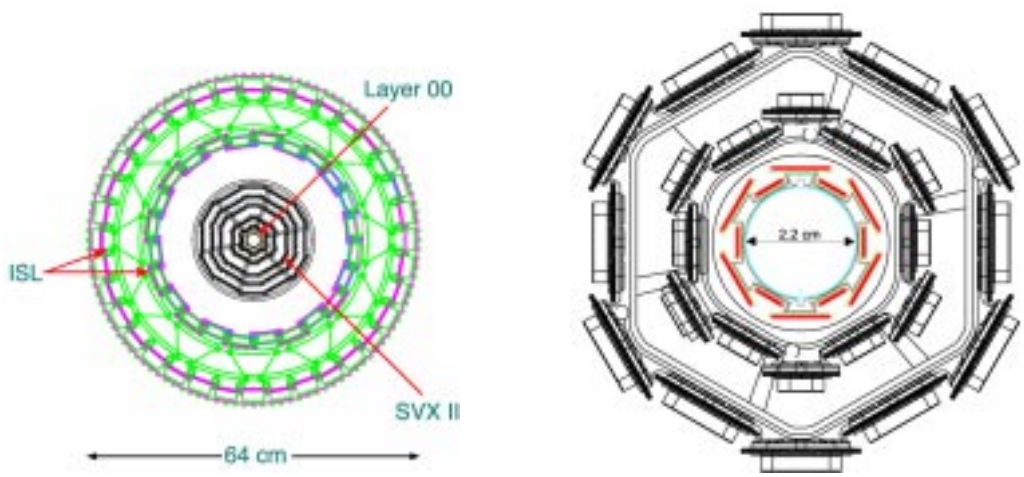

(a) (b)

Figure 4.4: (a) End view of the CDF silicon system including the SVX II cooling bulkheads and ISL support structure. (b) End view of the innermost three layers of silicon system, showing Layer 00 along with the first two layer of the SVX II.

on the beam pipe. The design has six narrow (128 channels) and six wide (256 channels) groups in $R\phi$. There are six readout modules in z, with two sensors bonded together in each module. The readout chips are mounted on each side beyond the end of the silicon. The sensors are connected to readout chips via fine-pitch kapton cables. The main aim of Layer 00 is to improve the impact parameter resolution.

SVX II consists of three barrels each 29 cm long with five layers of double sided silicon and 12 wedges in ϕ. Of the five layers, three have 90° stereo while two have 1.2^o small angle stereo. This design permits good resolution in locating the z position of the secondary vertices and enhances the 3-dimensional pattern recognition capability of the silicon tracker.

ISL consists of one (two) cylinders of double sided silicon in the central (forward) region. Along with linking tracks in the COT to SVX II, the ISL enables silicon stand alone forward tracking, and extends the coverage for vertexing and b-tagging to $|\eta| = 2$.

The Central Outer Tracker (COT)

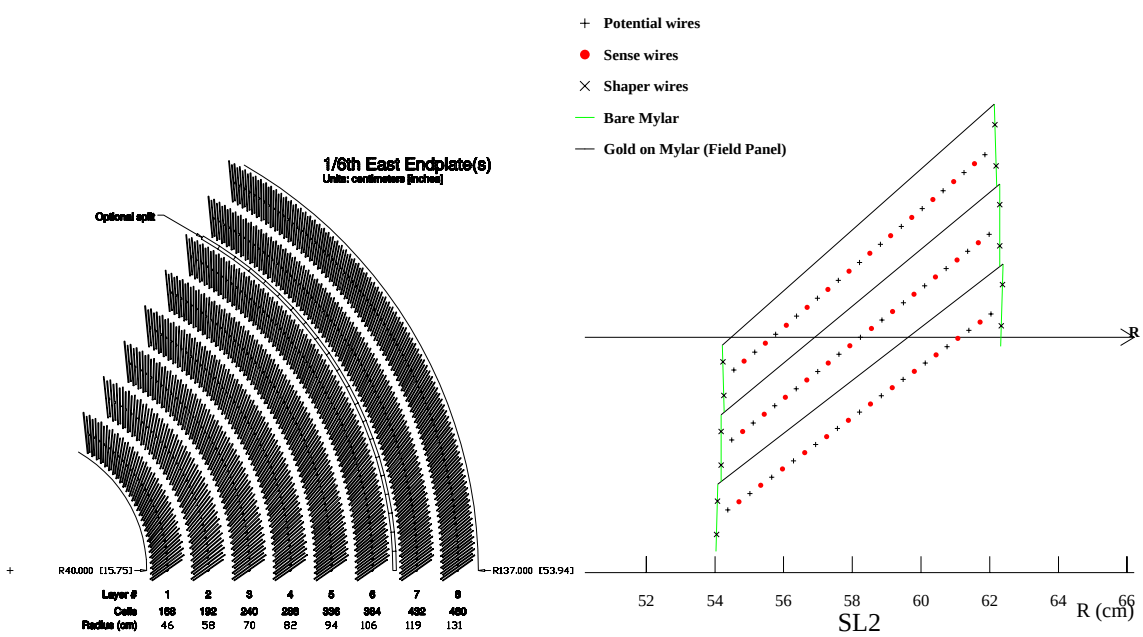

(a) (b)

Figure 4.5: (a) $1/6^{th}$ of a COT end plate showing the arrangement of the slots which hold the sense wires. (b) Cell layout for SL-2.

The main tracking detector of CDF is an open cell drift chamber, called the Central Outer Tracker (COT) [52]. The COT is 3.1 m long and extends from radii of 40 cm

to 137 cm. It contains 96 concentric cylindrical layers of sense wires grouped into 8 "super-layers" (see Figure 4.5). Forty-eight layers have wires parallel to the beam direction (axial layers) and provide tracking in the $R\phi$ plane. Forty-eight layers (stereo) are titled at $\pm 3^o$ with respect to the beam direction. Together, the axial and stereo information provides 3 dimensional tracking within a pseudo-rapidity range of $|\eta| < 1.1$.

The tracking momentum resolution of the CDF RunII tracker is estimated to be $\delta p_T/p_T = 0.08\%\ p_T$, for tracks with $p_T > 10$ GeV/c [50].

4.3.2 Calorimeters

The electromagnetic and hadronic calorimeters cover a solid angle close to 4π. All CDF calorimeters use a projective tower geometry with constant $\Delta\eta$ towers that point back to the nominal interaction region. Since this chapter deals with muon identification within $|\eta| < 1.0$, only the central calorimeters which cover the η regions $0 \leq |\eta| \leq 1.1$ are described. Additional information can be found in [50].

Electromagnetic Calorimeters

The Central Electromagnetic Calorimeter (CEM) is divided into 24 wedges, where each wedge covers 15° in ϕ and 0.1 in η. A CEM wedge consists of 31 layers of 3.2 mm thick lead converter alternating with 5 mm thick layers of plastic scintillators (see Figure 4.6). The CEM is about 19 radiation lengths in depth. Its energy resolution is measured to be $13.5\%/\sqrt{E_T} \oplus 2\%$ from test beam data[1] [50].

Hadronic Calorimeters

The Central and End wall Hadron Calorimeter (CHA, WHA) consists of 32 layers of 2.5 cm thick steel absorber alternating with layers of 1 cm thick plastic scintillator and is about 4.5 interaction lengths in depth. Its energy resolution is $50\%/\sqrt{E_T} \oplus 3\%$ [53]. Towers in the region $0.7 \leq |\eta| \leq 0.9$ are shared between the WHA and the CHA; a particle in this region passes through the CHA, then the WHA. Particles in the region $0.9 \leq |\eta| \leq 1.3$ are only measured by the WHA. The WHA are 15 layers of 5.1 cm thick steel absorber alternating with plastic scintillator. The WHA is about 4.5 interactions lengths in depth. Its energy resolution is

[1] In Run I its energy resolution was measured to be $13.7\%/\sqrt{E_T} \oplus 2\%$ [53]

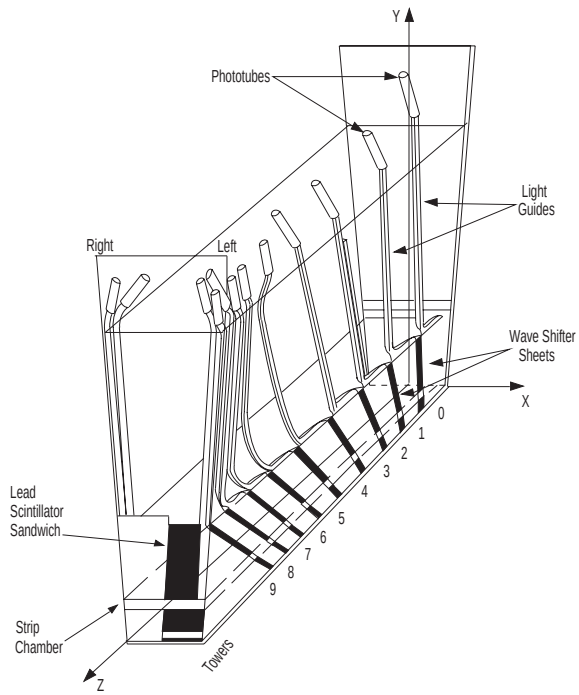

Figure 4.6: A wedge of the central electromagnetic calorimeter (CEM).

$75\%/\sqrt{E_T} \oplus 4\%$ [53].

Both of these hadron calorimeters have TDCs which provide timing information for the energy deposition. If an electromagnetic shower deposits enough energy ($\geq$ 300 MeV) in a single hadronic tower, timing information will be recorded. At Run I, the time resolution of these TDCs was 1 ns.

4.3.3 Muon Chambers

The central muon chamber (CMU and CMP) and the central extension (CMX) are used to identify muons within a region $|\eta| \leq 1$. The BMU provides muon identification in the region $1 \leq |\eta| \leq 2$. The BMU is not discribed here, additional information can be found in [50]. Figure 4.7 shows the $\eta - \phi$ coverage of the muon chambers.

The Central Muon Detector (CMU)

The central calorimeters act as hadron absorber for the CMU, which consists of four layers of drift chambers located outside the CHA. There are 144 modules with 16 rectangular cells per module. Each cell has a 50 μm stainless steel wire in the centre. The 16 cells are stacked four layers deep in the radial direction, with a small offset

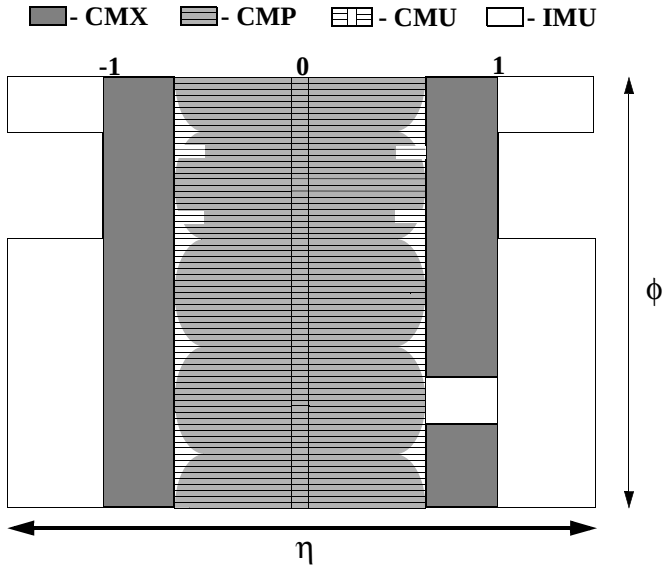

Figure 4.7: Coverage of the muon chambers in the $\eta - \phi$ plane. The ϕ scale is from 0 to 2π.

in ϕ between 1st and 3rd, and 2nd and 4th layers. The 1st and 3rd (2nd and 4th) ϕ cells have their wires ganged together in the readout. Each wire pair is instrumented with a TDC to measure the muon location in ϕ and an ADC on each end measures the muon location in z via charge division. The CMU covers the region $|\eta| < 0.6$.

The Central Muon Upgrade (CMP)

The CMP consists of a second set of muon chambers behind an additional 60 cm of steel in the region $55^o \leq \theta \leq 90^o$. The return yoke of the CDF solenoid provides the necessary steel above and below the CMP. As a result, it was necessary to add steel only on the two sides in a form of a non-magnetised retractable walls. The chambers are of fixed length in z and form a box around the central detector, therefore the actual pseudo-rapidity coverage varies with azimuth as shown in Figure 4.7. The CMP chambers are rectangular, single wire drift tubes configured in four layers with alternate half-cell staggering. The chambers run in proportional mode with a maximum drift time of approximately 1.4 μs. The tubes are made of aluminum extrusions with 0.26 cm walls, having a single wire in the centre and field shaping cathode strips on top and bottom (see Figure 4.8). The CMP covers the region $|\eta| < 0.6$, being behind additional absorber it is particularly useful in reducing fake muons coming from punch-through from energetic hadrons.

A layer of scintillator counters (CSP) is installed on the outside surface of the wall drift chambers. Each counter covers two upgrade chambers in width and half the

chamber length.

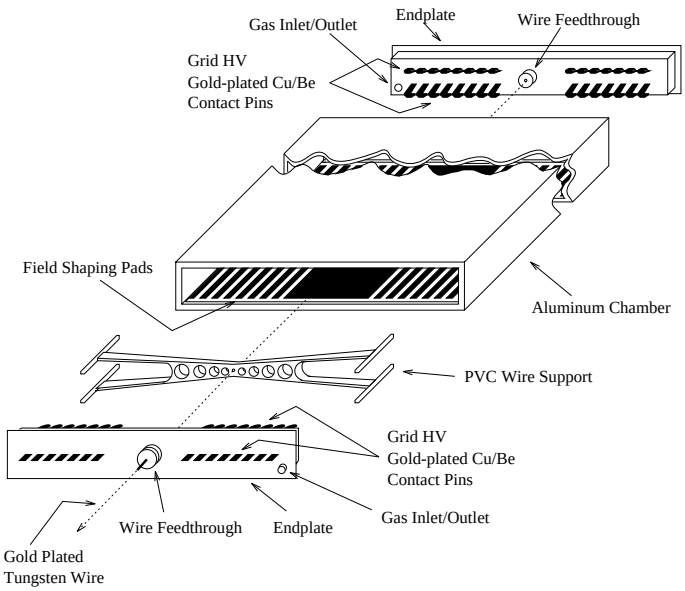

Figure 4.8: Schematic view of a CMP-CMX tube.

The Central Muon Extension (CMX)

The central extension consists of conical sections of drift tubes (CMX) and scintillation counters (CSX) located at each end of the central detector and extending in polar angle from 42° to 55°. At 55°, the CMX/CSX system slightly overlap the coverage provided by the central muon system, thus extending its $|\eta|$ coverage from 0.6 to 1.0. The CMX drift tubes are arrayed as a logical extension of the central system. There are four logical layers of twelve tubes for each 15° ϕ sector, and successive layers are half-cell offset to eliminate ambiguities. Each logical layer consists of two physical layers of drift tubes that partially overlap each other (see Figure 4.9). The overlap is greater at the inner edge of the detector as a result of forming a conical surface with rectangular cells. The overlap not only provides redundancy with the average muon traversing six cells, but the resulting stereo angle of 3.5 mrad between adjacent cells permits the measurement of the polar angle of the track.

A layer of four CSX scintillation counters is installed on both the inside and outside surfaces of each 15° CMX sector. The counters on the inside and outside layers are half-cells staggered with respect to each other thereby doubling the effective granularity of the system.

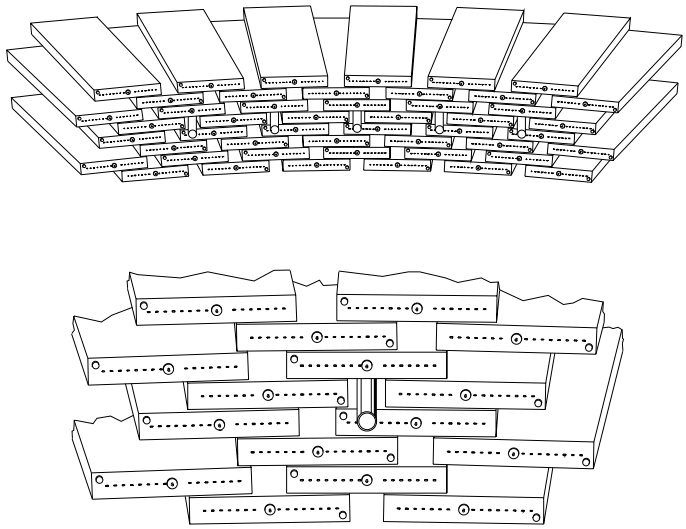

Figure 4.9: Drift tube layout in a 15° CMX module.

4.3.4 Luminosity counters (CLC)

The luminosity at a hadron collider can be determined from the rate of inelastic $p\bar{p}$ interactions. This process has a large cross section known with an uncertainty of 3% [54]. The basic formula for the integrated luminosity L is:

$$L = \int_{\Delta\ t} \mathcal{L} dt = \frac{N_{p\bar{p}}}{\sigma_{inel}} \tag{4.3}$$

where $N_{p\bar{p}}$ is the number of inelastic $p\bar{p}$ interactions in time $\Delta\ t$ and σ_{inel} is the $p\bar{p}$ inelastic cross section. $N_{p\bar{p}}$ is derived from the number of empty crossings.

The Čerenkov Luminosity Counters (CLC) [55] cover the pseudo-rapidity range $3.7 \leq |\eta| \leq 4.7$ in the forward and backward regions. Each CLC detector module consists of 48 thin, long, conical, gas filled Čerenkov counters. These counters are arranged around the beam pipe in three concentric layers, with 16 counters each, and pointing to the centre of the interaction region (see Figure 4.10). The Čerenkov counters offer several advantages to measure the luminosity. Primary particles from $p\bar{p}$ interactions travel along the cone's axis and produce a large signal, whereas secondary particles produced in the beam pipe and plug calorimeter cross the counter at different angle thus giving a small amount of light. In addition, the Čerenkov counter is not sensitive to low momentum particles since it has a momentum threshold [2]. Also the counter is not sensitive to particles coming from the beam halo interactions. These particles hit the counter from behind and therefore, emit light in the opposite direction.

[2] 2.2 GeV/c for pions in isobutane at normal pressure

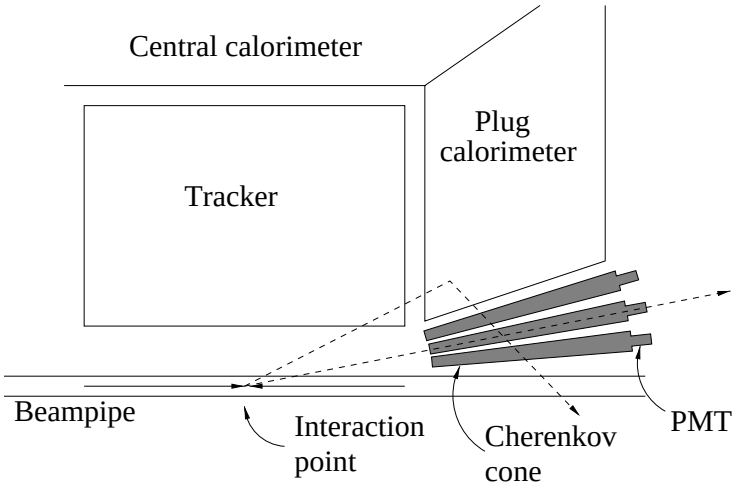

Figure 4.10: Schematic view of the luminosity monitor inside a quadrant of CDF.

Currently, it is estimated that the CLC measures the Luminosity with an accuracy of 10%, and it is aimed to improve it to less than 5% [56].

4.3.5 Triggers

The trigger in hadron collider experiments plays an important role since the collision rate is much higher than the rate at which data can be stored to tape. In Run II, the collision rate will effectively be equal to the crossing rate of 7.6 MHz while the tape writing speed is less than 50 Hz. The role of the trigger is to efficiently extract the most interesting physics events.

The CDF trigger has a three level architecture with each level providing a rate reduction sufficient to allow for processing in the next level with minimum dead time. Level-1 uses custom designed hardware to find physics objects based on a subset of the detector information and makes a decision based on the counting of these objects (e.g. 6 GeV/c CMU muon or 12 GeV/c electron). Level-2 trigger[3] uses custom hardware to do a limited event reconstruction which can be processed in programmable processors. The Level-3 trigger uses the full detector information to fully reconstruct events in a processor farm. Figure 4.11 shows the functional block diagram of the readout electronics. Additional information can be found in [50] and [57].

[3]During the period of data taking referred in this thesis, the Level-2 trigger was not used to reject events.

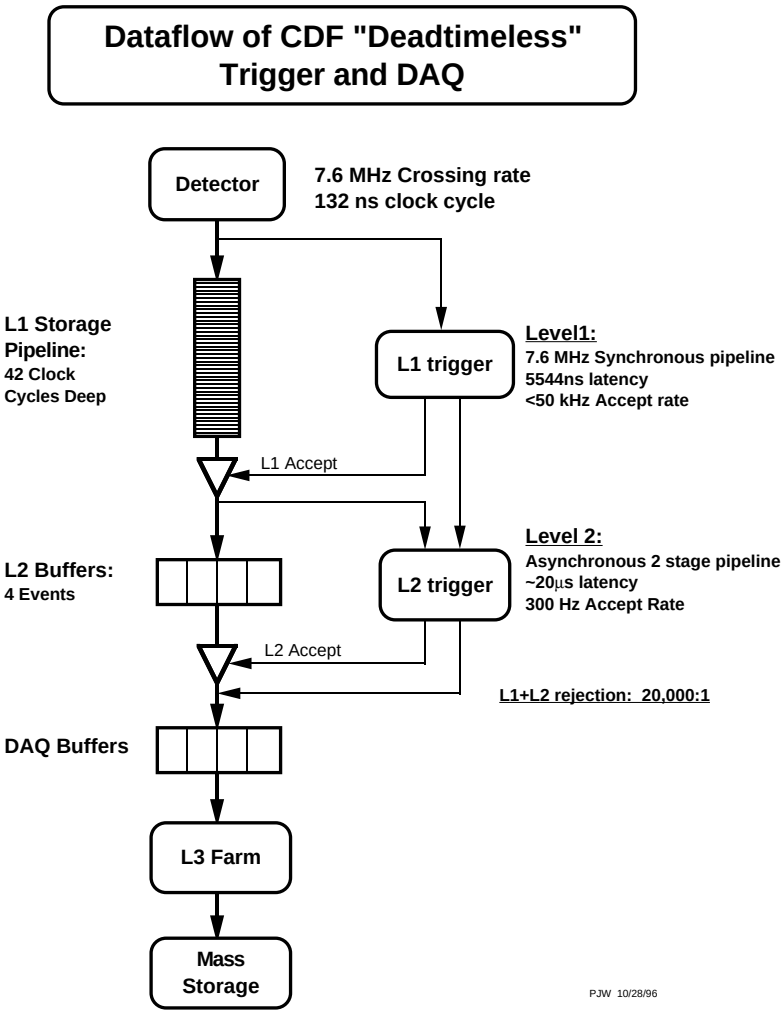

Figure 4.11: The Run II readout block diagram.

Chapter 5

Muon reconstruction, cosmic tagger and $Z^0/\gamma^* \to \mu^+\mu^-$ using RunIIa data at CDF

5.1 Introduction

The CDF experiment started taking data for Run IIa in summer 2001. The first few months of collision data allowed the commissioning of the upgraded CDF detector and the observation of the first physics events at a centre of mass energy of 2 TeV. The observation of the SM events, such as J/ψ, Z^0 and $W^\pm$ bosons, are particularly useful in demonstrating the good operation of the detector and data acquisition, and also of the reconstruction algorithms used offline. These signals are crucial for the momentum and energy scale calibrations and therefore are the first step to take with the initial data from the CDF experiment. Since the SUSY trilepton channel discussed in Section 1.4.2 relies on leptons, this chapter focuses on the muon identification via the reconstruction of $Z^0/\gamma^* \to \mu^+\mu^-$ signal using the first 3.1 pb^{-1} of data and the measurement of the Z^0 production cross section. Furthermore, since cosmic ray muons are an important background to the $Z^0/\gamma^* \to \mu^+\mu^-$ signal and also to many other physics signals, such as the SUSY trilepton channel, a cosmic ray muon tagger has been implemented.

Section 5.2 introduces the muon identification with the CDF detector. Section 5.3 describes the implementation of the first version of the CDF cosmic ray muon tagger and its performance. Section 5.4 describes the analysis performed to obtain the first $Z^0/\gamma^* \to \mu^+\mu^-$ signal of Run IIa using the cosmic tagger and the measurement of

the Z^0 production cross section at $\sqrt{s} = 2$ TeV.

5.2 Muon identification

This section gives a brief overview of the muon reconstruction as currently available and some of the quantities used for muon identification. It is worth noting that presently the CDF software is still under development and not all quantities used for muon identification are available. A Monte Carlo sample of single muons has been used, generated with a flat momentum distribution between 4 and 40 GeV/c and $|\eta| < 1.0$, using the full CDF simulation and reconstruction software[1].

5.2.1 Muon reconstruction

The muon reconstruction is based on the association of a track element (stub) in a CDF muon chamber to an extrapolated charged particle track. Muon hits are reconstructed using the drift chamber time to distance relationship in the $R\phi$ plane, and charge division in the Rz plane. Muon hits are then used to reconstruct a three dimensional muon stub using a linear fit. Finally, the tracks, extrapolated to the muon chamber, taking into account the non uniformity of the magnetic field, are matched to the muon stub. The versions of the CDF software used in this chapter allow the simulation and reconstruction of CMU, CMP, and CMX stubs; the BMU is not yet implemented.

5.2.2 Calorimeter Energy

Since the muon is a minimum ionising particle (MIP), the amount of electromagnetic energy, E_{em}, and hadronic, E_{had}, that can be deposited in the calorimeter towers are small. The mean measured energy deposits in the electromagnetic calorimeter and hadronic calorimeter for a typical muon are 0.3 GeV and 2 GeV, respectively. Figure 5.1 shows the distribution of the E_{em} and E_{had} energy deposited by a single muon with 4 GeV/c $< p_T <$ 40 GeV/c obtained using the CDF detector full simulation and reconstruction. In Run I analyses, the standard muon identification cuts required that the E_{em} and E_{had} to be less than 2 GeV and 6 GeV respectively.

[1]The release version 4.1.0 of the software was used for producing the MC samples used in this chapter

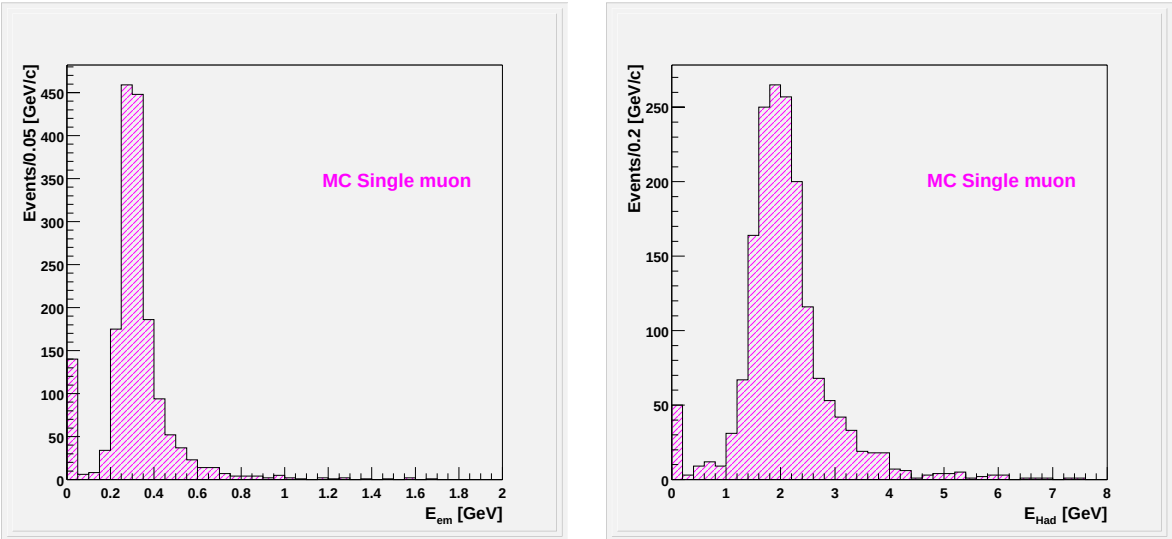

(a) (b)

Figure 5.1: Electromagnetic calorimeter (a) and hadronic calorimeter (b) energy deposit from a single muon with $4 < p_T < 40$ GeV/c.

5.2.3 Track Matching

The correct track association with a muon stub can be determined using the matching δX quantity which is the distance in $R\phi$ between the extrapolated track and the muon stub. This variable shows a p_T dependence due to multiple scattering effects (see Figure 5.2).

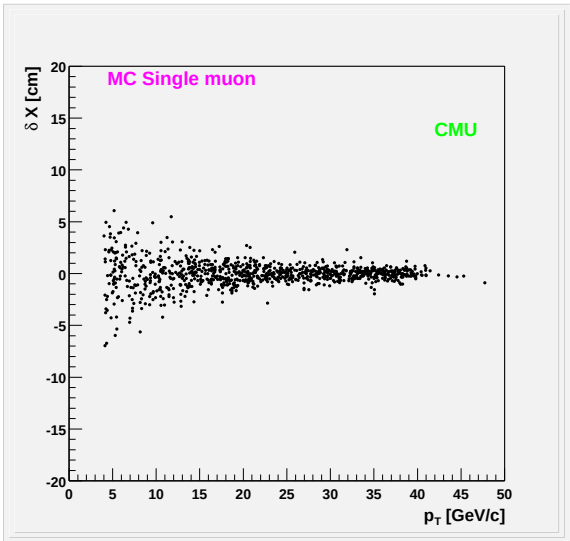

Figure 5.2: Distance, δX between the CMU stub and the extrapolated track in the $R\phi$ plane versus the muon momentum.

5.3 Cosmic ray muon tagger

Cosmic ray muons can appear to be muons created in $p\bar{p}$ collisions and therefore are a background to the single muon, dimuon and trilepton samples in CDF. In some cases both *legs* (incoming and outgoing with respect to the beam line) are reconstructed; while in others, only one *leg* is reconstructed. The *one leg* case occurs when the pattern recognition finds only the ingoing or outgoing track due to the timing of the COT hits being incompatible with the times expected from a track coming from the interaction region. This section describes the first version of the CDF cosmic ray muon tagger implemented for Run II. Currently, the tagger deals with the case where both *legs* are reconstructed.

5.3.1 Data samples and detector status

The data used for the implementation of the cosmic ray muon tagger were collected in September 2001, corresponding to an integrated luminosity of 450 nb^{-1}. Runs were selected on the basis that the COT and the CMU, CMP and calorimeters were fully operational. For all these runs, the beam position was also available from the CDF database. Events passing any Level 1 muon trigger and where Level 3 trigger reconstructs at least one muon with a $p_T > 12$ GeV/c are saved to tape. These events are then reprocessed offline with the latest version of the reconstruction code and to make the *HighPtMuon* sample, requiring at least one muon with $p_T > 12$ GeV/c and with $E_{had} < 8$ GeV. This sample is used, since it is the one containing the largest amount of cosmic ray muon data and is also used for the $Z^0 \to \mu^+\mu^-$ analysis.

During this period of data taking, certain detector components, such as the hadron TDCs and the muon scintillators, were not fully efficient or operating and therefore could not yet be used for cosmic ray muon rejection. Therefore, the cosmic ray muon selection criteria are based mainly on the topology of a cosmic ray event, i.e. two muons back to back and displaced from the interaction point.

5.3.2 Cosmic ray muon selection criteria

Cosmic ray events can trigger the detector independently of a collision occurring. These events have the property of having a small number of reconstructed tracks when they do not overlap with a minimum bias event. The track reconstruction software uses timing information to correctly create tracks from hits in the COT and

is optimised for reconstructing tracks originating from the interaction region. Since cosmic ray muons traverse the detector, their timing information are different from tracks originating from the interaction point. Occasionally, the track reconstruction software will create two tracks where only one exists. Each track may be associated to different stubs in the muon chambers thus creating two muons instead of one. In order to approximately distinguish between cosmic ray events and physics events, the plots presented below use the following colour scheme: red for less than 5 track events and blue for more than five track events.

In order to remove cosmic ray background in events with at least two muons, the muon pair with the largest acolinearity was selected. Since cosmic ray muons are independent of the interaction region, the distance from the nominal interaction point, $z0$, in the Rz plane and, $d0$, in the $R\phi$ plane can be used.

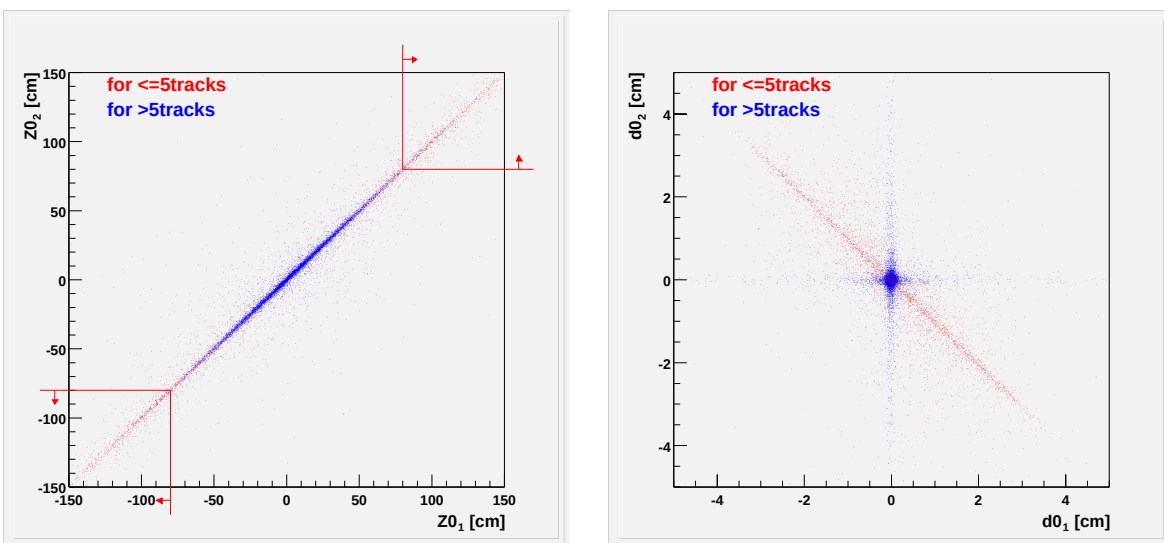

(a) (b)

Figure 5.3: Two dimensional plot of $z0$ (a) and $d0$ (b) for the selected muon pair, for less than 5 track events (red) and more than 5 track events (blue). The arrows indicate the region selected following the criteria outlined in the text.

Figure 5.3(a) shows the two dimensional plot of the $z0$ of one muon against the other one. Events where for both muons $z0$ are greater than 80 cm are not considered since they have a very low probability of coming from the interaction region.

In order to use the $d0$ of the muon track, this variable must be corrected to take into account the beam position. At production time, the beam position is stored in the CDF database. Two possible types of beam position can be accessed: the COT beam position which is calculated from COT based tracks only and the SVX beam

position which is calculated from COT tracks which have silicon hits associated to them. The SVX beam position is more precise than the COT beam position, but since the silicon detector was in a commissioning phase, the SVX beam position was not always available. Therefore, the best available was used to obtained the beam position. The $d0$ of the track is then corrected taking into account the beam position, for each run, in the $R\phi$ plane and the beam slope in the Rz plane. Figure 5.3(b) shows the two dimensional plot of the corrected $d0$ of one muon against the other one. In the case of cosmic ray muons, the $d0$ has a flat distribution and $|d0_1| \simeq |d0_2|$, whereas for physics events, $d0$ is centered at zero, with cases where one of the muon $d0$ is badly reconstructed.

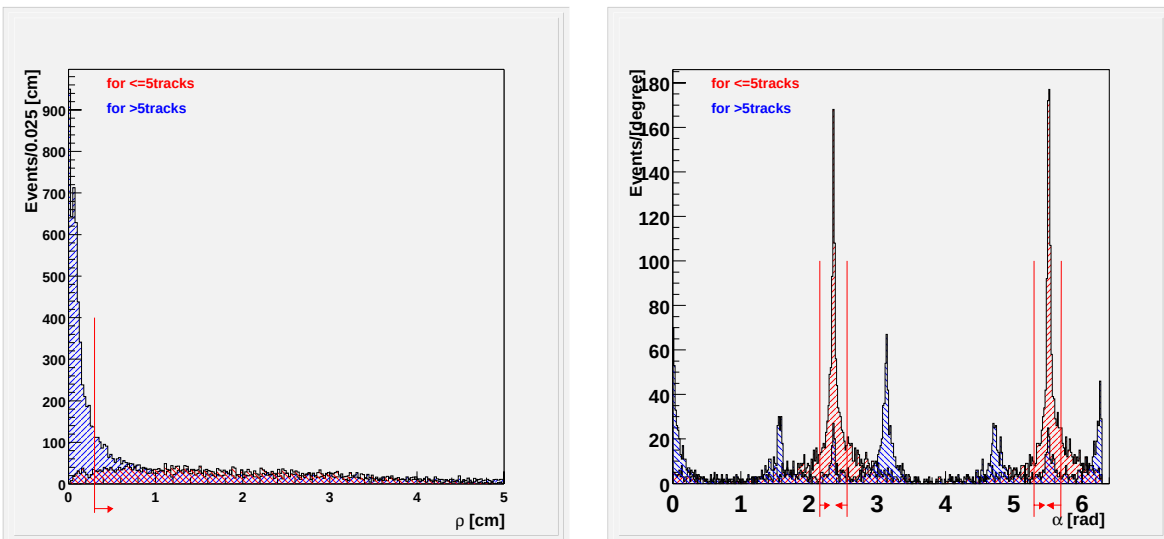

(a) (b)

Figure 5.4: Distribution of $\rho = \sqrt{d0_1^2 + d0_2^2}$ (a) and $\alpha = \tan^{-1}(d0_2/d0_1)$ when $\rho > 0.3$ cm (b) for less than 5 track events (red) and more than 5 track events (blue). The arrows indicate the region selected following the criteria outlined in the text.

In order to separate the cosmic ray muons from real physics events, this plot can be transformed to polar coordinates, where the radius is defined as $\rho = \sqrt{d0_1^2 + d0_2^2}$ and the angle between the $d0$'s is defined as $\tan\alpha = d0_2/d0_1$ (see Figure 5.4). Events where $\rho > 0.3$ cm and $|\alpha - \frac{3\pi}{4}| < 0.2$ rad or $|\alpha - \frac{7\pi}{4}| < 0.2$ rad are tagged as cosmic ray events.

Cosmic ray muons have the properties of being back to back in the $R\phi$ and Rz planes, which can be seen from the distribution of the acolinearity plotted in Figure 5.5(a). However, $Z^0/\gamma^* \to \mu^+\mu^-$ events also tend to have a large acolinearity between the two muons (see Figure 5.5(b)). In hadron collisions, the underlying event deposits

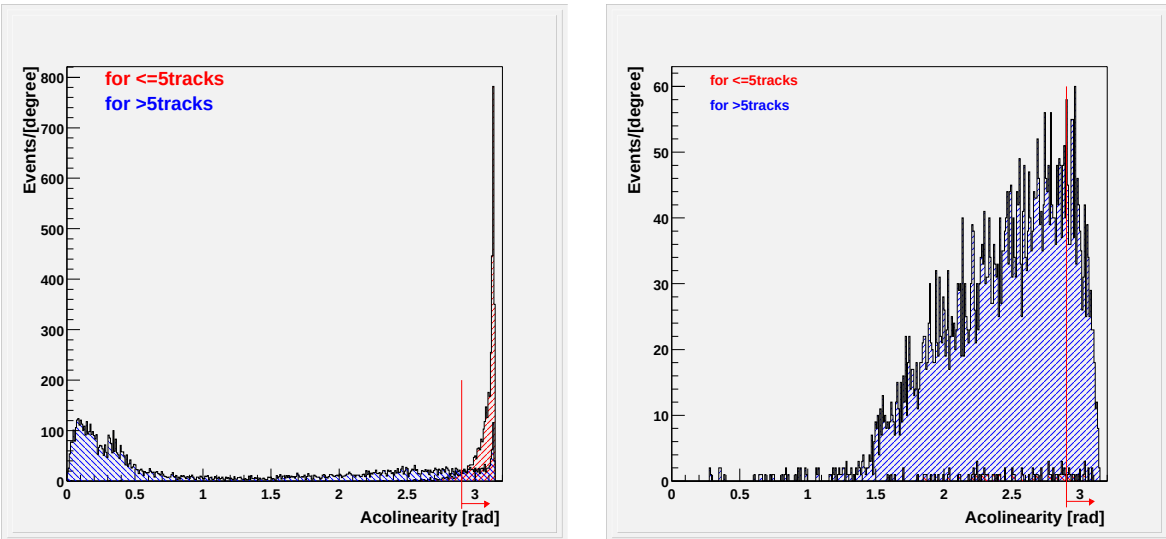

(a) (b)

Figure 5.5: Distribution of the acolinearity for the data (a) and MC Drell-Yan $Z^0/\gamma^* \rightarrow \mu^+\mu^-$ (b), for less than 5 track events (red) and more than 5 track events (blue). The arrows indicate the region selected following the criteria outlined in the text.

energy in the forward calorimeters (see Figure 5.6(b)), whereas for cosmic ray events not overlapping with minimum bias events, the energy deposited in the forward region is typically less than 10 GeV due to detector noise (see Figure 5.6(a)). Events where the acolinearity is greater than 2.9 rad and where the energy deposited in the forward calorimeters, E_{plug} is less than 10 GeV are tagged as cosmic ray events.

The selection criteria used to identify cosmic ray muons where both legs are reconstructed are summarised in Table 5.1.

Selection criteria for cosmic ray events
$1 - \lvert z0_1 \rvert > 80$ cm and $\lvert z0_2 \rvert > 80$ cm
or
$2 - \rho > 0.3$ cm and $(\lvert \alpha - 3\pi/4 \rvert < 0.2$ rad or $\lvert \alpha - 7\pi/4 \rvert < 0.2$ rad$)$
or
$3 - Acol > 2.9$ rad and $E_{plug} < 10$ GeV

Table 5.1: Criteria used to select cosmic ray events.

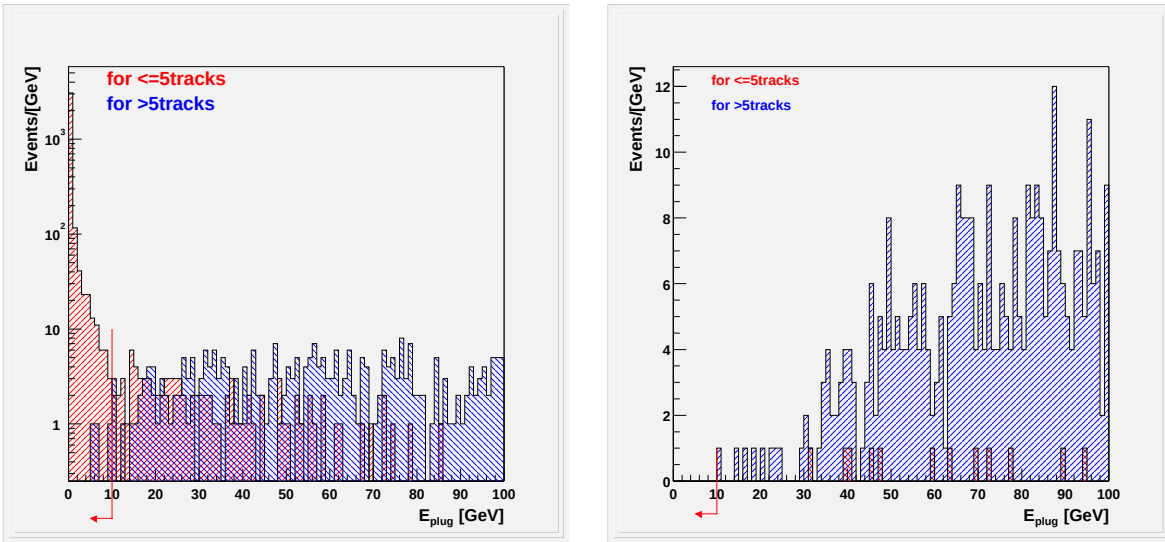

(a) (b)

Figure 5.6: Distribution of the forward energy, E_{plug}, when $Acol > 2.9$rad, for the data (a) and MC Drell-Yan $Z^0/\gamma^* \rightarrow \mu^+\mu^-$ (b), for less than 5 track events (red) and more than 5 track events (blue). The arrows indicate the region selected following the criteria outlined in the text.

5.3.3 Performance of the cosmic ray muon tagger

In order to estimate the purity of the sample obtained after rejection of cosmic ray events, the timing information of each muon from the CHA hadron TDC was used. In the case of a cosmic ray event, the difference in the CHA TDC timing information, δt_0, between the "bottom" leg and the "top" leg corresponds to about 18 ns, which is approximatively the time taken by a relativistic particle to cross from one side of the CHA to the other opposite side. In the case of a physics event, the difference in the timing information of both muons is centered toward zero since they originate from the interaction point. At the time of writing, the final CHA TDC timing optimisation were not fully implemented. Consequently, the timing resolution used for the CHA TDC was about 5.7 ns which however suffices to distinguish between muons originating from the interaction point and the cosmic ray muons.

Figure 5.7(a) shows the distribution of δt_0 for events identified as cosmic ray muons (magenta) using the criteria summarised in Table 5.1 and for the physics events (green). The central part of each distribution was fitted with a gaussian function as indicated by the two black curves in Figure 5.7(a). A double gaussian fit, using the parameters obtained from the two gaussian functions, is then used to estimate the

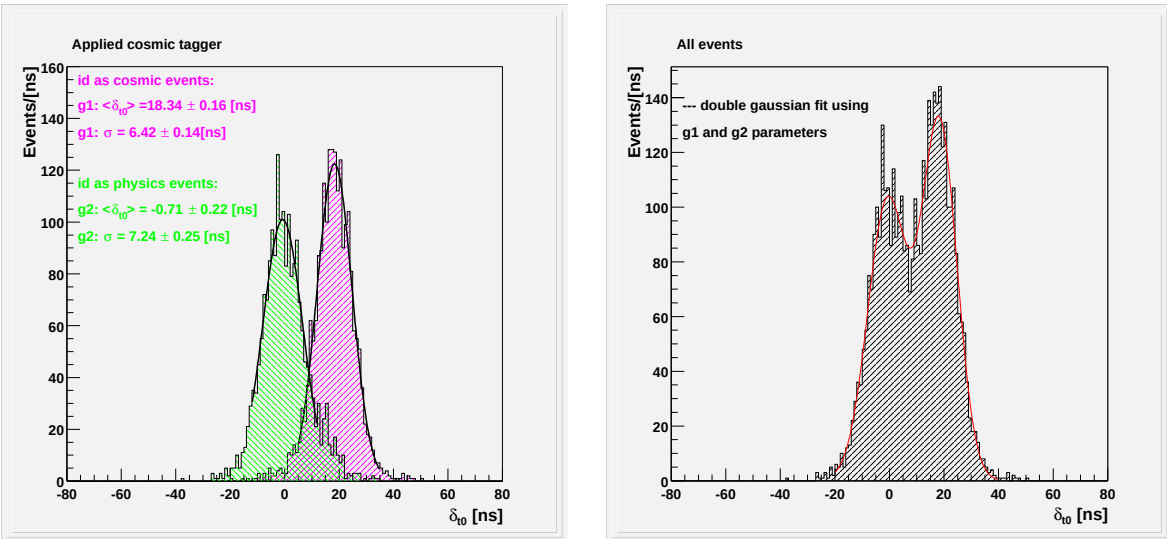

(a) (b)

Figure 5.7: Distribution of δt_0 (a) between the selected muon pair for events tagged as cosmic (pink) and the other events (green). The black curves indicate the gaussian fits obtained for each case as described in the text. Distribution of δt_0 (b) between the selected muon pair for all events. The red curve indicates the double gaussian fit obtained as described in the text.

amount of each contribution in a given sample.

Figure 5.7(b) shows the distribution of δt_0 for the whole sample. The red curve indicates the double gaussian fit obtained combining the cosmic ray and physics event parametrisations. The fraction of cosmic ray events in the sample used can be calculated from the fit and is estimated to be $53.8 \pm 0.6\%$.

Figure 5.8 shows the distribution of δt_0 for events remaining after removal of the events tagged as cosmic ray muons as defined by Table 5.1. The curve indicates the fit obtained using the double gaussian fit. The purity of this sample after cosmic ray muons removal is estimated to be $95.8 \pm 1.0\%$.

5.3.4 Future plans

The cosmic ray muon tagger has been implemented within the official CDF software code and will be used in many CDF analyses. As mentioned previously, some useful information such as the hadron TDC timing information or the muon scintillator timing were not yet fully operational at the time of the first implementation of the

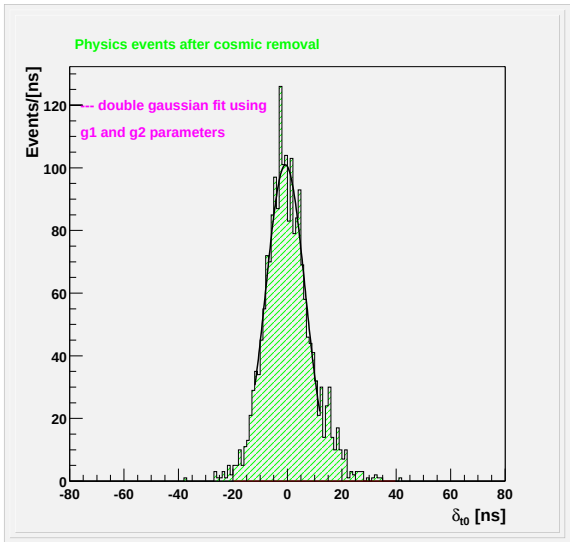

Figure 5.8: Distribution of δt_0 between the selected muon pair for the events remaining after cosmic ray rejection. The curve indicates the double gaussian fit obtained as described in the text.

cosmic ray muon tagger. It is foreseen to improve the cosmic ray muon tagger as additional tools become available as well as to implement the one *leg* case.

5.4 First $Z^0/\gamma^* \to \mu^+\mu^-$ events

The Standard Model process, the Z^0 boson decaying leptonically, is one of the first processes investigated at the start of data taking and is particularly useful to check the performance of the different sub-systems of the detector and to optimise lepton identification. It is also used to determine the momentum scale by normalising the reconstructed $Z^0 \to \mu^+\mu^-$ mass to the world average, and to measure the momentum resolution in the high p_T region. This section describes the analysis performed to isolate the first $Z^0/\gamma^* \to \mu^+\mu^-$ signal and the measurement of the Z^0 production cross section at $\sqrt{s} = 2$ TeV.

5.4.1 Data samples and detector operation

The 3.1 ± 0.31 pb^{-1} of data collected by the CDF experiment between the 8th of August and the 6th of October 2001, were used to search for $Z^0/\gamma^* \to \mu^+\mu^-$ can-

didates. The analysis was performed using the *HighPtMuon* sample processed with CDF software version 4.2.0. During this period of data taking, the CMX detector was relatively noisy, since the toroids, which provides shielding from the beam scattered particles, were not yet in their nominal position. In addition, the BMU was not yet fully operational.

A Monte Carlo sample of Drell-Yan $Z^0/\gamma^* \to \mu^+\mu^-$ was generated with PYTHIA [44] and simulated and reconstructed via the CDF software version 4.1.0. The luminosity for this MC sample was 120.8 pb^{-1}.

5.4.2 Selection criteria

The main backgrounds to the $Z^0/\gamma^* \to \mu^+\mu^-$ signal are cosmic ray muons and real or fake muons from hadronic jets. The selection criteria applied to isolate a Z^0 peak were chosen in order to take into account the detector operation and the cuts were kept loose since the detector sub-components were being commissioned. The topology of a $Z^0/\gamma^* \to \mu^+\mu^-$ event consists of two isolated oppositely charge muons with large acolinearity and with their invariant mass consistent with the mass of the Z^0.

The cosmic ray muon tagger described in Section 5.3.2 was used to reject the cosmic ray background. In order to remove badly reconstructed tracks, the number of COT axial hits is required to be greater than 25. As mentioned previously, muons from a Z^0 event are isolated, which is not the case for real or fake muons in hadronic jets. The calorimetry isolation, $E_T^{0.4}$, is determined by summing the transverse energy deposited in the calorimeter in a cone in $\eta-\phi$ space of $\Delta R = \sqrt{(\Delta\eta)^2 + (\Delta\phi)^2} = 0.4$ around the muon direction, subtracting the transverse energy of the muon deposited in the calorimeters:

$$E_T^{0.4} = \sum_{\Delta R<0.4} E_T - E_T(\mu) \tag{5.1}$$

Figure 5.9 shows the distribution of $E_T^{0.4}$ for data (a) and MC Drell-Yan (b). Both muons are required to have $E_T^{0.4}$ less than 4 GeV.

Since the BMU muon chambers were not fully operational, BMU muons are rejected. In order to reject fake CMX muons due to beam scattered particles, the number of hits in a CMX stub is required to be greater than 5 (see Figure 5.10(a)).

Figure 5.10(b) shows the distribution of the track matching variable in the CMU, δX, for the highest p_T muon in the event. This variable is required to be less than

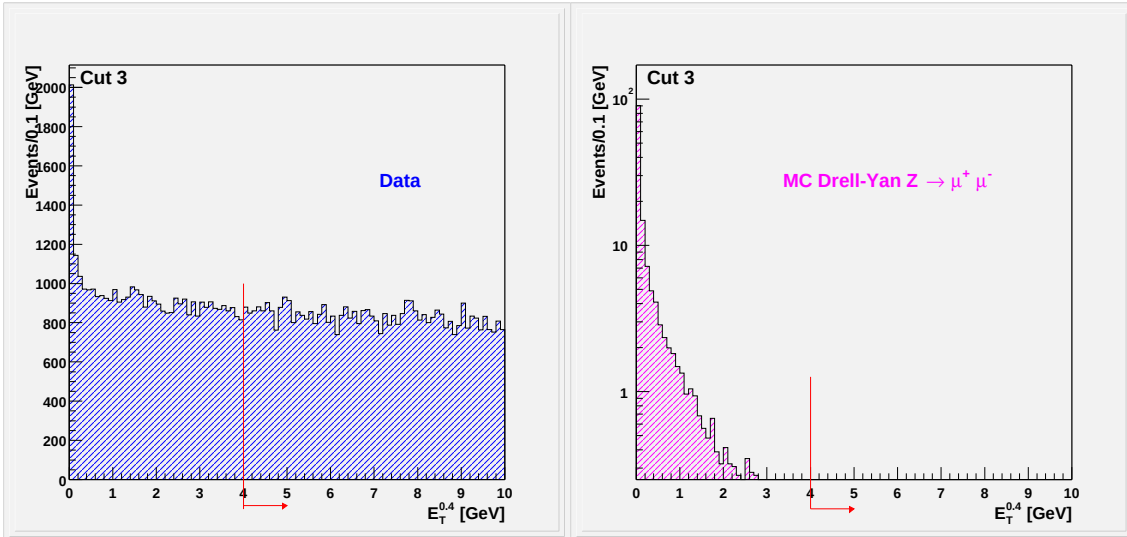

(a) (b)

Figure 5.9: Distribution of the total transverse energy in a cone of $\Delta R = 0.4$ around the muon direction, $E_T^{0,4}$ for data (a) and MC (b) before the cut is applied. The line indicates where the cut is placed and the direction of the arrow indicates the region removed.

5 cm for the highest p_T muon and less than 10 cm for the second highest p_T muon.

Figures 5.10(c) and (d) show, respectively, the distribution of E_{em} and E_{had} deposited by each muon. Those variables are required to be less than 2 GeV and 6 GeV, respectively .

For each muon candidates, Figure 5.11(a) shows the distribution of the $R\phi$ impact parameter, $d0$, corrected for the beam position and Figure 5.11(b) shows $z0$. In order to reject muons which originate from decay in flight and cosmic rays, $|d0|$ is required to be less than 0.3 cm and $|z0|$ is required to be less than 60 cm.

Finally, the muon pair is required to have opposite charge. Table 5.2 summarises the number of data events and the percentage of Drell-Yan MC after each cut for $|\eta_\mu| < 2.0$ and for $|\eta_\mu| < 0.6$ [2]. At the end of the final selection, the number of data candidates within the mass range $66 < M_{\mu^+\mu^-} < 116$ GeV/c^2 and with $|\eta_\mu| < 0.6$ is 27; the efficiency of the analysis is $81.7 \pm 0.9\%$.

In order to improve the momentum resolution, the muon tracks were refitted using the COT beam constraint. Additionally, a correction on the curvature (crv) determined by requiring the ratio of energy to momentum, E/p, for electrons to be independent of charge, was applied to take into account the misalignment between

[2] $|\eta| < 0.6$ being the η range used for the Z^0 production cross section measurement; see Section 5.4.3

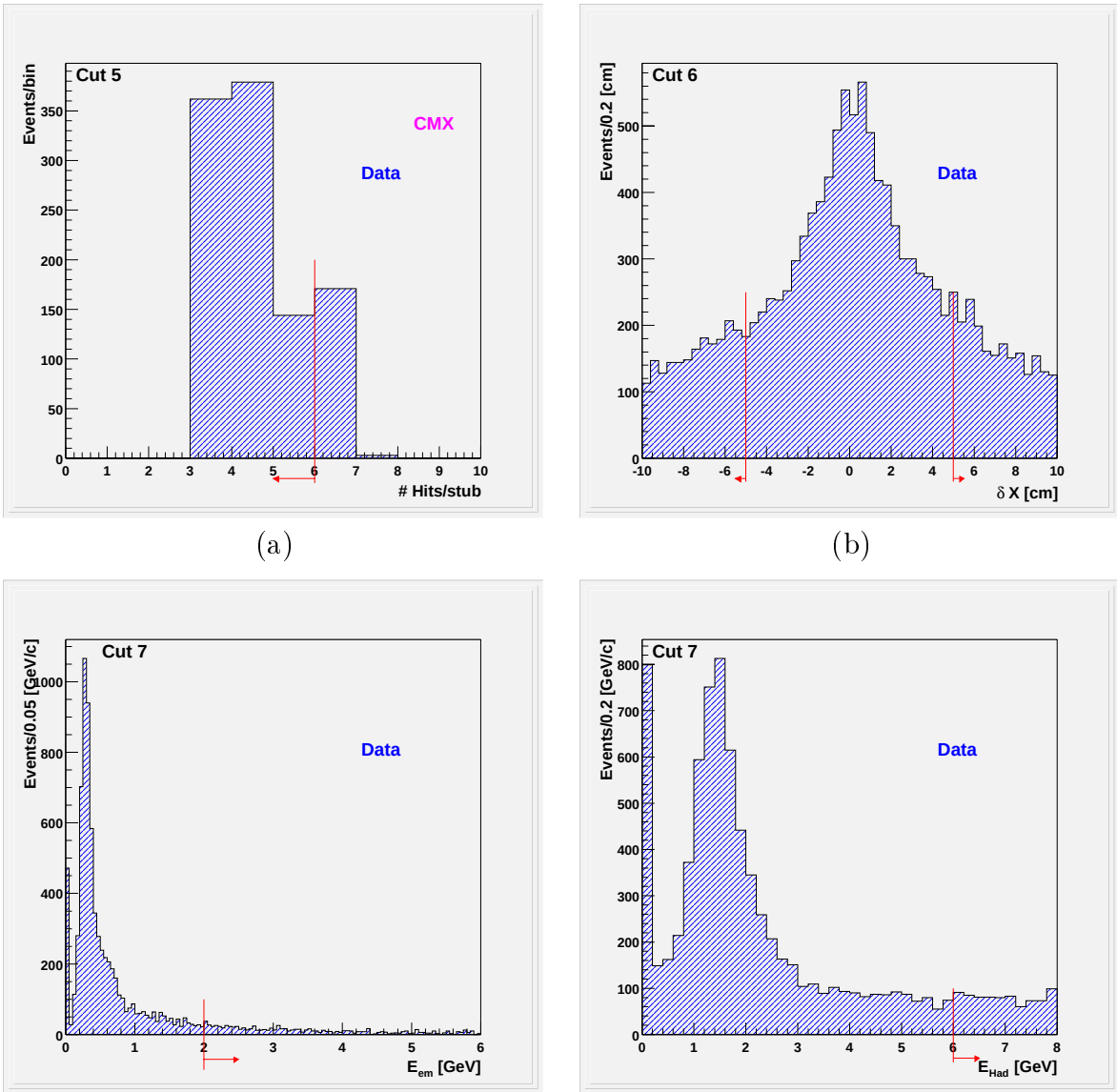

Figure 5.10: (a) Number of hits per stub for CMX muons. (b) Track matching variable, δX, for CMU muon. (c) Total electromagnetic energy deposited by the muons. (d) Total hadronic energy deposited by the muons. The variables are plotted for the data, before the cut is applied. The line indicates where the cut is placed and the direction of the arrow indicates the region removed.

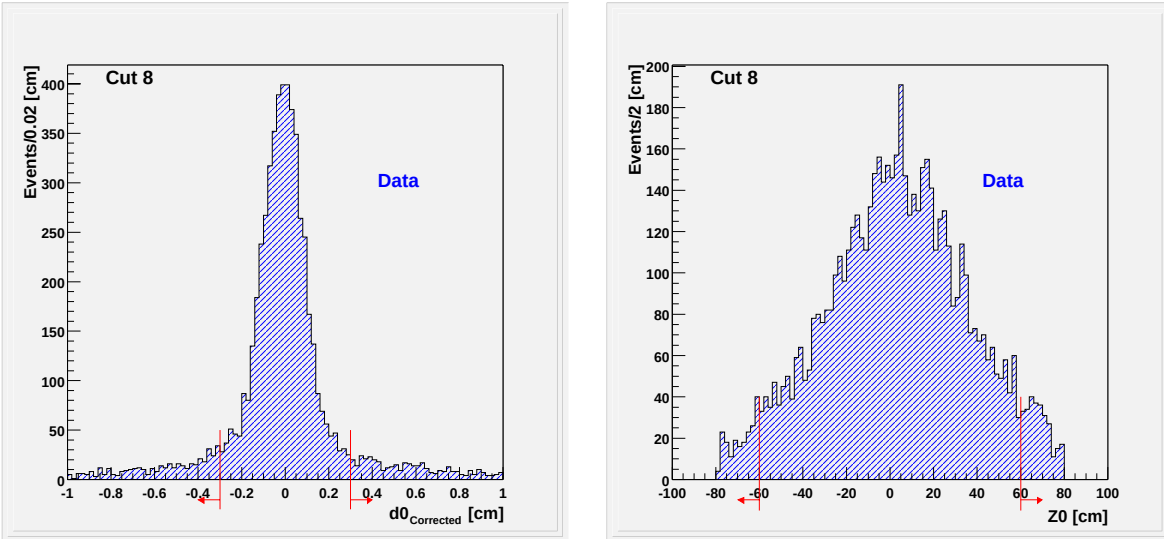

(a) (b)

Figure 5.11: (a) $d0$ distribution of the muons. (b) $z0$ distribution of the muons. The variables are plotted for the data, before the cut is applied. The line indicates where the cut is placed and the direction of the arrow indicates the region removed.

	# data events after cut		MC $Z^0/\gamma^* \to \mu^+\mu^-$ after cut (%)	
Criteria	$\|\eta\| < 0.6$	$\|\eta\| < 2.0$	$\|\eta\| < 0.6$	$\|\eta\| < 2.0$
No Cut	68690	75357	100	100
1- Cosmic ray	46930	52144	99.9	99.3
2- $nAxHits > 25$	42384	45709	99.9	99.3
3- $E_T^{0.4} < 4$ GeV	7033	8260	94.6	94.5
4- no BMU muon	7033	7726	94.6	94.5
5- CMX $nHits \geq 6$	7033	7146	94.6	77.6
6- CMU $dx_{1\ (2)} < 5\ (10)$ cm	3246	3316	94.2	77.3
7- $E_{em\ (had)} < 2(6)$ GeV	2362	2424	84.2	69.0
8- $\|d0\| < 0.3\ cm$ & $\|z0\| < 60\ cm$	1529	1577	84.2	69.0
9- opposite charge	1117	1159	83.6	68.5
All Cuts & $66 < M_{\mu^+\mu^-} < 116$ GeV/c^2	27	44	81.7	65.6

Table 5.2: Number of data events and percentage of Drell-Yan MC after each cut for $|\eta|$ <0.6 and $|\eta|$ <2.0.

the two COT end-plates [65]:

$$\frac{1}{p_T} = sign(crv) * \frac{1}{p_T} - .0007 - .00103 * sin(\phi - .8) + .00015 * tan^{-1}(\theta)$$

Figure 5.12 shows the invariant mass distribution of the muon pair candidates for $|\eta| < 1.0$, after the selection criteria 1 to 9 listed in Table 5.2, without applying the cosmic ray muon filter and after applying the filter. The $Z^0/\gamma^* \rightarrow \mu^+\mu^-$ mass peak can clearly be seen once the cosmic ray filter has been applied.

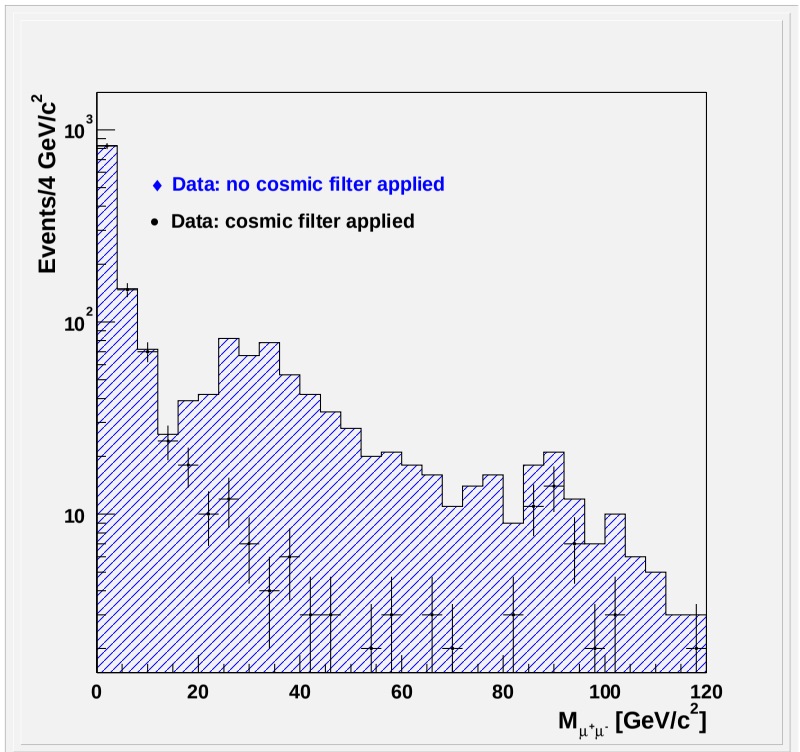

Figure 5.12: Distribution of the invariant mass of the two muons within $|\eta| < 1.0$ after selection without applying the cosmic ray filter (histogram) and with applying the cosmic ray filter (crosses).

5.4.3 Z^0 production cross section measurement

This section describes the method used to measure the Z^0 production cross section using the data candidates within the mass range of $66 < M_{\mu^+\mu^-} < 116$ GeV/c^2 and $|\eta| < 0.6$. The result obtained is compared with the Run I measurement and the theoretical prediction [66].

Since the efficiency of the CMX detector was poor for this period of data taking, only muons having CMU, CMP or CMUP stubs (*i.e.* $|\eta| < 0.6$) were considered.

Additionally, the data events remaining were scanned with the CDF event display to remove the remaining cosmic ray events. The number of observed Z^0/γ^* candidate events, N_{obs}, obtained within a mass region of $66 < M_{\mu^+\mu^-} < 116$ GeV/c^2 was 27.

Detector efficiencies and acceptance

The detector acceptance for the MC, A_Z^{MC}, to reconstruct a $\mu^+\mu^-$ pair within a mass range of $66 < M_{\mu^+\mu^-} < 116$ GeV/c^2, where both muons are reconstructed within $|\eta| < 0.6$, is defined as:

$$A_Z^{MC} = \varepsilon^{geo}\ \varepsilon_{MC}^{rec} \tag{5.2}$$

where $\varepsilon^{geo} = 7.3 \pm 0.5\%$ is the geometrical acceptance, *i.e* the fraction of $\mu^+\mu^-$ events generated by the Drell-Yan MC, where both muons are within $|\eta_\mu| < 0.6$ and have an invariant mass between 66 and 116 GeV/c^2. $\varepsilon_{MC}^{rec} = 91.7 \pm 0.6\%$ is the efficiency for reconstructing both muons in either of the CMU or CMP muon chambers. The error of 0.5% given on the geometrical acceptance is due to the theoretical uncertainty on the parton distribution functions. Thus, the MC detector acceptance is $A_Z^{MC} = 6.7 \pm 0.6\%$.

In order to verify that the reconstruction efficiency in the data, ε_{Data}^{rec}, agrees with the one obtained in the MC, the reconstruction efficiencies for the CMU and CMP detectors are estimated from the number of reconstructed muons with CMU stub only (N_μ^{CMU}), CMP stub only (N_μ^{CMP}) and CMU and CMP stubs (N_μ^{CMUP}), thus exploiting the fact that both detectors have similar $\eta - \phi$ coverage.

The estimate of the CMU efficiency, ε_{CMU} is calculated using:

$$\varepsilon_{CMU} = \frac{N_\mu^{CMUP}}{N_\mu^{CMUP} + N_\mu^{CMP}} \tag{5.3}$$

and similarly for the CMP efficiency, ε_{CMP}:

$$\varepsilon_{CMP} = \frac{N_\mu^{CMUP}}{N_\mu^{CMUP} + N_\mu^{CMU}} \tag{5.4}$$

Table 5.3 gives the reconstruction efficiencies of CMU and CMP muons in MC and data.

The CMU efficiency is in agreement within errors between the MC and the data. However, the CMP efficiency is $\sim 25\%$ lower in the data compared to the MC. This

Detector	MC	Data
CMU	$76.7 \pm 0.8\%$	$80.6 \pm 6.6\%$
CMP	$81.9 \pm 0.8\%$	$61.7 \pm 7.1\%$

Table 5.3: Reconstruction efficiencies of CMU and CMP for single muon in the MC and data.

is explained by the fact the CMP detector was not operational for the full period of commissioning. Therefore, a correction factor:

$$\varepsilon_{CMP}^{corr} = \frac{\varepsilon_{data}^{CMP}}{\varepsilon_{MC}^{CMP}} = 76.6\% \tag{5.5}$$

needs to be applied to the CMP only muons. The fraction of CMP only muons derived from MC is 19.6%. Having corrected the fraction of CMP only muons for the CMP inefficiency, the overall reconstruction efficiency for the data is $\varepsilon_{Data}^{rec} = 83.3 \pm 8.4\%$), which leads to $A_Z^{Data} = \varepsilon^{geo}\ \varepsilon_{Data}^{rec} = 6.08 \pm 0.7\%$. The error, 8.4%, given on ε_{Data}^{rec} is obtained from the difference in reconstruction efficiencies between the MC and the data.

The efficiency of the event selection, ε_Z^{Ana}, is estimated using the MC, to be $81.7 \pm 0.9\%$. It incorporates all cuts listed in Table 5.2 and the requirements that both muons were reconstructed within $|\eta_\mu| < 0.6$ and the measured invariant mass lies between 66 and 116 GeV/c^2.

Estimation of errors

The following systematic errors were considered:

- The error on the acceptance $\delta A_Z^{Data}/A_Z^{Data} = 12.3\%$:
  This number takes into account the percentage of errors due to:
  - the theoretical uncertainty on the parton distribution function ($\frac{\delta\varepsilon^{geo}}{\varepsilon^{geo}} = 7\%$)
  - the uncertainty on the data reconstruction efficiency ($\frac{\delta\varepsilon_{Data}^{rec}}{\varepsilon_{Data}^{rec}} = 10.1\%$)
- The error on the analysis efficiency $\delta\varepsilon_Z^{Ana}/\varepsilon_Z^{Ana} = 1.1\%$
- The error on the luminosity measurement $\delta L/L = 10\%$
- The error on Drell-Yan continuum correction factor ($\delta F_Z/F_Z = 0.2\%$) (see below)

The resulting total systematic error on the Z^0 production cross section is 15.9%. The statistical error is 22.3%.

Results

The measured cross section for the production of $Z^0 \to \mu^+\mu^-$ is obtained from:

$$\sigma(Z^0) \times \mathbf{BR}(Z^0 \to \mu^+\mu^-) = \frac{(N_{obs} - N_{bkg}) \cdot F_Z}{A_Z^{Data} \cdot \varepsilon_Z^{Ana} \cdot L} \tag{5.6}$$

where $\mathbf{BR}(Z^0 \to \mu^+\mu^-) = 3.367\%$ is the Z^0 branching fraction to dimuons [7] and $L = \int \mathcal{L} dt$ is the integrated luminosity. The number of background events, $N_{bkg} = 2 \pm 2$, in the mass region of 66 to 116 GeV/c^2, is estimated by comparing the data with the Drell-Yan MC outside the Z^0 peak.

The F_Z factor corrects the production cross section of Z^0/γ^* to the Z^0 cross section and for the finite mass of 66 to 116 GeV/c^2 to the entire mass range. This factor is taken to be 1.005 ± 0.002 [66].

The measured $Z^0 \to \mu^+\mu^-$ cross section is found to be:

$$\sigma(Z^0) \times \mathbf{BR}(Z^0 \to \mu^+\mu^-) = 163 \pm 36 \pm 26 \text{ pb} \tag{5.7}$$

where the first error is statistical and the second is systematic. Therefore, the Z^0 production cross section is measured to be:

$$\sigma(Z^0) = 4.84 \pm 1.08\ (stat.) \pm 0.77\ (syst.) \text{ nb} \tag{5.8}$$

which is in agreement with the Run I measurement of 6.94 ± 0.53 nb and with the QCD theoretical prediction of 6.05 ± 0.3 nb [66].

Figure 5.13 shows the invariant mass distribution of the muon pair candidates with $|\eta_\mu| < 0.6$ in the mass window 40 GeV/c^2 to 120 GeV/c^2, for the MC Drell-Yan $Z^0/\gamma^* \to \mu^+\mu^-$ and for the data. The MC sample was scaled to the data luminosity.

Figure 5.14 shows an event display of one of the $Z/\gamma^* \to \mu^+\mu^-$ candidates.

5.5 Conclusion

In preparation for the search for a supersymmetric trilepton signal, a cosmic ray muon tagger has been implemented, since cosmic ray muons are a source of natural

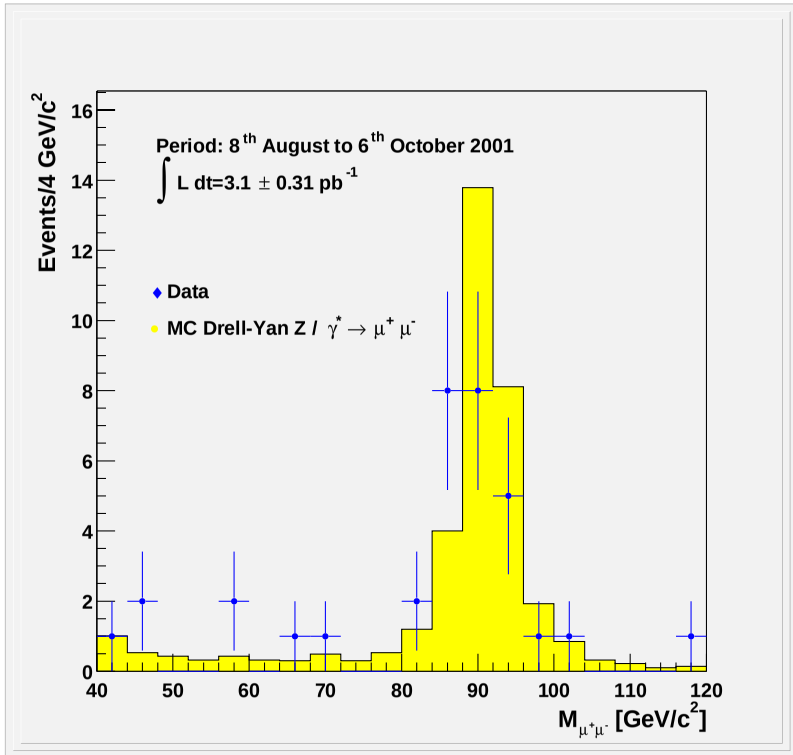

Figure 5.13: Distribution of the invariant mass of the two muons, within $|\eta| < 0.6$ after selection, for MC Drell-Yan (histogram) and data (dot). The MC has been scaled to the luminosity.

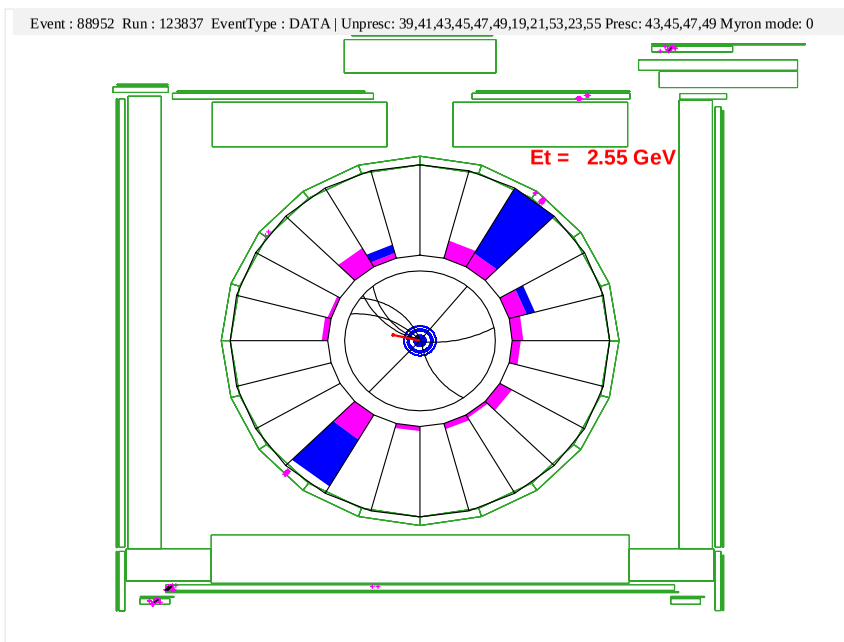

Figure 5.14: CDF event display of a $Z^0/\gamma^* \rightarrow \mu^+\mu^-$ candidate

background to many supersymmetric signals at CDF. The first version of the CDF cosmic ray muon tagger was shown to provide a physics sample with a purity of $95.8 \pm 1.0\%$. The first $Z^0/\gamma^* \rightarrow \mu^+\mu^-$ signal at Run IIa, was obtained using the CDF cosmic ray muon tagger. The Z^0 production cross section was calculated using the data candidates with invariant mass in the mass range $66 < M_{\mu^+\mu^-} < 116$ GeV/c^2 and with $|\eta_\mu| < 0.6$. This cross section was measured to be $4.84 \pm 1.08(stat.) \pm 0.77(syst.)$ nb which is in agreement with the RunI measurement of 6.94 ± 0.53 nb and with the QCD theoretical prediction of 6.05 ± 0.3 nb [66].

Chapter 6

Conclusions

The data taken in 1998 and 1999 by the DELPHI experiment at centre of mass energies between 189 GeV and 202 GeV, corresponding to an integrated luminosity of 378.2 pb^{-1}, were used to search for the supersymmetric partner of the tau lepton (stau). In this analysis, the MSSM model with conservation of R-parity is assumed. Consequently, the stau is assumed to be pair produced and to decay to a tau plus the lightest neutralino ($\tilde{\tau} \rightarrow \tilde{\chi}_1^0 \tau$). At the end of the analysis, 48 data events were selected when $43.69 \pm 3.04(stat.) \pm 0.66(syst.)$ background events are expected, where the dominant background came from W^+W^- decays. The result obtained shows no significant deviation from the Standard Model prediction.

The results were interpreted as a 95% CL confidence level exclusion region in the neutralino-stau mass plane for the conservative set of MSSM parameters of $\mu = -200$ GeV/c^2 and $\tan\beta = 1.5$. It was concluded that the mass of the stau is greater than 63 GeV/c^2 at 95% confidence level if the difference between the stau and the LSP mass is greater than 15 GeV/c^2.

The LEP experiments have ceased data taking on the 2nd November 2000 and the construction of the Large Hadron Collider (LHC) is underway. During the 2000 data taking period, the LEP2 collider ran at centre of mass energies up to 209 GeV thus probing further the SUSY parameter space. The preliminary results combining the data taken by the four LEP experiments show no evidence of supersymmetry. The LEP results found that the right-handed stau mass limit is $m_{\tilde{\tau}_R} \geq 87$ GeV/c^2, the lightest chargino mass limit is $m_{\tilde{\chi}_1^\pm} \geq 103$ GeV/c^2 and the neutralino mass limit is $m_{\tilde{\chi}_1^0} \geq 47$ GeV/c^2.

Attention is now turned toward the TEVATRON which has started taking

data in summer 2001. One of the most promising supersymmetric channels at the TEVATRON is the so-called trilepton channel. In the Minimal Supergravity model (MSUGRA), the associated production of the lightest chargino, $\tilde{\chi}_1^{\pm}$, and the second lightest neutralino, $\tilde{\chi}_2^0$, that could be produced, cascade decay to a final state with three leptons and missing transverse energy ($3l+\not{E}_T$) for some regions of the parameter space. In the case where the τ lepton decays leptonically, this channel can offer a *clean* trilepton signal with very little Standard Model background. Preliminary Monte Carlo studies have shown that for certain sets of MSUGRA parameters, the *clean* trilepton signal could be observable in Run IIa with 2fb^{-1} of data if $m_{\tilde{\chi}_1^{\pm}} \leq 177$ GeV. The observation of a signal coming from the $\tilde{\chi}_1^{\pm}\tilde{\chi}_2^0$ associated production can be enhanced if the hadronic tau decay could be efficiently tagged while keeping the Standard Model backgrounds under control. In the case where the trilepton signal is not observed, the TEVATRON can still probe a substantial region of the parameter space that was not accessible at LEP2 and could exclude the lightest chargino mass up to ~ 200 GeV/c^2.

In preparation for the search for a supersymmetric trilepton signal, a cosmic ray muon tagger has been implemented, since cosmic ray muons are a source of natural background to many supersymmetric signals at CDF. The first version of the CDF cosmic ray muon tagger was shown to provide a physics sample with a purity of $95.8 \pm 1.0\%$. The Z^0 production cross section was calculated using the data candidates with invariant mass in the mass range $66 < M_{\mu^+\mu^-} < 116$ GeV/c^2 and with $|\eta_\mu| < 0.6$. The Z^0 production cross section was measured to be $4.84 \pm 1.08(stat.) \pm 0.77(syst.)$ nb which is in agreement with the RunI measurement of 6.94 ± 0.53 nb and with the QCD theoretical prediction of 6.05 ± 0.3 nb [66].

Bibliography

[1] http://ichep2000.hep.sci.osaka-u.ac.jp/

[2] S. L. Glashow, Nucl. Phys. **B22** (1961) 579.
S. Weinberg, Phys. Lett. **B19** (1967) 1264.
V.Novikov, *Field Theory and the Standard Model*, 1998 European school of high energy physics, CERN 99-04.
C. Quigg, *The state of the Standard Model*, hep-ph/0001145.

[3] Search for the Standard Model Higgs Boson at LEP in the year 2000.
Delphi Collaboration (P. Abreu et al.). Phys. Lett. **B499** (1923-37) 2001

[4] D. Griffiths, *Introduction to Elementary Particles*, Wiley, 1987.
A. Pich, "Quantum Chromodynamics", 1994 *European School of High Energy Physics* (and references therin). (hep-ph/9505231).

R. K. Ellis, W. J. Stirling and B. R. Webber, QCD and Collider Physics, Cambridge University Press 1996.

[5] P. W. Higgs, Phys. Lett. **12** (1964) 132, Phys. Rev. Lett. **13** (1964) 508, Phys. Rev. **145** (1966) 1156.

[6] G. Hooft, M.Veltman, Nucl. Phys. **B318** (19353) (1972)

[7] Particle Data Group, The European Physical Journal **C3** (1998).

[8] A. Sirlin, "Ten Years of Precision Electroweak Physics," hep-ph/9912227.
M. Swartz, "Precision Electroweak Physics at the Z," hep-ex/9912026.

[9] Lep Electroweak Working Group, http://www.cern.ch/LEPEWWG/.

[10] Lep Susy Working Group, http://lepsusy.web.cern.ch/lepsusy/.

[11] Number of Neutrino Families from Lep 1 Measurements. M. Chemarin, Nucl.Phys.Proc.Suppl.85:67-71,2000

[12] Measurement of the Top Quark Mass. By CDF Collaboration (F. Abe et al.).Phys.Rev.Lett.80:2767-2772,1998
Direct Measurement of the Top Quark Mass at D0, B. Abbott et al. Phys.Rev.D58:052001,1998

[13] The BES collaboration, J.Z. Bai *et al.*, hep-ex/0102003;
N. Wu, Moriond QCD 2001.

[14] D. Dicus and V. Mathur, Phys. Rev. **D7** (1973) 3111.
B. Lee, C. Quigg and H. Thacker, Phys. Rev. **D16** (1977) 1519.

[15] L. Girardello and R.T. Grisaru, Nucl. Phys. **B194** (1965) (1982).

[16] P.Nath "SUSY/SUGR/String Phenemnology", hep-ph/9708221 and references therein.

[17] C. Kolda "Gauge mediated Supersymmetry Breaking Introduction, Review and Update" hep-ph/9707450 and references therein.

[18] J. Polonyi, Hungary Central Inst Res - KFKI-77-93.

[19] H.P. Nilles, Phys. REp. 110, 1, (1984).

[20] Susy and Such, S. Dawson, hep-ph/9612229.

[21] Drees, Introduction to Supersymmetry.

[22] Stephen P.Martin, P.Ramond, "Sparticle spectrum constraints", hep-ph/9306314

[23] G. L. Kane, C. Kolda, L. Roszkowski and J. D. Wells, Phys. Rev. **D49** (1994) 6173-6210.

[24] P. Smith *et al.*, Nucl. Phys. **B144** (1979) 525, Nucl. Phys. **B206** (1982) 333.
E. Norman *et al.*, Phys. Rev. Lett. **58** (1987) 1403.
T. Hemmik *et al.*, Phys. Rev. **D41** (1990) 2074.
S. Wolfram, Phys. Lett. **B82** (1979) 65.
C. Dover, T. Gaisser and G. Steigman, Phys. Rev. Lett. **42** (1979) 1117.

[25] N.Ghodbane, S.Katsanevas, P.Morawitz, E.Perez, Susygen 3, hep-ph/9909499

[26] Report of SUGRA Working Group for RunII of the Tevatron, hep-ph/0003154

[27] [Lep Injector Study Group Collaboration], "Lep Design Report. Vol. 1 and 2 " CERN-LEP/84-01, CERN-LEP/TH/83-29.

[28] S. Myers, "The LEP collider, from design to approval and commissioning, Nov 26, 1990," CERN-91-08

[29] P. Aarnio *et al.* [DELPHI Collaboration], "The DELPHI detector at LEP," Nucl. Instrum. Meth. A **303** (1991) 233.

[30] The DELPHI Collaboration, "Proposal for the upgrade of DELPHI in the forward region", DELPHI 92-142 (1992).
V. Chaubaud *et al.*,"The DELPHI silicon strip microvertex detector with double sided readout", CERN-PPE/95-96(1995).
S.J Alvsvaag *et al.*, "The DELPHI smal angle calorimeter", *DELPHI* 94-157 CAL 120 (1994).

[31] P. Abreu *et al.* [DELPHI Collaboration], "Performance of the DELPHI detector," Nucl. Instrum. Meth. A **378** (1996) 57.

[32] P. Chochula *et al.*, The DELPHI Silicon Tracker at LEP2. CERN-PPE/97-155 (1997).
The DELPHI Silicon Tracker group, Nucl. Instr. and Meth. **A412** (1998) 304-328.

[33] Ph.Charpentier *et al.*, The DELPHI Data Acquisition System, in *Proc. Int. Conf. on Computing in High Energy Physics*, ed. Y. Watase and F. Abe, page 643, Tokyo, Universal Academy Press (1991).

[34] V. Bocci *et al.*, Nucl. Instrum. Meth. A **362** (1995) 361.
J.A. Vallis *et al.* Architecture and performance of the DELPHI trigger system, 1992, IEEE 1992 Nuclear Science Symposium, DELPHI 92-162 DAS 135.
V. Canale and G. Valenti, The trigger configuration of the LEP 200, DELPHI note, 1996, DELPHI 96-104 DAS 179.

[35] J.M. Benlloch *et al.* Nucl. Instrum. Meth. A **292** (1990) 319.

[36] The DELPHI Collaboration, DELPHI Data Analysis Program **DELANA** Usser's Guide. DELPHI 89-44 PROG 137 (1989).

[37] G. Altarelli, T. Sjöstrand, F. Zwirner, "Physics at LEP2", CERN 96-01, 1996.

[38] F. A. Berends, P.H. Daverveldt and R. Kleiss, Comp. Phys. Comm. **40** (1986) 285-307

[39] F. A. Berends, P.H. Daverveldt and R. Kleiss,Comp. Phys. Comm. **40** (1986) 271-284.

[40] S. Jadach, W.Plazeck and B.F.L Ward, Phys. Lett. **B390** (1997) 298.

[41] DELPHI Collaboration, P. Abreu et al., Nucl. Instr. and Meth. **A378** (1996) 57

[42] F.Q. Berends, R.Pittau and R. Kleiss, Comp. Phys. Comm. **85** (1995) 437

[43] S. Jadach,B.F.L Ward and Z. Was, Comp. Phys. Comm. **79** (1994) 503-522

[44] T. Sjöstrand, Comp. Phys. Comm. **82** (1994) 74
T. Sjöstrand "High energy physics event generation with Pythia 5.7 and JETSET 7.4" CERN-TH/7111-93 (1993, rev. 1994).

[45] S. Nova, A. Olshevski and T. Todorov, "A Monte Carlo event generator for two photon physics", DELPHI note 90-35 PROG 152

[46] S. Katsanevas and S. Melachroinos, Physics at LEP 2, CERN yellow report, 1996, Vol2, 328

[47] "Workshop on Confidence Limits", CERN, Geneva, Switzerland, 17 - 18 Jan 2000 James, F; Lyons, L; Perrin, Y [eds] CERN.

[48] Private communication, B. King.

[49] Luminosity Upgrade Group, http://www-bd.fnal.gov/lug/runII_handbook/RunII_index.html

[50] The CDF Collaboration, http://www-cdf.fnal.gov/internal/upgrades/upgrades.html
The CDF Collaboration, http://www-cdf.fnal.gov/internal/upgrades/btb/

[51] T. K. Nelson, "The CDF Layer 00 detector", CDF-note/5780.

[52] B. Ashmanskas et al. "Open-cell Chamber to replace the CTC", CDF-note/3648.

[53] F.Abe et al., The CDF Collaboration, Phys. Rev. **D50** (1994) 2966

[54] F.Abe et al., The CDF Collaboration, Phys. Rev. **D50** (1994) 5550

[55] J.Elias et al. Čerenkov counter for Luminosity measurements, CDF-note/5003, CDF-note/4831.

[56] Private communication, J. Konigsberg.

[57] CDF Run II TRigger Table and Datasets Plan, CDF-note/4728.

[58] G.Ascoli et al. Nucl. Instr. and Meth. **A268** (1988) 33
G.Ascoli et al. Nucl. Instr. and Meth. **A268** (1988) 41

[59] M.Nojiri and Y.Yamada, hep-ph/9902201.

[60] S.Ambrgosanio et al. " Report of the Beyond the MSSM subgroup for the Tevatron Run II SUSY/Higgs Workshop" section VI, hep-ph/0006162.

[61] Stephen Tether, "The fake lepton rate for the Run Ib SUSY Trilpeton analysis", CDF-note/3566 (1996).

[62] Y.Kato, T.Kamon, B.Tannenbaum, J.Wolinski, S.Lammel, J.Hauser, "Search for the $\tilde{\chi}_1^{\pm}\tilde{\chi}_2^0$ produciton using trilepton events in the $p\bar{p}$ Collisions at $\sqrt{s}$ = 1.8TeV", CDF-note/3333 (1995).

[63] V.Barger, C.Kao, "Trilepton signature of Minimal suprgravity at the upgraded TEVATRON, hep-ph/9811489.

[64] J. Lykken, K.T. Matchev, "Tau jet signal supersymmetry at the TEVATRON", hep-ph/9910033.

[65] Private communication, L.Nodulman.

[66] F.Abe et al., The CDF Collaboration, "Measurement of Z and Drell-Yan production cross sections using dimuons in p anti-p Collisions at $\sqrt{s}$ = 1.8 TeV", Phys. Rev. **D59** (1999) 052002

Acknowledgments.

I would like to express my gratitude to Professors Paul Booth and Erwin Gabathuler for allowing me to carry out my Ph.D. at the University of Liverpool. Additional thanks need to be addressed to Prof. Booth for his advice, great support and encouragement.

I am thankful to Dr. Ronan McNulty for his supervision and endless advice, most particularly during the stau analysis. Special thanks to Dr. Barry King for his help in the preparation of the stau results for the Osaka conference, advice on the mass exclusion plots and also for proof reading this thesis. A big thank you to Dr. Beate Heinemann for her most valuable advice to my frenetic confusions, for being so joyful and putting up with me in this tiny office at FermiLab. Many thanks to Dr. Tara Shears, Dr. Phil Allport for their useful suggestions. This work would not have been possible without the availability of all of them to discuss many details of these analyses.

Sincere thanks to the Cdf muon team, especially Dr Michael Schmitt and Dr. Ken Bloom, for their advice and great support during the implementation of the cosmic ray muon tagger. Many thanks to Prof. Young-Kee Kim, Dr. Avi Yagil, Dr. Simona Rolli, Dr. Liz Sexton-Kennedy for their advice and help in so many occasions.

Special thanks to Dr. Tony Morton who has provided priceless computational help and support at Liverpool. I also would like to thanks the whole Cdf Task Force computer team, for all their help in fixing my computers.

Many thanks to the whole team of people, too numerous to list here, that "live" in the Cdf control room, and that have help me in so many occasions during my Ace shifts, to debug the DAQ, and also to my co-Ace, Dr. Victoria Martin.

Financial support from the University of Liverpool and the Particle Physics and Astronomy Research Council is acknowledged.